Star Formation in Extragalactic HII Regions.
Determination of Parameters of the Initial Mass Function

F. Kh. Sakhibov[1] and M. A. Smirnov[2]

[1]*Institute of Astrophysics, Academy of Sciences of Tajikistan, ul. Bukhoro 22, Dushanbe, 734670 Tajikistan*
[2]*Institute of Astronomy, Russian Academy of Sciences, Pyatnitskaya ul. 48, Moscow, 109017 Russia*
Received January 27, 1999

Abstract—A method for using the colors of star-forming complexes to derive the slope and upper mass limit of the initial mass function (IMF) and the age of the complex is proposed in the framework of synthetic evolutionary models of star-cluster populations. The star-formation parameters of 105 complexes in 20 spiral and irregular galaxies are determined. The IMF slopes in different star-forming complexes differ appreciably, and their dependence on the luminosities and masses of the complexes is derived. The duration of the star-formation period increases with the luminosity of the complex, and complexes with longer star-formation periods are richer in metals. The slope of the integrated IMF in a Galaxy depends on the mass spectrum of its complexes, and the upper mass limit of the IMF is lower in early-type spirals. © 2001 MAIK "Nauka/Interperiodica".

1. INTRODUCTION

One of the main characteristics of stellar systems, in particular of young star clusters, is the mass spectrum of the stellar population. The mass spectrum, or mass function, of a stellar population reflects both the initial conditions for star formation in the cluster and its history. To distinguish the initial conditions for star formation from evolutionary effects, we must know the initial mass function (IMF) of the cluster stars. One aim of this paper is to derive the IMF and ages of young star-forming complexes (SFCs) from the observed spectral energy distributions in integrated spectra. We will also analyze the variations of star-formation parameters as a function of the individual characteristics of SFCs and the morphological type and luminosity class of the parent Galaxy.

Earlier [1], we proposed a program to investigate SFCs in external galaxies based on analysis of their integrated colors, and a technique for translating these colors into the parameters of the IMF. This required the construction of a grid of theoretical models to calibrate photometric diagrams in terms of the IMF parameters. A method for calibrating two-color photometric diagrams in terms of IMF parameters and the ages of stellar groups was developed by Piskunov and Myakutin [2]. Here, we discuss a technique for comparing the observed colors of SFCs to theoretical colors in order to infer the parameters of the IMF and the cluster age; in other words, a technique for translating an SFC's color indices into information about the star formation in it.

The objects of study are young SFCs in spiral and irregular galaxies, visible as bright clumps and also known as giant extragalactic HII regions. Young SFCs in spiral galaxies are concentrated in the spiral arms rather than in the interarm space, and appear as the brightest objects

in irregular galaxies. We wish to study star formation in the individual SFCs in these galaxies: the IMF slope (α), IMF upper mass limit (M_{max}), and age t of the SFC.

In many studies, star formation in spiral and irregular galaxies has been investigated using computed synthetic spectra and the observed integrated colors of individual SFCs/giant HII regions [2–10]. There are two approaches to such studies: (1) the synthetic spectra are computed based on stellar evolutionary tracks and model atmospheres—so-called evolutionary synthesis [4, 6, 11, 12]; or (2) libraries of stellar and star-cluster spectra are used—so-called population synthesis [13]. Both methods are useful when comparing observations with the predictions of theories of stellar evolution, stellar atmospheres, and star formation. The difficulty with these approaches is that they involve too many free parameters, making the results fairly uncertain. Drawing on observational characteristics at multiple wavelengths from UV to radio and comparing these with the predictions of evolutionary population-synthesis models enabled Mas-Hesse and Kunth [6] to derive with considerable certainty information about the IMF slope, age, and star-formation regime in 17 starburst regions in irregular and blue compact galaxies. They found that the IMF slopes of SFCs range from -1 to -3, and discovered both young bursts of star formation (4 Myr) and older objects (10–15 Myr) with continuous star formation.

In this paper, we propose our own technique for comparing the observed integrated colors of SFCs with theoretical colors in the framework of an evolutionary model for a star-cluster population, considering star-formation parameters varying over a wide range. The comparison of observed spectral energy distributions with theoretical spectra is an effective tool for analyz-

ing the structure of stellar populations in SFCs. Our technique can be characterized as the conversion of integrated SFC colors into parameters describing the star formation. Once we have determined the star-formation parameters in individual SFCs, we can analyze the variations of these parameters among SFCs in other galaxies.

We now list the main arguments in favor of using individual SFCs to study star formation:

(1) SFCs/HII regions have uniform chemical compositions (metal abundance z), which can be derived from observations;

(2) SFCs are sufficiently compact and young for their IMFs to be uniform in space and time;

(3) SFCs/giant HII regions are nebulae whose ionized volume is determined by radiation from the cluster stars;

(4) Extinction can be taken into account more accurately in SFCs than in an entire Galaxy;

(5) A simple star-formation history for a young SFC can be described either by a time-independent IMF and constant star-formation rate $r(t)$, or by a starburst, when all stars are assumed to have been born simultaneously t years ago;

(6) Young SFCs/giant HII regions are common in galaxies of various types and luminosities, and are convenient tools for analyzing variations of the IMFs in galaxies with different physical conditions;

(7) Extensive observational data have been accumulated for these objects, including the integrated colors for 836 extragalactic SFCs in 49 spiral and irregular galaxies [14].

2. MODEL FOR THE STELLAR POPULATION IN A SFC

Star formation can be described by the function $b(m, t)$, which specifies the number of stars N forming in a mass interval dm during a time interval dt:

$$b(m, t) = \frac{d^2N}{dm\,dt}.$$

Assuming a simple star-formation history in an individual young SFC, which we expect to consist of a single generation of stars, the star-formation function $b(m, t)$ can be written as the product of a function $f(m)$ describing the mass distribution of the stars born (i.e., the IMF) and a function $r(t)$ describing the star-formation intensity as a function of time t (i.e., star-formation rate):

$$b(m, t) = f(m)r(t).$$

Adopting a power-law IMF $f(m) \propto m^\alpha$ and $\alpha = -2.35$, we obtain the well-known Salpeter initial mass function [15].

We used the evolutionary model for the stellar population of an SFC developed by Piskunov and Myakutin [2] and Myakutin [16]. We now briefly list the main

characteristics of this model. Most importantly, we assume that the star-formation function can be separated into two parts: the IMF $f(m)$ and the star-formation rate $r(t)$. The IMF has a power-law form, $f(m) \propto m^\alpha$ with slope α, and the masses of stars born lie in the interval $m \in (M_{min}, M_{max})$, where M_{min} and M_{max} are lower and upper mass limits for the IMF. We consider two possibilities for the star-formation function:

(1) Simultaneous star formation, when we assume that all the stars in the SFC were born simultaneously t years ago at time $t_0 = 0$, $-r(t) = \delta(t_0)$;

(2) Continuous star-formation, when we assume that star formation in the SFC began t years ago and has continued until the present time, $-r(t) = $ const.

To compute the fluxes emitted by the stars of an SFC, Piskunov and Myakutin [2] constructed theoretical Hertzsprung–Russell diagrams for SFCs of specified ages and IMFs based on evolutionary tracks and model atmospheres. Their evolutionary tracks included the effects of

(1) both early and late evolutionary stages;

(2) both low-mass and massive star models;

(3) differences in chemical composition (within the range of abundances for Population I);

(4) specific physical effects, such as mass loss during stellar evolution.

Since there were no published grids of evolutionary tracks that satisfied these conditions, a homogeneous grid was constructed based on a compilation of results from various studies [17]. Piskunov and Myakutin [2] used Schmidt-Kaler's [17] calibrations to convert bolometric stellar luminosities into U, B, V, and R fluxes. Lyman continuum fluxes were computed using the calibration of Avedisova [18], based on non-LTE model atmospheres.

The theoretical stellar composition of an SFC was represented using four-dimensional tables of the integrated colors U–B, B–V, V–R, and the Lyman continuum index LCI as functions of various star-formation parameters, namely, slope α and upper mass limit M_{max} of the IMF, age t of the SFC, and its metal abundance Z:

$$
\begin{aligned}
V\text{–}B &= f_1(\alpha, M_{max}, t, Z), \\
B\text{–}V &= f_2(\alpha, M_{max}, t, Z), \\
V\text{–}R &= f_3(\alpha, M_{max}, t, Z), \\
LCI &= f_4(\alpha, M_{max}, t, Z),
\end{aligned}
\tag{1}
$$

where $LCI = 2 - \log(I_{H_\alpha + NII}/I_B)$ is the Lyman continuum index (the intensity of the $I_{H_\alpha + NII}$ line emission in erg s^{-1} cm^{-2}) and the B-band flux I_B is in erg s^{-1} cm^{-2} Å^{-1}. In the case of ionization-bounded nebulae, the ionizing flux of the Lyman continuum can be computed from the observed H$_\alpha$ emission intensity.

3. METHOD FOR QUANTITATIVE COMPARISON OF OBSERVATIONS WITH MODELS. TRANSLATION OF INTEGRATED COLORS INTO PARAMETERS OF STAR FORMATION

The observed spectral energy distribution of an SFC—the integrated colors $U–B$, $B–V$, $V–R$, and LCI—contain information about star formation in the complex and its parameters (slope α and upper mass limit M_{max} of the IMF and age t of the SFC). Evolutionary models relating these parameters to the integrated colors of SFCs were represented in tabular form with step 0.1 in α in the interval $(-0.35, -4.35)$, step $30 M_{\odot}$ in M_{max} in the interval $(30, 120) M_{\odot}$, and step 0.2 in $\log t$ in the interval $(5.7, 8.1)$. Figure 1 shows a two-dimensional cross section (in the α–$\log t$ plane) for a theoretical model with fixed M_{max} and metallicity Z. Each point $(\alpha(i)$, $t(j)$ for fixed $M_{max}(k))$ in the α–$\log t$ plane corresponds to a set of tabulated colors $(U–B)_{tab}^{i,j,k}$, $(B–V)_{tab}^{i,j,k}$, $(V–R)_{tab}^{i,j,k}$, $\mathrm{LCI}_{tab}^{i,j,k}$. The procedure for finding the IMF parameters (α, M_{max}) and age of the SFC (t) corresponding to the observed colors $(U–B)_{obs}$, $(B–V)_{obs}$, $(V–R)_{obs}$, LCI_{obs} in the framework of a given evolutionary model (with simultaneous or continuous star formation) can be divided into the following three stages.

We first compute (O–C)—the differences between the observed and predicted colors for each entry of the table for a given model with metal abundance Z for the SFC:

$$(\mathrm{O\text{–}C})_1^{i,j,k} = (U–B)_{obs} - (U–B)_{tab}^{i,j,k},$$

$$(\mathrm{O\text{–}C})_2^{i,j,k} = (B–V)_{obs} - (B–V)_{tab}^{i,j,k},$$

$$(\mathrm{O\text{–}C})_3^{i,j,k} = (V–R)_{obs} - (V–R)_{tab}^{i,j,k}, \quad (2)$$

$$(\mathrm{O\text{–}C})_4^{i,j,k} = \mathrm{LCI}_{obs} - \mathrm{LCI}_{tab}^{i,j,k}.$$

Indices $i, j,$ and k indicate the entry corresponding to the $\alpha(i)$, $\log t(j)$, and $M_{max}(k)$ for the table of theoretical (model) colors. We then compute for each entry (i, j, k) of the theoretical table the functional

$$F_{i,j,k} = \sqrt{\sum_{l=1}^{4} [(\mathrm{O\text{–}C})_1^{i,j,k}]^2}. \quad (3)$$

In the second stage, we construct the following linear approximation to the theoretical model:

$$\alpha - a_2 M_{max} - a_3 t$$
$$= a_1 + a_4(U–B) + a_5(B–V) + a_6(V–R) + a_7 \mathrm{LCI} + \varepsilon, \quad (4)$$

where coefficients $a_1, a_2, \ldots, a_7$ are derived via least-squares fitting and error ε is a random quantity that arises due to the nonlinear nature of the model. The
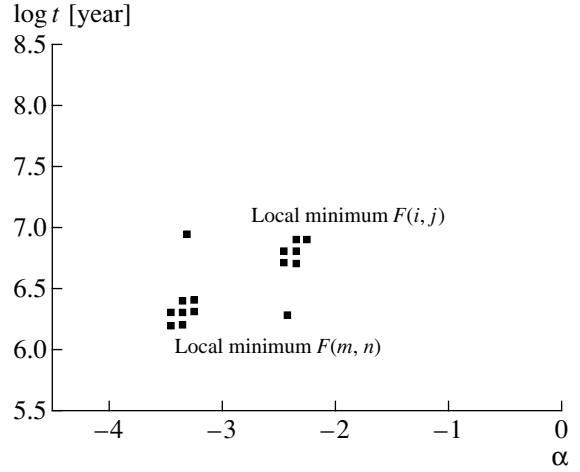
Fig. 1. Two-dimensional section (in the "slope–age" plane) of the theoretical model for fixed metallicity Z and IMF upper mass limit M_{max}.

resulting correlation coefficient $(r = 0.90)$ indicates that this linear fit is quite satisfactory.

Finally, in the third stage, we wish to convert the integrated colors of the stellar population into the IMF parameters and SFC age. We take the appropriate solution to be the table entry that simultaneously satisfies the following three conditions.

Condition 1. The absolute values of all O–C are less than the measurement errors of the corresponding colors:

$$\left|(\mathrm{O\text{–}C})_1^{i,j,k}\right| \le \sigma_{U–B}, \quad \left|(\mathrm{O\text{–}C})_2^{i,j,k}\right| \le \sigma_{B–V},$$

$$\left|(\mathrm{O\text{–}C})_3^{i,j,k}\right| \le \sigma_{V–R}, \quad \left|(\mathrm{O\text{–}C})_4^{i,j,k}\right| \le \sigma_{\mathrm{LCI}}.$$

Condition 2. The functional $F_{i,j,k}$ has the deepest local minimum. Here, we consider the local minimum to be the table entry where the value of $F_{i,j,k}$ is less than in the eight neighboring cells:

$$F_{i,j,k} < F_{i-1,j-1,k}, \quad F_{i,j,k} < F_{i,j-1,k}, \quad F_{i,j,k} < F_{i+1,j-1,k},$$

$$F_{i,j,k} < F_{i-1,j,k}, \quad F_{i,j,k} < F_{i+1,j,k},$$

$$F_{i,j,k} < F_{i-1,j+1,k}, \quad F_{i,j,k} < F_{i,j+1,k}, \quad F_{i,j,k} < F_{i+1,j+1,k}.$$

Condition 3. The difference between the right-hand and left-hand sides of Eq. (4) is less than dispersion σ of the random quantity ε:

$$|\alpha - a_2 M_{max} - a_3 t|$$
$$- |a_1 + a_4(U–B) + a_5(B–V) + a_6(V–R) + a_7 \mathrm{LCI}| < \sigma.$$

If it is possible to find for the observed colors $(U–B)_{obs}$, $(B–V)_{obs}$, $(V–R)_{obs}$, LCI_{obs} an entry (i, j, k) in the theoretical table that simultaneously satisfies these three conditions, the star-formation parameters $\alpha(i)$, $M_{max}(k)$, and $t(j)$ corresponding to this entry are adopted as the parameters for the SFC in question. When two or more

Table 1. Estimated errors in α, $M_{\max}$, and $\log t$ for various input parameters

Parameter errors	$U{-}B$, $B{-}V$, $V{-}R$, LCI	$U{-}B$, $B{-}V$, LCI	$U{-}B$, $V{-}R$, LCI	$B{-}V$, $V{-}R$, LCI	$U{-}B$, $B{-}V$, $V{-}R$
$\sigma_{M_{\max}}$, $M_\odot$	39	32	31	33	31
σ_α	0.46	0.43	0.55	0.53	0.58
$\sigma_{\log t}$	0.23	0.35	0.23	0.26	0.36

table entries satisfy conditions 1 and 3 and the functional $F_{i,j,k} \approx F_{l,m,n}$ also has a minimum, the solution for that SFC is uncertain. As is evident from Fig. 1, there can, in some cases, be several possible solutions, due to the nonlinear and non-single-valued form of the theoretical color models.

4. ACCURACY OF TRANSLATING INTEGRATED COLORS INTO STAR-FORMATION PARAMETERS

To determine three star-formation parameters for an SFC (α, $M_{\max}$, and t), it is sufficient to know three observed colors, if the chemical composition is known from observations [see the system of equations (1)]. If more input parameters are available, e.g., the four integrated colors $(U{-}B)_{\text{obs}}$, $(B{-}V)_{\text{obs}}$, $(V{-}R)_{\text{obs}}$, and LCI$_{\text{obs}}$, then five combinations of input data values can be constructed, yielding five independent estimates of the star-formation parameters:

1) $U{-}B$, $B{-}V$, $V{-}R$, LCI;
2) $U{-}B$, $B{-}V$, LCI;
3) $B{-}V$, $V{-}R$, LCI;
4) $U{-}B$, $V{-}R$, LCI;
5) $U{-}B$, $B{-}V$, $V{-}R$.

All four integrated characteristics and the chemical composition are known for 50 SFCs. For these SFCs, we used all five combinations of input data to derive five solutions for α, $M_{\max}$, and t. The number of SFCs in each of the five solution samples (α, $M_{\max}$, t) is different, since it was not possible to obtain unambiguous solutions for all five color combinations for some of the 50 objects.

We now use a pairwise comparison of the parameters derived from different color combinations to estimate the accuracy of the inferred star-formation parameters for each of the five color combinations. Let n_{ij} be the number of SFCs for which there are solutions based on the ith and jth color combinations. Note that n_{ij} is always less than or equal to 50. We now compute the

differences of the star-formation parameters derived from different color combinations for each of the SFCs:

$$\Delta_1(\alpha_{ij}) = \alpha_i - \alpha_j,$$

$$\Delta_1(M_{ij}) = M_i - M_j,$$

$$\Delta_1(t_{ij}) = \log t_i - \log t_j.$$

The subscript $l = 1, \ldots, n_{ij}$ is the number of the SFC. Before proceeding further with the analysis, we must make sure that the parameter values derived using the various methods are unbiased. To this end, we computed the means of each of the parameters and their standard errors; for example, for the parameter α, we compute the means $\Delta\alpha_{ij} = \dfrac{1}{n_{ij}}\sum_{l=1}^{n_{ij}} \Delta_1(\alpha_{ij})$ and errors

$$\Delta(\alpha_{ij}) = \sqrt{\frac{\sum_{l=1}^{n_{ij}} [\Delta_1(\alpha_{ij}) - \Delta\alpha_{ij}]^2}{n_{ij}(n_{ij}-1)}}.$$ We found the resulting values to be unbiased. Since the means of the differences $\Delta_1(\alpha_{ij})$ are zero, their dispersions are given by the formula

$$\sigma_{\alpha_{ij}}^2 = \frac{\sum_{l=1}^{n_{ij}} [\Delta_1(\alpha_{ij})]^2}{n_{ij}-1}.$$

The variances of other parameters can be determined in the same way. We will assume that the dispersions of the pairwise differences are independent. Then, for each i and j, we have $\sigma_{\alpha_i}^2 + \sigma_{\alpha_j}^2 = \sigma_{\alpha_{ij}}^2$. Given the pairwise dispersions for all color combinations, $\sigma_{\alpha_{13}}^2$, $\sigma_{\alpha_{14}}^2$, $\sigma_{\alpha_{15}}^2$, $\ldots$, $\sigma_{\alpha_{45}}^2$ we have ten equations in the five unknown dispersions σ_{α_i} ($i = 1, 2, \ldots, 5$) of parameter α for each combination of color indices. We estimated the errors in the other two star-formation parameters in the same way.

Table 1 gives the dispersions of the IMF slope α and upper mass limit $M_{\max}$ and age t of the SFC determined using the five combinations of observed colors. In our subsequent determination of the star-formation parameters of extragalactic SFCs, we used all available observed colors and their combinations. The mean expected errors in the star-formation parameters derived via the conversion of the observed colors in the framework of the evolutionary models considered are taken to be (for adopted errors for the input data $\sigma_{\text{obs}} = 0.15^m - 0.25^m$ and $\sigma_z/Z = 50\%$)

$$\sigma_\alpha = 0.51 \pm 0.03, \quad \sigma_{M_{\max}} = 33 \pm 2 M_\odot, \quad \sigma_t = 0.29 \pm 0.03.$$

5. OBSERVATIONAL DATA

5.1. Integrated Colors

In [14], we compiled a catalog of the multicolor photometry of 836 SFCs in 49 spiral and irregular galaxies. All observations were reduced to the standard *UBVR* LCI system. We subtracted the contribution of the Galaxy from the observed SFC brightnesses for all samples considered, so that the catalog gives the characteristics of the intrinsic emission of the SFCs. We excluded measurements in which the fluxes of SFCs were not distinguished from the fluxes of the galaxies in which they lie since these cannot be correctly compared to the results of other studies. Our analysis of the accuracy of color indices measured in various studies indicated that it ranged from 0.15^m to 0.20^m [14]. In [14], we compare the observed colors of star-forming complexes (reduced to a single photometric system and corrected for interstellar extinction) to theoretical color indices on $(U–B)–(B–V)$, and LCI–$(U–B)$, LCI–$(B–V)$ color–color diagrams for a wide range of star-formation parameters. The region occupied by the theoretical colors describes satisfactorily the observed distribution of SFC colors.

We demonstrated the presence of selection effects in the observational data considered. The integrated SFC colors corrected for extinction and emission by gas can be translated into star-formation parameters in the framework of a given star-formation model if the chemical composition (which is known from observations) is fixed. See [14] for a detailed discussion of the catalog and a complete list of references.

5.2. Chemical Composition

We used spectroscopic data to correct for extinction and determine the chemical compositions of the SFCs. Analysis of the chemical compositions of spiral and irregular galaxies is currently an active area of research. The recent review [19] provides data on the chemical compositions of 39 spiral galaxies, in which at least five SFCs (HII regions) were observed. We expanded this list to 48 spiral and irregular galaxies.

Table 2 gives a list of the galaxies in which chemical compositions of individual giant HII regions have been measured, together with references to the original observations. The first three numbers in parentheses following a reference give the number of individual HII regions with measured [OIII] $\lambda\lambda$ 4959, 5007 and [NII] $\lambda\lambda$ 6548, 6583 line-intensity ratios and extinctions A_v. The fourth number, given for some references, is the number of objects with measured H_α and H_β emission fluxes. All these studies provide evidence for chemical abundance gradients in the disks of spiral galaxies. The metal abundances at the center and periphery differ by, on average, a factor of ten.

The observations of relative emission-line intensities in individual complexes are subject to both random and systematic errors. However, the extensive collected spectroscopic data on SFCs enables a comparative analysis of the observed parameters. A comparison of the observations of emission-line intensities for individual SFCs obtained in different studies showed that they are essentially free of systematic errors. Consequently, differences are nearly completely due to random errors, making it possible to estimate the external accuracy of individual observations. Recall that here we are referring to the accuracy of the mean chemical composition of a SFC, since different observations can correspond to different parts of an HII region.

Table 3 gives the estimated errors of individual observations derived from pairwise comparisons of line intensities for individual objects in galaxies, in the same way as is described in Section 3. We can see from Table 3 the ranges of the accuracies in the oxygen ([OIII]/H_β) and nitrogen ([NII]/H_β) relative line-intensity measurements and the extinctions A_v. The errors in [OIII]/H_β are lower than those in [NII]/H_β, since selective extinction influences the relative oxygen line intensity only weakly. The accuracy in A_v (derived from the Balmer decrement) is often low, due to the uncertainties in joining (calibrating) the blue and red spectrograms.

The accuracy estimates from various studies have typical dispersions $\Delta\sigma_i = 0.05, 0.15,$ and 0.5 for [OIII], [NII], and A_v, respectively. Therefore, to characterize the accuracy of individual measurements, we introduce classes with the following accuracies, which will be convenient to use in our subsequent analysis:

Class I includes [OIII]/H_β observations with $\sigma_i = 0.00–0.05$ (in units of the logarithm of the intensity);

Class II includes [OIII]/H_β observations with $\sigma_i = 0.05–0.10$;

Class III includes [OIII]/H_β observations with $\sigma_i = 0.10–0.20$;

Class IV includes [OIII]/H_β observations with $\sigma_i = 0.30–0.50$.

We subdivide the [NII] line measurements into classes with the following individual accuracies:

Class I—$\sigma_i < 0.10$;

Class II—$\sigma_i = 0.10–0.15$;

Class III—$\sigma_i = 0.15–0.20$;

Class IV—$\sigma_i = 0.30–0.50$.

To derive metallicities Z from the observed relative line intensities, we used semi-empirical relations between the relative oxygen and nitrogen line intensities and the metal abundances in the SFCs relative to the solar abundance ($Z_\odot = 0.017$) determined in [54].

5.3. Extinction in the SFCs

The absorption of light corresponding to the Balmer decrement of the emission of ionized gas in an SFC characterizes the extinction of gaseous and not stellar emission. In their analysis of the differences between the extinction of stellar and gaseous emission in HII regions in the LMC, Caplan and Deharveng [55]

Table 2. Galaxies with chemical composition studies

Galaxy	References*	Galaxy	References*
NGC 55	[20] (7, 7, 7)	NGC 3344	[26] (5, 0, 0, 5), [19] (9, 0, 9, 9)
NGC 157	[21] (9, 9, 9)	NGC 3351	[26] (3, 3, 3, 4), [34] (6, 0, 6, 6)
NGC 224	[22] (8, 8, 8), [23] (21, 24, 23, 23)	NGC 3521	[19] (10, 0, 10, 10)
NGC 253	[20] (8, 12, 10)	NGC 3621	[19] (7, 0, 7, 7)
NGC 300	[20] (13, 13, 14), [24] (6, 6, 6, 3) [25] (13, 0, 15, 14)	NGC 4254	[26] (5, 7, 7, 8), [46] (3, 3, 3, 3)
NGC 598	[26] (4, 4, 4, 4), [27] (12, 11, 12), [28] (7, 6, 7, 5), [29] (42, 0, 0), [30] (30, 8, 8, 8), [31] (80, 0, 0), [32] (24, 0, 0, 36)	NGC 4258	[19] (9, 0, 9, 9), [34] (11, 0, 11, 11)
NGC 628	[26] (7, 6, 6, 7), [33] (132, 132, 132, 132)	NGC 4303	[46] (6, 10, 10, 9), [47] (12, 12, 12), [48] (79, 79, 79, 79)
NGC 772	[34] (1, 0, 1, 1)	NGC 4321	[26] (4, 6, 6, 5), [46] (5, 5, 5, 5)
NGC 925	[19] (9, 0, 9, 9), [21] (8, 8, 8)	NGC 4449	[49] (18, 14, 0)
NGC 972	[21] (30, 31, 31)	NGC 4559	[19] (20, 0, 20, 20)
NGC 1068	[34] (4, 0, 4, 4)	NGC 4725	[19] (8, 0, 8, 8)
NGC 1084	[21] (5, 5, 7)	NGC 4736	[26] (2, 0, 0, 2), [34] (9, 0, 9, 9)
NGC 1313	[35] (6, 6, 6)	NGC 5033	[19] (8, 0, 8, 8)
NGC 1365	[24] (3, 3, 3), [36] (6, 6, 6, 6)	NGC 5055	[26] (5, 4, 4, 5)
NGC 1566	[37] (7 objects), [38] (5, 5, 5, 5)	NGC 5194	[26] (4, 2, 2, 4), [50] (4, 6, 6, 6), [39] (15, 15, 15), [21] (9, 9, 9), [40] (13, 0, 0, 0)
NGC 2460	[34] (2, 0, 2, 2)	NGC 5236	[20] (6, 18, 15), [51] (8, 8, 8)
NGC 2403	[26] (6, 6, 6, 6), [27] (8, 6, 8), [21] (13, 12, 13), [40] (264, 0, 0), [41] (5, 5, 5, 5)	NGC 5253	[49] (10, 10, 10, 10)
NGC 2841	[34] (1, 0, 1, 1)	NGC 5457	[26] (6, 8, 8, 6), [39] (14, 13, 14), [52] (6, 6, 5, 6), [25] (6, 0, 6, 6), [53] (3, 3, 3), [40] (81, 0, 0)
NGC 2903	[26] (6, 7, 7, 7), [19] (20, 0, 20, 20), [21] (5, 6, 5)	NGC 6384	[34] (9, 0, 9, 9)
NGC 2997	[26] (1, 0, 0, 1), [42] (49, 49, 49), [43] (8, 8, 8)	NGC 6946	[26] (6, 7,7, 7), [33] (166, 159, 166, 166)
NGC 3031	[34] (1, 0, 1, 1), [44] (17, 18, 18, 18), [45] (10, 10, 2)	NGC 7331	[19] (2, 0, 2, 2), [34] (6, 0, 6, 6)
NGC 3184	[26] (5, 6, 6, 6), [19] (10, 0, 10, 10)	NGC 7793	[20] (20, 17, 20), [26] (4, 2, 3, 5)
NGC 3198	[19] (15, 0, 15, 15)	IC 342	[26] (4, 5, 5, 5)
NGC 3319	[19] (13, 0, 13, 13)	He 2-10	[25] (3, 0, 3, 3)

* See text for an explanation of the numbers in parentheses following the references.

showed that the extinction derived from the observed Balmer decrement (A_v^{gas}) systematically exceeds the extinction of the stellar emission (A_v^*) in the same HII region: $A_v^* < A_v^{\text{gas}}$. The two-dimensional spectrophotometric map of the central region of NGC 4214 constructed by Maiz-Apellaniz *et al.* [56] shows that the stars, gas, and dust clouds in the brightest SFCs near the Galactic nucleus are spatially separated. The dust is concentrated at the edges of the region of ionization and primarily influences nebular emission lines, whereas the stellar continuum is located in a region that is relatively free of dust and gas. This spatial segregation could explain the observed discrepancy in the extinctions for emission lines and the stellar continuum. Indeed, Maiz-Apellaniz *et al.* [56]

found that the Balmer line peaks are located several arcseconds from the star cluster. Moreover, reddening is strongest in regions of Balmer line emission and somewhat weaker in front of the star cluster. Mas-Hesse and Kunth [6] showed that, in a number of galaxies, the color excesses $E(U–B)$ inferred from Balmer line intensity ratios systematically exceed those based on the UV continuum. This could indicate clumpiness in the distribution of the absorbing material in the SFCs.

Because estimates A_v^{gas} systematically exceed the extinction of the stellar continuum A_v^*, correcting the observed colors of stars in an SFC based on the Balmer extinction would artificially shift their colors toward the blue, distorting the star-formation parameters derived

Table 3. Accuracy of individual measurements of [OIII] and [NII] lines and of A_v in extragalactic HII regions

References	[OIII] line		[NII] line		A_v	
	class	σ_i	class	σ_i	class	σ_i
[19]	IV	0.23			III	0.68
[20]	III	0.013			III	0.56
[22]	III	<0.13	II	<0.11	II	0.46
[23]	III	<0.13	II	<0.11	II	0.46
[24]	II	0.070			III	0.85
[25]	I	0.030 ± 0.016			II	0.47 ± 0.13
[26]	I	0.04 ± 0.02	II	0.14 ± 0.08	I	0.28 ± 0.10
[27]	II	0.12 ± 0.03	III	0.16	III	0.53
[28]	II	0.10 ± 0.03	II	0.14	II	0.41
[29]	III	0.11 ± 0.04				
[30]	II	0.09 ± 0.04	II	0.14 ± 0.04	II	0.36 ± 0.13
[31]	I	0.010 ± 0.05				
[32]	IV	0.26 ± 0.06				
[33]	IV	0.35	IV	0.67	III	0.94
[34]	III	0.18			II	0.46
[39]	II	0.06 ± 0.03	II	0.14 ± 0.07	II	0.45 ± 0.11
[40]	II	0.08 ± 0.04				
[41]	II	0.08 ± 0.08	II	0.04	I	<0.19
[42]	III	<0.19	I	<0.07	II	<0.35
[43]	III	<0.19	I	<0.07	II	<0.35
[44]	III	<0.15	I	<0.07		
[45]	III	<0.15	I	<0.07		
[46]	IV	0.37	IV	0.46	I	0.25
[47]	III	0.18	II	0.10	I	0.30
[48]	III	0.17	II	0.11	I	0.28
[52]	I	0.027 ± 0.008	II	0.11	I	0.27 ± 0.06
[53]	I	0.042 ± 0.012	III	0.15	III	

from these colors. In practice, only the extinction of line emission has been determined for most of the SFCs, and it would therefore be useful to have an empirical relation between the Balmer extinction of gaseous emission and reddening of the stellar continuum.

In [57], we empirically analyzed the relation between the Balmer absorption of gaseous emission and the extinction of stellar light in HII regions in M33, NGC 2403, and the LMC. This required independent estimates of the extinction in emission lines and in the stellar continuum in individual SFCs. The LMC is the only Galaxy with independent measurements of the gaseous and stellar extinction in SFCs [55]. In the case of M33, we have measurements of the luminosities and colors of the brightest stars [58], as well as observations [25, 26] of HII regions that provide information about

their chemical composition, Balmer line intensities, and positions in the Galaxy. We used the observed brightnesses and colors of stars in SFCs in M33 [58] to determine the extinction for their stars using the technique described in [57]. In this way, we determined the extinctions A_v^* for 30 stars in eight associations in M33. We then compared the stellar and gaseous extinction in six complexes in M33, 32 complexes in the LMC, and one object in NGC 2403 to derive an empirical relation between A_v^* and A_v^{gas}, which can be fit satisfactorily by a linear relation, both separately for M33 and the LMC and for the combined sample of SFCs in the three galaxies:

$$A_v^* = (0.17 \pm 0.02) + (0.62 \pm 0.12)A_v^{\text{gas}}.$$

The correlation coefficient is $r = 0.81$.

Allowance for Galactic extinction in the directions of M33, NGC 2403, and the LMC yields the relation

$$A_v^* = (1 - b)A_v^{\text{Gal}} + bA_v^{\text{gas}},$$

where A_v^{Gal} is the Galactic extinction in the direction toward the object in question and $b = (0.65 \pm 0.10)$.

We added the data for M33 and NGC 2403 to those for the LMC not only to improve the sample statistics, but also because the first two galaxies have a different morphological type: they are spirals, whereas the LMC is irregular.

We divide the measurements of A_v into classes with the following individual accuracies:

Class I—$\sigma_i < 0.30$,

Class II—$\sigma_i \in (0.30–0.50)$,

Class III—$\sigma_i > 0.5$.

An error of $\pm 0.5^m$ in the inferred extinction increases the standard error in the observed color indices to 0.25^m–0.30^m. We corrected the observed color indices for interstellar extinction using only A_v^* estimates with class I and II accuracies.

5.4. Contribution of Gaseous Emission to the Integrated Colors of SFCs

In [54], we constructed a semiempirical model for gaseous emission in SFCs (extragalactic HII regions) for use in the reduction of multicolor photometric and spectroscopic data in order to separate the gaseous and stellar components in the spectra and determine the physical and chemical conditions in the SFCs. The resulting semi-empirical model enabled the determination of the following SFC parameters from the observed fluxes in the $H_\alpha + NII$ band and the $[NII]/H_\alpha$, $[OIII]/H_\beta$, and H_α/H_β relative line intensities:

—metal abundance Z;

—emission measure ME;

—electron temperature T_e;

—interstellar extinction derived from the Balmer decrement A_v^{gas};

—number of Lyman continuum photons N_{LC}.

The model also made it possible to determine the contribution of gaseous emission to the observed fluxes in continuum bands and to separate out the purely stellar component. To estimate the flux F_0 of the purely stellar emission from the observed flux F in a given photometric band, we took into account the contribution of gaseous line emission, F', and gaseous continuum emission, F''; in this band:

$$F_0 = F - F' - F''.$$

Flux F'' can be derived from the z, ME, and T_e estimates using the formulas for spectral intensity near the boundaries of hydrogen series, free–free emission, and two-photon emission given in [59–61]. In our calculations, we summed the intensities of all lines in the band. We included a total of 18 main lines of the interstellar medium. Note that the gas usually contributed less than 4–7% of the total flux in the U, B, and V bands.

When calculating the number of Lyman continuum photons, N_{LC}, emitted by the SFC stars from the observed H_α fluxes, difficulties arose in connection with taking into account the ionizing flux that is absorbed directly by interstellar dust and does not participate in gas ionization. It was shown in [62, 63] that, on average, 30% of photons with wavelengths shorter than 912 Å are absorbed directly by dust in extragalactic HII regions. In our subsequent calculations we allowed for variations of the Lyman-photon fluxes exceeding the above values by 30–40%.

6. RESULTS

To convert the observed colors into star-formation parameters, we must know at least three colors, the metallicity, and the Balmer decrement for the given SFC. Of the 836 SFCs for which multicolor photometric data have been obtained, only 180 have all the required data. We obtained unambiguous solutions as described above in Section 2 for 113 SFCs in 22 spiral and irregular galaxies. The absolute magnitudes of individual SFCs cover a wide range, from -8^m to -19^m. This reflects the fact that individual SFCs can contain from 50 to 5.5×10^8 stars, and this determines the luminosity of the complex. Other characteristics of the SFCs also differ widely: the ratios of the SFC-to-solar metallicities vary from 0.16 to 6, and SFCs can be found both near the centers of galaxies and at distances of up to 0.7 Galactic radii.

Since the IMF is a statistical concept, it can be reliably determined if there are a sufficiently large sample of stars in the SFC. If the IMF is known, the number of stars that formed at the initial time ($t_0 = 0$) can be estimated given the initial luminosity L_{SFC} of the complex. The initial luminosity L_{SFC} can be estimated from the observed luminosity of the SFC in the framework of a particular evolutionary model for a stellar population with a given age t and IMF. Absolute magnitudes $M_B(\text{obs})$ are known for 110 of the 113 SFCs for which the ages t, IMFs, and star-formation regimes (simultaneous or continuous) have been determined based on the integrated colors.

The number of stars forming in the SFC at the initial time ($t_0 = 0$) for a given IMF (slope α and M_{max}) can be computed from the formula

$$N_{\text{SFC}} = A \int_{M_{\text{min}}}^{M_{\text{max}}} m^\alpha dm. \tag{5}$$

Table 4. Galaxies in which the IMF and ages of SFCs have been determined

NGC	Morphological type according to RC2	Number index T of the morphological type	Number index LC of the luminosity class	d, Mpc	Number of SFC
628	SAS5	5	1	7.2	4
1365	SBS3	3	2	10.0	8
1566	SXS4	4	2	15.2	1
2403	SXS6	6	5	3.2	7
2903	SXT4	4	2	7.5	8
2997	SXT5	5	1	8.5	3
3184	SXT6	6	3	7.6	4
3351	SBR3	3	3	9.0	2
4038	P	9	1	18.0	7
4254	SAS5	5	1	18.0	5
4303	SXT4	4	1	18.0	17
4321	SXS4	4	1	18.0	5
4449	IB9	10	5	4.3	9
5055	SAT4	4	3	6.8	2
5194	SAS4P	4	1	7.5	8
5253	I 0 P	0	6	2.0	1
6946	SXT6	6	1	5.0	5
IC 342	SXT6	6	2	2.7	2
LMC	SBS9	10	6	0.05	6

The normalization constant A is derived from the initial luminosity of the SFC:

$$L_{SFC} = A \int_{M_{min}}^{M_{max}} L^*(m) m^\alpha dm, \qquad (6)$$

where $L^*(m)$ is the stellar luminosity function in the B band [64]. We adopted a lower mass limit for the IMF of $M_{min} = 0.1 M_\odot$.

We used the following criterion to determine whether the number of stars in a SFC was sufficient to reliably infer the IMF parameters: at least three stars must exist in the mass interval from M_{min} to M_{max}. One hundred and five SFCs of the 110 with known luminosity in 20 galaxies satisfy this condition (Table 4). No luminosity data are available for three objects. We selected these 105 SFCs for further analysis.

6.1. Distribution of Star-Formation Parameters in SFCs

Table 5 gives parameters for Gaussian fits to the distributions of the slope and upper mass limit of the IMF and age t for the 105 SFCs. The IMF slopes range from –0.5 to –4.0. The mean slope is –2.42, which is close to estimates of this parameter for our own Galaxy. The dispersion σ_α(obs) = 0.9 exceeds the standard error ($\sigma_\alpha = 0.51$), suggesting that the IMF slopes of different

SFCs can differ significantly. The IMF slopes (α) determined by Mas-Hesse and Kunth [6] range from –1 to –3, with a mean somewhere between the Salpeter value of $\alpha = -2.35$ and the Scalo slope $\alpha = -2.85$. The maximum mass of the stars formed, M_{max}, ranges from 30 to $120 M_\odot$, with a mean of $74 M_\odot$.

The ages of the SFCs (on a logarithmic scale) range from 5.9 to 7.9. SFCs with the largest ages are characterized by prolonged star formation. The mean age of the SFCs is 7×10^6 years. The age dispersion is $\sigma_{\log t}$(obs) = 0.55, and exceeds the standard error, $\sigma_{\log t} = 0.29$. The mean age of the 45 SFCs in which bursts of star formation were observed is $4.5^{+4.5}_{-2.5}$ Myr, whereas the mean age of the 60 SFCs with continuous star formation is 10^{+30}_{-8} Myr. The scatter in the ages of the 14 regions of intense star formation analyzed by Mas-Hesse and Kunth [6] is much narrower: $\log t$ (t in years) ranges from 2.5 to 6.5. Recall that the sample of objects used by Mas-Hesse and Kunth [6] is biased toward young bursts, and these authors gave preference to the simultaneous star formation scenario. However, in the case of the remaining three regions, Mas-Hesse and Kunth [6] reliably identified continuous star-formation regimes lasting for at least 10–15 Myr.

Table 5. Parameters of the distributions of α, M_{max}, age t, and M_{SFC} for the 105 SFCs

Parameter	Interval of variation	Mean	Standard error	Accuracy of the method
α	−0.5–4.0	−2.42	0.91	0.51
M_{max}, $M_\odot$	30–120	74	20	33
$\log t$ [year]	5.9–8.0	6.84	0.55	0.29
$\log M_{SFC}$, $M_\odot$	3–11	6.99	1.76	0.90

6.2. Initial Masses of the SFCs

Given the luminosity of an object, the IMF parameters, age, and star-formation regime determined in our analysis are sufficient to compute the initial mass of stars in the SFC—the mass of gas converted into stars at the initial epoch of star formation (M_{SFC}):

$$M_{SFC} = A \int_{M_{min}}^{M_{max}} m m^\alpha dm. \qquad (7)$$

Here, the normalization constant A is computed in the same way as was done when determining the initial number of stars from the initial luminosity L_{SFC} via Eq. (5). Recall that the initial luminosity L_{SFC} can be derived from the observed luminosity in the framework of some evolutionary model if the IMF, age, and star-formation regime are known.

Table 5 shows the mass range, mean mass, and dispersion for the 105 SFCs studied. The initial SFC masses vary in a wide interval from 10^3 to $10^{11} M_\odot$, cor-

responding to a wide range of observed absolute magnitudes (from -7^m to -19^m) and initial luminosities (from -9^m to -22^m). The masses of the 17 star-formation regions analyzed by Mas-Hesse and Kunth [6] lie in a narrower interval, from 500 to $10^8 M_\odot$. However, they calculated masses M_{SFC} in a shorter IMF mass interval, starting from $2 M_\odot$ and not from $M_{min} = 0.1 M_\odot$ as in our case.

Using $M_{min} = 0.1 M_\odot$, we found the resulting masses of the biggest SFCs to be so large that these objects must be gravitationally bound. It would be appropriate to consider such objects as subgalaxies within the parent Galaxy. If we adopt $M_{min} > 0.1 M_\odot$, the resulting masses of the biggest SFCs are not large enough that they will be gravitationally bound. About 80% of the SFC luminosity comes from stars with masses higher than $4 M_\odot$, so that the star-formation parameters that we derive from the integrated colors correspond to the massive, upper part of the IMF ($M > 4 M_\odot$) of the complexes. The IMF could have a different slope for low-mass stars. If the low-mass, lower part of the IMF has a shallower slope than the upper, massive part, the inferred SFC mass would be substantially lower, even if $M_{min} < 0.1 M_\odot$.

7. DISCUSSION

Figure 2 shows the slope of IMF α plotted as a function of the initial luminosity M_B for two SFC groups with different masses. The two groups form two bands with equal slopes ($b \approx -0.24$): at a fixed initial mass M_{SFC}, the IMF slope becomes steeper as the initial luminosity of the SFC increases. The correlation coefficients between α and M_B are $r = 0.78$ and $r = 0.88$ for SFCs with masses from 10^5 to $3 \times 10^6 M_\odot$ (squares in Fig. 2) and from 3×10^5 to $10^6 M_\odot$ (circles), respectively.

SFCs with continuous star formation yield the following relation between M_B and metallicity (Fig. 3a):

$$M_B = -(8.98 \pm 0.97) - (4.59 \pm 0.59)(Z/Z_\odot),$$

where $Z_\odot = 0.017$ is the solar metallicity and the correlation coefficient is $r = 0.78$. The correlation between M_B and metallicity for SFCs with simultaneous star formation is very weak: the correlation coefficient is $r = 0.43$. When constructing the $M_B - Z/Z_\odot$ scatter diagram (Fig. 3), we excluded SFCs with $Z > 0.040$, since the evolutionary models for SFCs with continuous star formation we have used are sensitive to the metallicity and only cover the Z interval from 0.002 to 0.040.

Figure 3b shows the age–metallicity relation for SFCs with continuous star formation:

$$\log t = (5.65 \pm 0.15) + (0.84 \pm 0.09)(Z/Z_\odot)$$

with a correlation coefficient of $r = 0.83$. It is evident from Fig. 3b that the metallicities of complexes increase with the duration of the star formation. The weaker correlation for SFCs with simultaneous star formation ($r = 0.55$) reflects the inverse relation between metallicity and
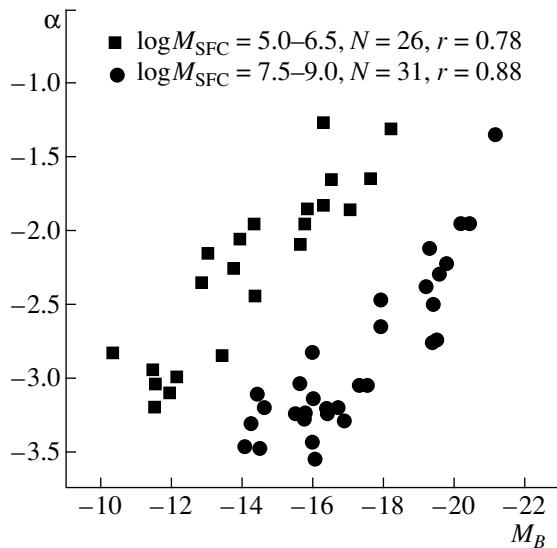
Fig. 2. "IMF slope–initial luminosity" diagram for two SFC groups with different masses. Squares and circles indicate SFCs with initial masses in the range 10^5 to $3 \times 10^6 M_\odot$ and 3×10^7 to $10^9 M_\odot$, respectively.
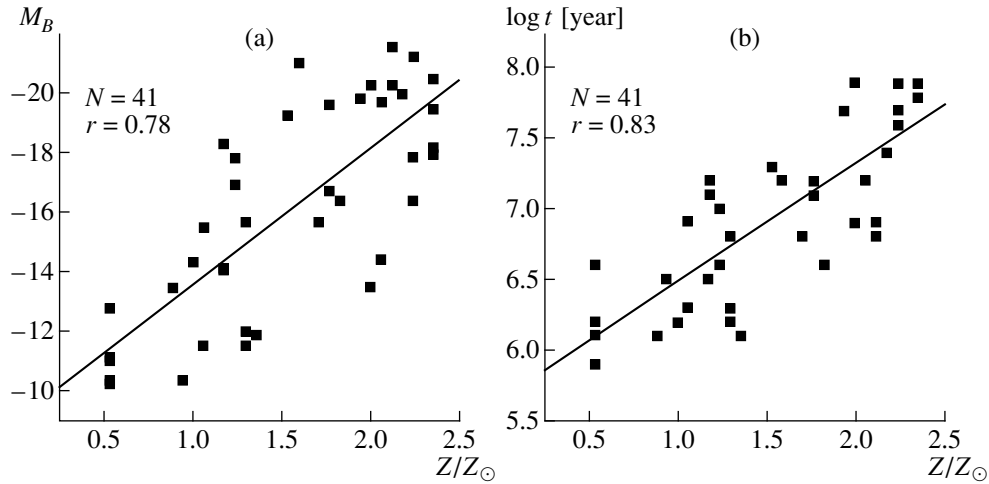
Fig. 3. (a) "Initial luminosity–metal abundance" and (b) "age–metal abundance" diagrams for SFCs with continuous star formation.

age: recent bursts of star formation are more metal-rich than old ones:

$$t \text{ (Myr)} \sim (8.1 \pm 1.2)(Z/Z_\odot)^{-(0.13 \pm 0.03)}.$$

This conclusion is in agreement with the results of Girardi *et al.* [65], who showed that the ages of star clusters in the LMC inferred in the framework of a simultaneous star-formation model are inversely proportional to metal abundance Z.

It is evident from Fig. 3 that the duration of a period of continuous star formation should depend on the initial luminosity of the complex (Fig. 4):

$$\log t = (4.73 \pm 0.26) - (0.14 \pm 0.02)M_B.$$

The corresponding correlation coefficient is $r = 0.80$. Figure 4 shows that the duration of star formation in a complex increases with the initial luminosity (mass) of the complex. This is in agreement with the results of Efremov and Elmegreen [66], who found the duration of star formation in complexes to increase with the size of the complexes. They showed that the age difference of cluster pairs in the LMC increases with their spatial separation, implying that the duration of star formation in a complex is correlated with its size. Of the SFCs considered here, linear sizes S have been estimated for 20 objects with continuous star formation and 23 with simultaneous star formation. The low accuracy of the linear sizes and the small sample sizes lead to a low degree of correlation between the ages and linear sizes of these complexes. Nevertheless, there is a weak but significant correlation ($r > 0.6$) between age t and size S in the SFC samples considered. The ages of SFCs with continuous star formation are a monotonically increasing function of the size S of the complex (Fig. 5):

$$t \sim 0.11 S^{1.02 \pm 0.30},$$

where t and S' are in Myr and pc, respectively. Young SFCs with simultaneous star formation are larger than older complexes with earlier bursts of star formation:

$$t \sim 2.09 \times 10^2 S^{-(0.72 \pm 0.20)},$$

where t and S' are in Myr and pc, respectively; $r = 0.61$. In the case of simultaneous star formation in an individual SFC, the decrease of its size with age could be due to a decrease in the number of massive O stars, which are the most important sources of radiation ionizing the ambient interstellar hydrogen. We used SFC sizes determined from plates taken with an H_α filter. In the case of continuous star formation, the size of the region encompassed by the wave of star formation increases with time, expanding the HII region and increasing the
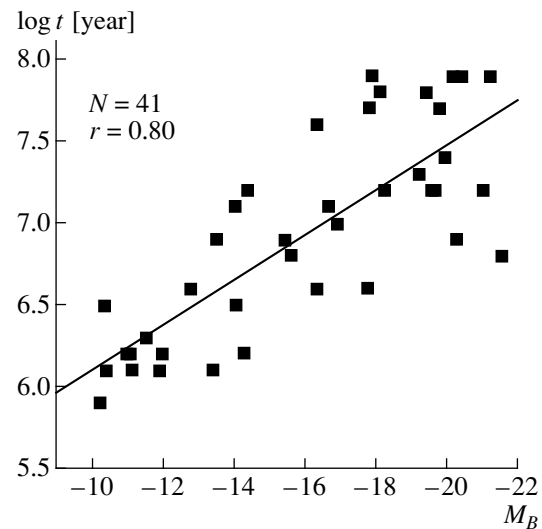
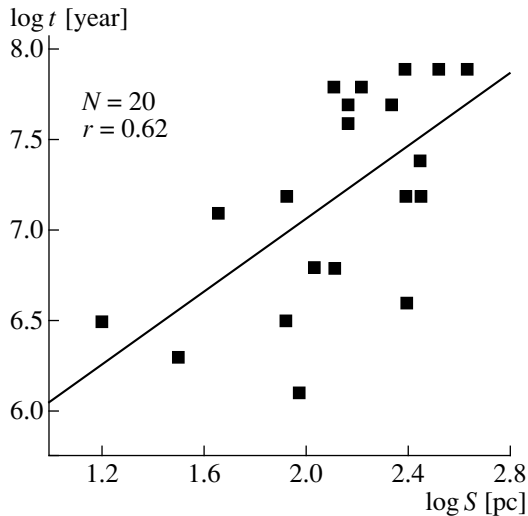**Fig. 4.** "Age–initial luminosity" diagram for SFCs with continuous star formation.

Fig. 5. "Age–size" diagram for the SFCs.

Fig. 6. Dependence of the IMF slope on the initial mass of the SFCs.

size of the SFC. The SFCs we studied are classical OB associations with typical scales of ~80 pc [67, 68]. Substituting this size into the above age–size relations yields typical ages of $t \sim 10$ and ~9 Myr for SFCs with continuous and simultaneous star formation, respectively, in agreement with typical ages for OB associations.

The linear sizes of the SFCs in the samples considered range from 20 to 400 pc. Efremov and Elmegreen [66] discuss the age–size relation for an entire spatial hierarchy of star-formation scales. Note that the large-scale regions of star formation, such as spiral-arm segments in galaxies, consist of numerous smaller star-formation regions with both continuous and simultaneous star formation. However, even if a large-scale stellar complex is dominated by smaller sites of simultaneous star formation with various ages, the overall pattern has the appearance of a continuous star-formation process [6].

In spite of the large scatter in the initial luminosities of the 105 SFCs studied, which range from -9^m to -22^m, the dependence of the IMF slope α on the mass M_{SFC} of the complex can be described by a single linear equation with correlation coefficient $r = 0.75$ (Fig. 6):

$$\alpha = (0.05 \pm 0.22) - (0.35 \pm 0.03) \log M_{SFC}.$$

Note that this functional dependence between α and M_{SFC} follows from our assumption of a power-law form for the stellar initial mass function, $f(m) \propto m^\alpha$. The scatter of the data points in Fig. 6 is determined by the scatter of the SFC luminosities. Recalculating the masses of 17 SFCs determined by Mas-Hesse and Kunth [6] for the entire range of the IMF mass interval from $M_{min} = 0.1 M_\odot$ to M_{max} yields for these SFCs a relation similar to that obtained above:

$$\alpha = (-0.60 \pm 0.61) - (0.27 \pm 0.10) \log M_{SFC}.$$

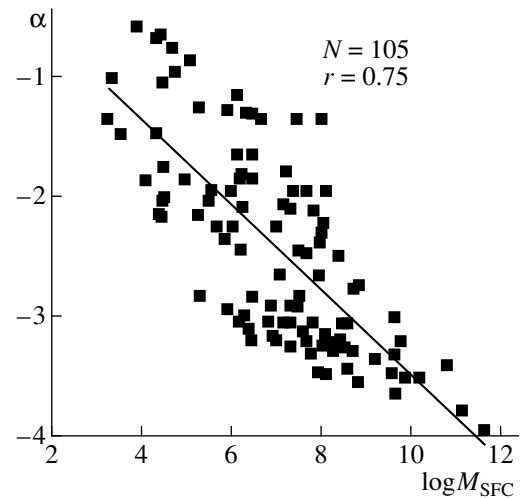The linear relation based on the sample of 105 SFCs can be used to predict the masses of individual SFCs if the IMF slope is known (from the observed color indices). It follows from the relation between the IMFs and masses of the SFCs that the integrated stellar IMF in a Galaxy constructed by counting the stars in all the SFCs is determined by the spectrum of the masses of the complexes populating the Galaxy. The observed universality of the integrated IMFs in different galaxies, whose slopes are close to the Salpeter value ($\alpha = -2.35$, could indicate that SFCs in different galaxies have similar mass distributions centered near $M_{SFC} \approx 7 \times 10^6 M_\odot$, which corresponds to the Salpeter IMF. The mean mass of the SFCs in the sample considered here, consisting of 105 objects in 20 galaxies, corresponds to an almost Salpeter IMF, with $\alpha = -2.40$. However, if we imagine a Galaxy populated exclusively by low-mass SFCs with masses $M_{SFC} < 7 \times 10^5 M_\odot$, the resulting integrated IMF would be relatively flat, with a slope $\alpha > -2$.

Differences in the IMFs in different galaxies must be due to differences in the corresponding SFC mass distributions. The SFC size and luminosity distributions have been constructed for different galaxies. In most cases, these distributions are power laws with slopes ranging from –1.5 to –2.8 [69–72]. The mass distribution of molecular clouds in the Galaxy can also be approximated by a power-law with slope –1.6 [73]. This means that, if the absolute value of the slope of the SFC mass distribution exceeds two, star formation in the Galaxy is dominated by the contribution of low-mass SFCs near the lower limit of their mass distribution. In this case, we might expect the Galaxy to have a relatively shallow IMF.

We plotted our objects on "initial luminosity–Galaxy type" and "initial luminosity–Galaxy luminosity class" diagrams (Fig. 7). It is evident from these diagrams that galaxies of different types and luminosities
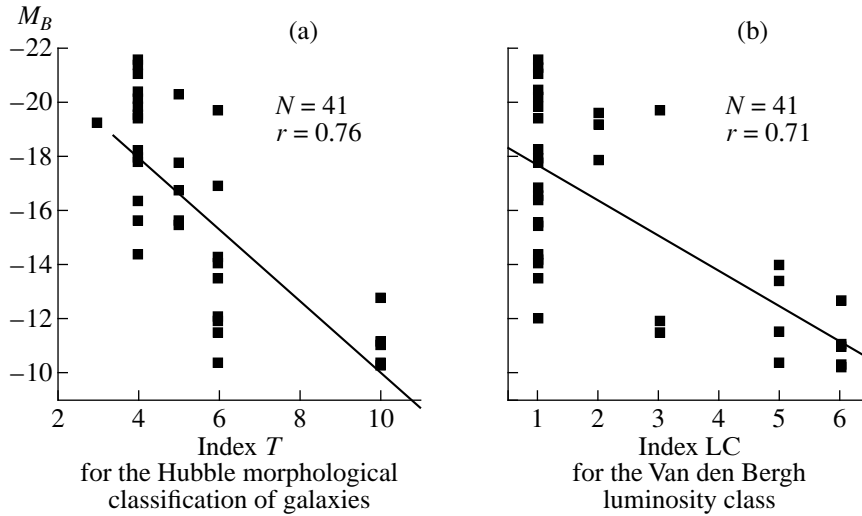
Fig. 7. (a) "Initial luminosity–Galaxy type" and (b) "initial luminosity–Galaxy luminosity class" diagrams for SFCs with continuous star formation.
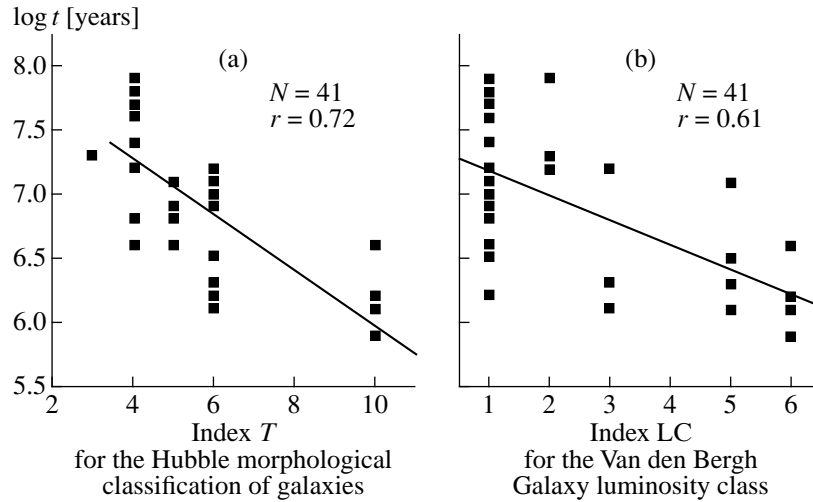
Fig. 8. (a) "Age–Galaxy type" and (b) "age–Galaxy luminosity class" diagrams for SFCs with continuous star formation.

are populated by complexes with different characteristic initial luminosities (masses). There is a tendency for the initial luminosity (mass) of SFCs with continuous star formation to decrease toward galaxies of later types and lower luminosity classes, with correlation coefficients $r = 0.76$ and $r = 0.71$, respectively.

Figure 8 shows "age–Galaxy type" and "age–Galaxy luminosity class" diagrams for the SFCs with continuous star formation. We can see the tendencies for the duration of star formation to increase toward galaxies of earlier morphological types and higher luminosity classes, with correlation coefficients $r = 0.72$ and $r = 0.61$, respectively.

We calculated the mean IMF upper mass limits M_{max} for three groups of SFCs with different masses:

—$M_{SFC} < 10^5 M_{\odot}$;

—$10^5 M_{\odot} < M_{SFC} < 10^9 M_{\odot}$;

—$M_{SFC} > 10^9 M_{\odot}$.

Figure 9 shows the dependence of the mean IMF upper mass limit (for each of the three groups considered) on the initial mass of the complex. The decrease of M_{max} toward more massive (brighter) complexes and the increase of the initial luminosity (mass) toward high-luminosity, earlier spirals (Fig. 7) agrees with the suggestion made in [74, 75] that Sa galaxies are characterized by reduced upper IMF limits. Our SFC sample contains no objects with infrared starburst events for which $M_{max} < 30 M_{\odot}$ [76].
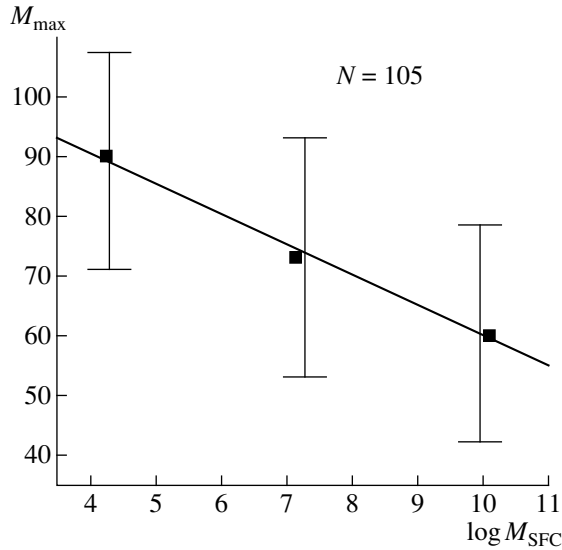
Fig. 9. The IMF upper mass limit $M_{\max}$ as a function of the SFC mass.

8. CONCLUSIONS

Our technique for translating the observed colors of SFCs into star-formation parameters proved an effective tool for studying star formation in extragalactic SFCs and enabled us to determine the IMF slopes and upper mass limits for a large sample of such objects. We were able to find unambiguous solutions for the star-formation parameters in nearly two-thirds of the SFCs. To derive these parameters, we must know at least three color indices (including the Lyman continuum index), the chemical composition, and the extinction of the SFC. The currently achievable accuracy of the observed quantities (0.15^m for measurements of the colors) is sufficient to determine the IMF slope, IMF upper mass limit, and the age of the SFC (on a logarithmic scale) with accuracies of ±0.51, $\pm33M_\odot$, and ±0.29, respectively. We performed all calculations in the framework of the evolutionary synthesis model of Piskunov and Myakutin [2].

The IMF slopes in complexes with different masses differ significantly: the IMF slope decreases monotonically as the SFC mass increases. We showed that the problem of the universality of the IMF in galaxies of different types can be solved only by investigating the mass distributions of SFCs and expanding Galaxy samples toward the earliest types of spirals and latest morphological types.

ACKNOWLEDGMENTS

REFERENCES

1. V. I. Myakutin, A. É. Piskunov, F. H. Sakhibov, and M. A. Smirnov, in *Abstracts of Poster Papers for the XXII IAU General Assembly*, Ed. by H. van Woerden (Twin, Sliedrecht, 1994).

2. A. É. Piskunov and V. Myakutin, Astron. Zh. **72**, 358 (1995) [Astron. Rep. **39**, 316 (1995)].

3. G. H. Rieke, M. J. Lebofsky, R. I. Thompson, *et al.*, Astrophys. J. **238**, 24 (1980).

4. J. Lequeux, M. Maucherat-Joubert, J. M. Deharveng, and D. Kunth, Astron. Astrophys., Suppl. Ser. **103**, 305 (1981).

5. E. B. Jensen, R. J. Talbot, and R. J. Dufour, Astrophys. J. **243**, 716 (1981).

6. J. M. Mas-Hesse and D. Kunth, Astron. Astrophys. 1999 (in press).

7. F. Viallefond and T. X. Thuan, Astrophys. J. **269**, 444 (1983).

8. R. Augarde and J. Lequeux, Astron. Astrophys., Suppl. Ser. **147**, 273 (1985).

9. R. Terlevich and J. Melnick, Mon. Not. R. Astron. Soc. **213**, 241 (1985).

10. J. M. Vilchez and B. E. Pagel, Mon. Not. R. Astron. Soc. **231**, 257 (1988).

11. J. Melnick, R. Terlevich, and P. P. Egglton, Mon. Not. R. Astron. Soc. **216**, 255 (1985).

12. K. Olofsson, Astron. Astrophys., Suppl. Ser. **80**, 317 (1989).

13. E. Bica, D. Alloin, and A. Schmidt, Mon. Not. R. Astron. Soc. **242**, 241 (1990).

14. F. Kh. Sakhibov and M. M. Smirnov, Astron. Zh. **76**, 419 (1999) [Astron. Rep. **43**, 361 (1999)].

15. E. E. Salpeter, Astrophys. J. **121**, 161 (1955).

16. V. Myakutin, Astron. Tsirk., No. 1553, 15 (1992).

17. Th. Schmidt-Kaler, *Landolt-Bernstein Numerical Data and Functional Relationships in Science and Technology* (Springer, Berlin, 1982), Vol. 2, p. 15, 453.

18. V. S. Avedisova, Astron. Zh. **56**, 965 (1979) [Sov. Astron. **23**, 544 (1979)].

19. D. Zaritsky, R. C. Kennicutt, and J. P. Huchra, Astrophys. J. **420**, 87 (1994).

20. B. L. Webster and M. G. Smith, Mon. Not. R. Astron. Soc. **204**, 743 (1983).

21. E. B. Jensen, K. M. Strom, and S. E. Strom, Astrophys. J. **209**, 748 (1976).

22. M. Dennefeld and D. Kunth, Astron. J. **86**, 989 (1981).

23. W. P. Blair, R. P. Kirshner, and R. A. Chevalier, Astrophys. J. **254**, 50 (1982).

24. B. E. Pagel, M. G. Edmunds, D. E. Blackwell, *et al.*, Mon. Not. R. Astron. Soc. **189**, 95 (1979).

25. S. D'Odorico, M. Rosa, and E. J. Wampler, Astron. Astrophys., Suppl. Ser. **53**, 97 (1983).

26. M. L. McCall, P. M. Rybski, and G. A. Shields, Astrophys. J., Suppl. Ser. **57**, 1 (1985).

27. K. B. Kwitter and L. H. Aller, Mon. Not. R. Astron. Soc. **195**, 939 (1981).

28. J. M. Vílchez, B. E. Pagel, A. I. Díaz, *et al.*, Mon. Not. R. Astron. Soc. **235**, 633 (1988).

29. D. Zaritsky, R. Elston, and J. M. Hill, Astron. J. **97**, 97 (1989).

30. L. Searle, Astrophys. J. **168**, 327 (1971).

31. J. Boulesteix, R. Dubout-Grillon, and G. Monnet, Astron. Astrophys. **104**, 15 (1981).

32. F. Viallefond and W. M. Goss, Astron. Astrophys. **154**, 357 (1986).

33. J. Belley and J.-R. Roy, Astrophys. J. Suppl. Ser. **78**, 61 (1992).

34. M. S. Oey and R. C. Kennicutt, Astrophys. J. **411**, 137 (1993).

35. B. E. Pagel, M. G. Edmunds, and G. Smith, Mon. Not. R. Astron. Soc. **193**, 219 (1980).

36. J.-R. Roy and J. R. Walsh, Mon. Not. R. Astron. Soc. **234**, 977 (1988).

37. S. A. Hawley and M. M. Phillips, Astrophys. J. **235**, 783 (1980).

38. J.-R. Roy and J. R. Walsh, Mon. Not. R. Astron. Soc. **223**, 39 (1986).

39. H. E. Smith, Astrophys. J. **199**, 591 (1975).

40. D. Zaritsky, R. Elston, and J. M. Hill, Astron. J. **99**, 1108 (1990).

41. J. Fierro, S. Torres-Peimbert, and M. Peimbert, Publ. Astron. Soc. Pac. **98**, 1032 (1986).

42. J. R. Walsh and J.-R. Roy, Astrophys. J. **341**, 722 (1989).

43. J. R. Walsh and J.-R. Roy, Mon. Not. R. Astron. Soc. **239**, 297 (1989).

44. D. R. Garnett and G. A. Shields, Astrophys. J. **317**, 82 (1987).

45. J. R. Stauffer and G. D. Bothun, Astron. J. **89**, 1702 (1984).

46. G. A. Shields, E. D. Skillman, and R. C. Kennicutt, Astrophys. J. **371**, 82 (1991).

47. R. B. Henry, B. E. Pagel, D. F. Lasseter, and G. L. Chincarini, Mon. Not. R. Astron. Soc. **258**, 321 (1992).

48. P. Martin and J.-R. Roy, Astrophys. J. **397**, 463 (1992).

49. F. Sabbadin, S. Ortolani, and A. Bianchini, Astron. Astrophys. **131**, 1 (1984).

50. A. I. Díaz, E. Terlevich, J. M. Vílchez, *et al.*, Mon. Not. R. Astron. Soc. **253**, 245 (1991).

51. R. J. Dufour, R. J. Talbot, and E. B. Jensen, Astrophys. J. **236**, 119 (1980).

52. J. F. Rayo, M. Peimbert, and S. Torres-Peimbert, Astrophys. J. **255**, 1 (1982).

53. G. A. Shields and L. Searle, Astrophys. J. **222**, 821 (1978).

54. F. Kh. Sakhibov and M. A. Smirnov, Astron. Zh. **67**, 472 (1990) [Sov. Astron. **34**, 236 (1990)].

55. J. Caplan and L. Deharveng, Astron. Astrophys. **155**, 297 (1986).

56. J. Maíz-Apellaniz, J. M. Mas-Hesse, C. Múñoz-Tunon, and H. O. Castanede, Astron. Astrophys. **329**, 409 (1998).

57. F. Kh. Sakhibov and M. A. Smirnov, Astron. Zh. **72**, 318 (1995) [Astron. Rep. **39**, 281 (1995)].

58. R. M. Humpreys and A. Sandage, Astrophys. J., Suppl. Ser. **44**, 319 (1980).

59. S. A. Kaplan and S. B. Pikel'ner, *Physics of the Interstellar Medium* (Nauka, Moscow, 1979).

60. K. R. Lang, *Astrophysical Formulae: a Compendium for the Physicist and Astrophysicist* (Springer, Berlin, 1974; Mir, Moscow, 1978), Vol. 1.

61. R. L. Brown and W. C. Mathews, Astrophys. J. **160**, 739 (1970).

62. L. F. Smith, P. G. Mezger, and P. Biermann, Astron. Astrophys. **66**, 65 (1978).

63. P. O. Mezger, Astron. Astrophys. **70**, 565 (1978).

64. C.W. Allen, *Astrophysical Quantities* (Univ. of London, Athlone, London, 1973).

65. L. Girardi, C. Chiosi, G. Berkelli, and A. Bressan, Astron. Astrophys. **298**, 87 (1995).

66. Yu. N. Efremov and Elmegreen, Mon. Not. R. Astron. Soc. **299**, 588 (1998).

67. P. B. Lucke and P. Hodge, Astrophys. J. **75**, 171 (1970).

68. Yu. N. Efremov, G. R. Ivanov, and N. S. Nikolov, Astrophys. Space Sci. **135**, 119 (1987).

69. F. Bresolin and R. C. Kennicutt, Jr., Astron. J. **113**, 975 (1997).

70. N. Caldwell, R. Kennicutt, A. C. Phillips, and R. A. Schommer, Astrophys. J. **370**, 526 (1991).

71. R. C. Kennicutt, B. K. Edgar, and P. W. Hodge, Astrophys. J. **337**, 761 (1989).

72. W. L. Freedman, Astrophys. J. **299**, 74 (1985).

73. J. P. Williams and C. F. McKee, Astrophys. J. 2000 (in press).

74. S. van den Bergh, Astron. J. **81**, 797 (1976).

75. J. Kormendy, in *The Evolution of Galaxies and Stellar Populations*, Ed. by B. M. Tinsley and R. B. Larson (Yale Univ. Obs., New Haven, 1977).

76. G. H. Rieke, K. Loken, M. J. Rieke, and P. Tamblyn, Astrophys. J. **412**, 99 (1993).

Translated by A. Dambis

The Synchrotron Spectra of Inhomogeneous Radio Sources

V. S. Artyukh and P. A. Chernikov

*Pushchino Radio Astronomy Observatory, Astro Space Center, Lebedev Institute of Physics,
Pushchino, Moscow oblast, 142292 Russia*

Abstract—Some features of the low-frequency cut-offs of synchrotron radio spectra are investigated using numerical simulations. It is demonstrated that the interpretation of the radio spectra of compact sources must be based on an exact (numerical) solution of the transfer equation. The need for creating VLBI systems operating at meter wavelengths to study the physical conditions in galactic nuclei is justified. © 2001 MAIK "Nauka/Interperiodica".

1. INTRODUCTION

The overwhelming majority of extragalactic radio sources have power-law spectra over a wide range of frequencies: $S \sim \nu^{-\alpha}$, where S is the source flux density, ν the frequency, and α the spectral index. In addition, the radio emission of many sources is partially linearly polarized; hence, the most probable and generally accepted mechanism for the nonthermal radio emission of extragalactic sources is synchrotron radiation by an ensemble of relativistic electrons with a power-law energy distribution $N(E) = N_0 E^{-\gamma}$, where $\gamma = 2\alpha + 1$ [1, 2].

Observations with very long base interferometry (VLBI) have shown that many compact radio sources have cut-offs of their spectra at low frequencies. At present, we know of four physical mechanisms for these low-frequency cut-offs; as shown in [3], the most probable mechanism for many radio sources in active galactic nuclei is synchrotron self-absorption. In this case, for homogeneous sources at low frequencies in the optically thick range, $S \sim \nu^{2.5}$ [4].

Homogeneous source models were widely used in the interpretation of radio spectra in the 1970s, when observational data were rather sparse, especially at low frequencies. In that situation, using a simple model to interpret the observations was quite natural. However, now, with the appearance of more accurate spectra, it has become clear that the overwhelming majority of sources are not well fit by homogeneous models, and other, more complex (i.e., inhomogeneous) models are needed to adequately interpret the observations.

Slysh [5] and Braude [6] were probably the first to indicate that the nonuniform distribution of the magnetic field and relativistic electron density in a source flattens the low-frequency cut-offs in the optically thick range (compared to $\alpha = 2.5$). Condon and Dressel [7] derived the spectra of inhomogeneous radio sources through numerical integration, and showed that the entire spectrum could be rather distinctly divided into three parts. At high frequencies, where the source is transparent, $S \sim \nu^{-\alpha}$. After reaching its maximum, the spectrum falls off and the low-frequency cut-off range can be divided into two parts: at the lowest frequencies, when the source is completely opaque, $S \sim \nu^{2.5}$, while, at intermediate frequencies, where the source is partially transparent, $S \sim \nu^{\alpha_{LF}}$, where $\alpha_{LF} < 2.5$.

Analytical expressions for the spectrum of an inhomogeneous source were obtained in [8, 9] and, as in [7], the gradients of the magnetic field and particle density were specified as power-law functions. These analytical expressions are approximate (in the general case, the transfer equation for an inhomogeneous source has no analytical solution), and it remains unclear to what extent these approximations are suitable for the interpretation of high-accuracy radio spectra.

Our present work is intended to elucidate this question. We will use model calculations to investigate the dependence of the shape of low-frequency cut-offs in the spectra of inhomogeneous radio sources on the character of the nonuniformity of the distributions of the magnetic field and relativistic particle density. In the process, we have compiled a catalog of theoretical spectra for use in the interpretation of radio astronomical observations of compact extragalactic sources and derived information about the physical conditions in the nuclei of the galaxies hosting these radio sources.

We have chosen power-law dependences for our analysis. If plasma flows outward from the center of a radio source, as in the solar wind, the magnetic field is stretched in the radial direction, and the magnetic intensity decreases as $1/r^2$; the plasma density follows the same law. If the magnetic field is dipolar, then $H \sim 1/r^3$. Thus, proceeding from physical considerations, we expect that the distributions of the magnetic field and relativistic particle density could plausibly obey power laws. Of course, in real radio sources, the non-uniformities in the distributions of the magnetic field and particle density could be arbitrary, and describing them with power-law functions is only a model approximation; however, this approximation is undoubtedly closer to the real situation than a homogeneous model.

In Section 2, we consider spectra for one-dimensional models of radio sources, suitable for describing the radio jets that emerge from the centers of galactic nuclei; these radio jets should not necessarily be narrow. In Section 3, we present spectra for spherically symmetric radio sources, i.e., sources with three-dimensional structures. In Section 4, we consider models in which the magnetic intensity and relativistic-electron density increase with distance from the source center. In Section 5, we calculate the source brightness distribution and frequency dependence of the source angular size. Finally, we discuss our results in Section 6.

2. ONE-DIMENSIONAL MODELS

Our first class of models are one-dimensional models of the radio jets that are symmetrically ejected from the center of a galactic nucleus. The radio jets consist of plane-parallel layers, and their properties vary only along the ejection direction. We assume that the magnetic intensity H and density of relativistic electrons N decrease with distance from the source center as

$$H(x) = H(0)\frac{1}{1 + k_H\left(\frac{|x|}{L}\right)^m},$$ (1)

$$N(x) = E^{-\gamma}N(0)\frac{1}{1 + k_N\left(\frac{|x|}{L}\right)^n}.$$ (2)

For $|x| > L$, $H(x) = 0$ and $N(x) = 0$. Here, L is the length of each jet. Factors k_H and k_N describe the fall-off of the magnetic field and particle density with distance from the center of the source. Note that the same power laws for $H(x)$ and $N(x)$ were considered in [7] but with different parameters:

$$H(r) = H(0)\frac{1}{1 + \left(\frac{r}{r_0}\right)^m} \quad \text{for} \ \ r < L,$$

$$H(r) = 0 \ \ \text{for} \ \ r \geq L,$$

where r_0 is the distance at which the field intensity drops by a factor of two. There is an obvious relationship between these parameters:

$$k_H = \left(\frac{L}{r_0}\right)^m.$$ (3)

This enables us to compare our results with those of [7]. In our opinion, parameter k_H describes the field distribution in a more transparent way than r_0.

In the absence of incident radiation, the solution of the transfer equation in the one-dimensional case is [10]

$$I(\nu) = \int_{-L}^{L} \varepsilon_\nu(x) e^{-\int_x^L \kappa_\nu(x')dx'} dx,$$ (4)

where ε_ν and κ_ν are the coefficients of emission and absorption. We consider the incoherent synchrotron emission of an ensemble of relativistic electrons. We also assume that the particle velocity distributions are locally isotropic at each point, so that we can adopt for the emission and absorption coefficients the angle-averaged expressions [2]:

$$\varepsilon_\nu = c_5(\gamma)NH_\perp^{\frac{\gamma+1}{2}}\left(\frac{\nu}{2C_1}\right)^{\frac{(1-\gamma)}{2}},$$ (5)

$$\kappa_\nu = c_6(\gamma)NH_\perp^{\frac{\gamma+2}{2}}\left(\frac{\nu}{2C_1}\right)^{\frac{-(\gamma+4)}{2}}.$$ (6)

Here, $c_5(\gamma)$ and $c_6(\gamma)$ are functions tabulated in [2] and C_1 is a constant, also given in [2].

We carried out calculations for three groups of models. In the first, only the magnetic field was varied, and the distribution of relativistic electrons was uniform. In the second group, the particle density was varied, whereas the magnetic field remained uniform. Finally, in the third group, both the particle density N and magnetic intensity H were varied in accordance with the same law.

We chose parameter values close to those expected for real radio sources, namely, $L = 50$ pc and $H(0) = 1$ G; we determined $N(0)$ from the condition that the source optical depth be unity at 1 GHz (in this case, the spectrum should peak near this frequency). Note that, in a number of studies, the frequency at which $\tau = 1$ is taken to be unity to emphasize the general character of the results obtained. Since the choice of the numerical values of these parameters does not affect the shape of the spectrum, we chose this frequency to be 1 GHz so that the calculated spectra would be close to observed spectra (for example, there is an entire class of "GHz-peaked spectrum" compact radio sources). The calculations were carried out for n (and m) = 1, 2, 3, and 4 (not only for the physically justified values $m = 2$ and 3) to trace the dynamics of changes in the spectra with changes in the magnetic field and particle distributions. Parameter k took on values of 10, 10^2, 10^3, 10^4, and 10^5. The labels by the curves in Figs. 1 and 3 correspond to the magnitude of $\log k$. We chose the integration step such that the computation error could be neglected, which we verified during the calculations.

Figure 1 presents the results of the calculations for the one-dimensional models. We can see that, at $\nu > 1$ GHz (the transparent range), the high-frequency part of the spectrum is completely independent of the magnetic-
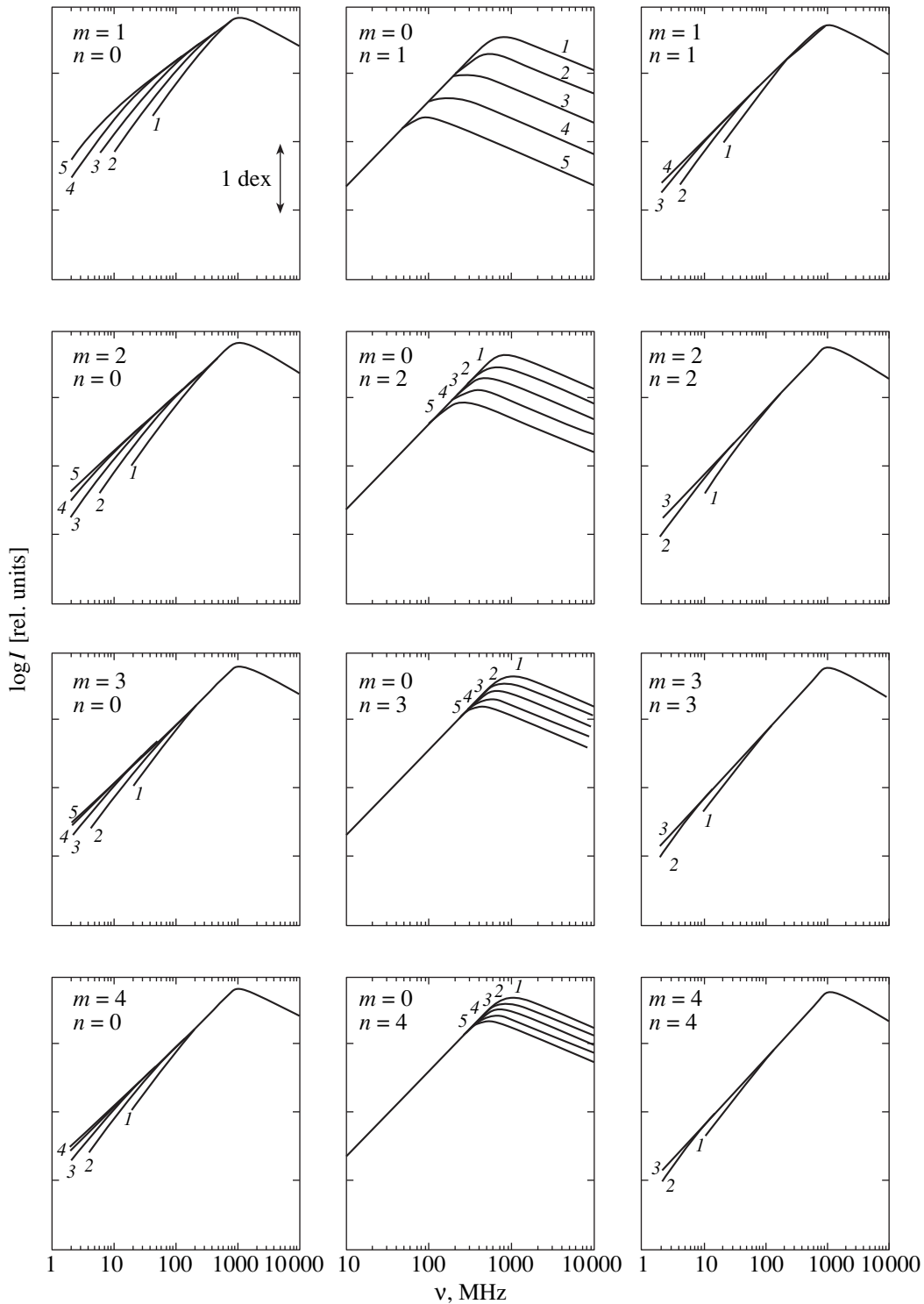
Fig. 1. Spectra of one-dimensional inhomogeneous synchrotron sources for $\gamma = 3$. The numbers of the curves correspond to the magnitude of $\log k$.

field and particle-density distributions: the spectrum always has the form $S \sim \nu^{-\alpha}$, where $\alpha = (\gamma - 1)/2$. In the models in which the magnetic intensity was varied (first column of Fig. 1) and both the field and particle density were varied (third column), between the maximum and

the quite steep low-frequency cut-off with spectral index 2.5, there is a section of the spectrum that is approximately power-law, but its spectral index $\alpha_{LF} < 2.5$. The spectral maxima of these models are slightly shifted toward higher frequencies ($\nu_m > 1$ GHz). In the models
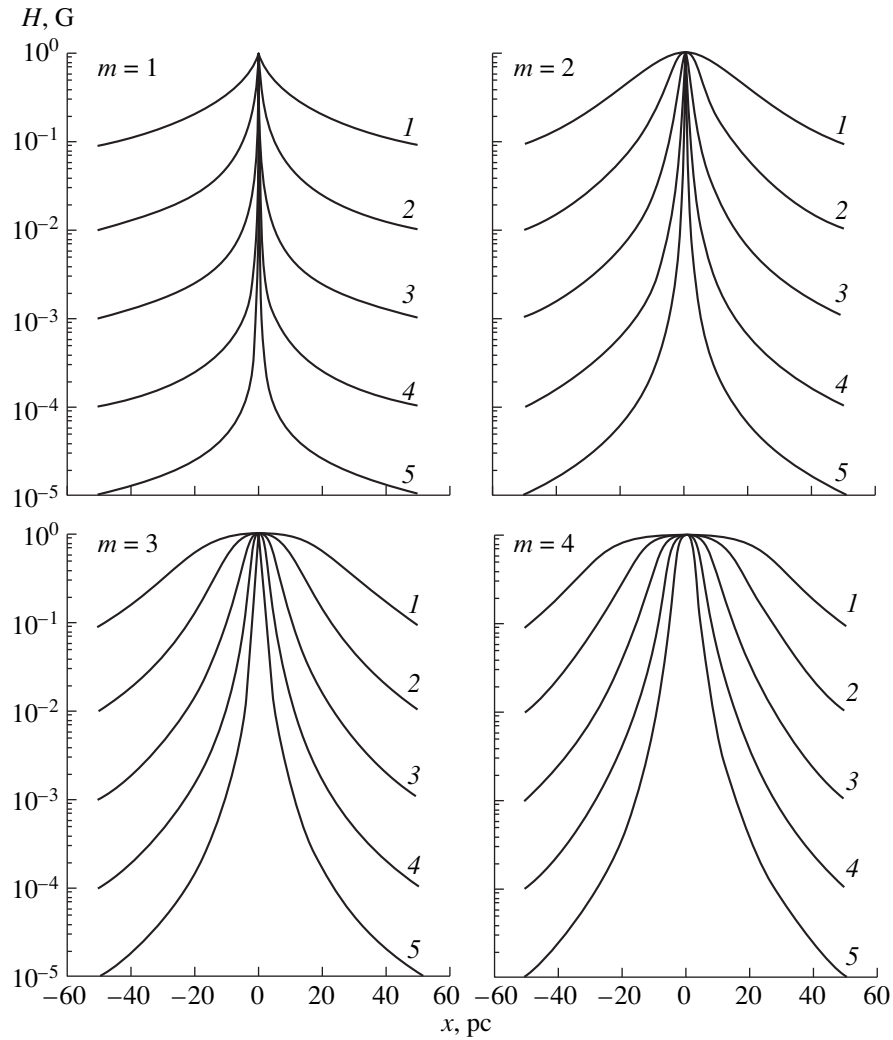
Fig. 2. Distributions of the magnetic field $H(x)$ [or density of relativistic particles $N(x)$] for which the theoretical spectra have been calculated.

where only the particle density was varied, while the magnetic field remained uniform (second column), the spectra of inhomogeneous and homogeneous sources are virtually the same, and the maxima are shifted toward low frequencies; this shift grows with increasing particle density gradient, i.e., with increasing k_N.

Note that, in most cases, the spectral maxima for homogeneous sources also do not coincide with the frequency at which $\tau = 1$. The optical depth at which the spectrum has its maximum ($\tau = \tau_m$) depends on γ [2]:

$$\gamma + 4 = 5\frac{(e^\tau - 1)}{\tau}. \qquad (7)$$

It follows that, in homogeneous sources with $\gamma < 4.6$, the spectral maxima are shifted toward high frequencies ($\nu_m > 1$ GHz).

Figure 2 shows the distributions of the magnetic field (or relativistic electron density) in the sources for

which these calculations were carried out. An important feature of the one-dimensional models is that all of their spectra have rather steep low-frequency cut-offs. The gentlest low-frequency cut-off has $\alpha_{\mathrm{LF}} = 1.26$ (for $n = 1$, $k = 10^5$, $\alpha = 0.5$).

3. SPHERICALLY SYMMETRIC MODELS

The second class of models consists of spherically symmetric models for the radio sources. Here, also, we specified the distributions of the magnetic field and particle density to be power laws:

$$H(r) = H(0)\frac{1}{1 + k_H\left(\dfrac{r}{R}\right)^m} \quad \text{for} \ \ r < R,$$

$$H(R) = 0 \ \ \text{for} \ \ r > R, \qquad (8)$$

$$N(r) = E^{-\gamma} N(0) \frac{1}{1 + k_N \left(\dfrac{r}{R}\right)^n} \quad \text{for} \quad r < R,$$

$$(9)$$

$$N(R) = 0 \quad \text{for} \quad r > R,$$

where R is the source radius. As in the first group, parameters m and n varied from 1 to 4 and k was varied from 10 to 10^5. The source luminosity is

$$P(\nu) = \int_0^R d^2\rho \int_{-a}^a dx \varepsilon(x,\rho) \exp\left(-\int_x^a dx' \kappa(x',\rho)\right), \quad (10)$$

where ρ is a vector perpendicular to the x axis (line of sight) and $a = \sqrt{R^2 - \rho^2}$.

We adopted the parameter values $R = 50$ pc and $H(0) = 1$ G; we found $N(0)$ from the condition that the optical depth along the diameter ($\rho = 0$) be unity at 1 GHz.

Figure 3 presents the results of the calculations for this group of models. We can see that, at high frequencies ($\nu > 1$ GHz), as in the one-dimensional case, the spectrum does not depend on the distributions of the magnetic field and relativistic particles. At low frequencies, in the partially transparent region, the shape of the low-frequency cut-off depends on the source parameters. In this case, m, n, and γ determine the value of α_{LF}, and variations of k change only the extent of this part of the spectrum: as k increases, the frequency interval for the transition region increases, but α_{LF} remains unchanged.

The spectral maxima are always shifted toward low frequencies relative to $\nu = 1$ GHz; in most cases, this shift is quite small, but it increases with γ. This shift is especially strong if H and N are varied simultaneously (third column of Fig. 3). Note that, when deriving an analytical expression for an approximate solution of the transfer equation, Marscher [9] assumed that the spectral maximum always fell at a frequency for which $\tau = 1$ along the diameter. Our calculations show that this assumption is only approximately correct, and sometimes is completely wrong.

For comparison, we present the spectrum of synchrotron emission of a homogeneous spherical source [11]:

$$S(\nu) = \frac{\varepsilon_\nu}{\kappa_\nu} \Omega \frac{\tau^2 - 2 + 2(1 + \tau)e^{-\tau}}{\tau^2}, \quad (11)$$

where $\tau = \kappa_\nu 2R$, $\Omega = \pi R^2/D^2$ is the source solid angle and D is the distance to the source. The high-frequency asymptotic of (11) for $\tau \longrightarrow 0$ is

$$S(\nu) \cong \frac{1}{D^2} \varepsilon_\nu \frac{4\pi R^3}{3}, \quad (12)$$

and the low-frequency asymptotic for $\tau \longrightarrow \infty$ is

$$S(\nu) \cong \frac{1}{D^2} \frac{\varepsilon_\nu}{\kappa_\nu} \pi R^2. \quad (13)$$

Thus, at high frequencies, the entire source volume radiates, while, at low frequencies, where $\tau \gg 1$, the emission comes only from a thin outer layer, and the observer sees the source as a uniformly luminous disk.

Proceeding from the condition that $dS/d\nu = 0$ at the spectral maximum, we obtain a relation between τ and γ [similar to (7) in the one-dimensional problem]:

$$\gamma + 4 = \frac{5e^\tau \tau^2 + 2(1 + \tau) - 2e^\tau}{4e^\tau - 2(\tau^2 + 2\tau + 2)}. \quad (14)$$

It follows that, in homogeneous sources with $\gamma < 3.34$, the spectral maxima are shifted toward high frequencies ($\nu_m > 1$ GHz).

The spectra for models in which only the relativistic particle density was varied (second column of Fig. 3) are virtually indistinguishable from that for a homogeneous sphere and, as in the one-dimensional case, the spectral maxima shift toward lower frequencies with increasing particle density gradient.

We should note one more result. When both H and N are varied, the low-frequency cut-offs are the steepest among the spherical models, but their spectral indices lie in a range $0.73 < \alpha_{LF} < 1.43$; i.e., the three-dimensional model spectra do not have very steep cut-offs. Thus, it should be possible to distinguish three-dimensional from one-dimensional structures using the shape of the low-frequency cut-off.

Note that models in which γ is two to three, the relativistic particles are distributed uniformly ($n = 0$), and the magnetic intensity decreases as $1/r^2$ ($m = 2$), have flat segments in their spectra ($\alpha_{LF} = 0$). We note especially the model with $\gamma = 3$, $n = 0$, $m = 2$, and $k = 10^4$. This model has a very broad flat section in its spectrum (covering about two orders of magnitude in frequency).

In the literature, two possible explanations for flat radio spectra are usually considered. The first is the particle energy distribution: when $\gamma = 1$, the emission spectrum is flat. However, it was noted early in [12] that forming such an ensemble of relativistic electrons would require extremely large amounts of energy, and is consequently improbable. The spectrum of relativistic particles may be not a power law at all, but instead, for example, Maxwellian. In this case, the emission maximum broadens compared to the maximum for a homogeneous source with a power-law particle distribution, but this broadening is not very great [13]. Note that, if the particle spectrum has a sharp cut-off at low energies (below E_0), the spectrum may be flat at frequencies below $\nu = 6 \times 10^{18} H E_0$. However, even if the particle distribution function has a form that yields a flat emission spectrum, is stable, and such a source can exist, it can still be distinguished from a self-absorbed synchrotron source. Since this type of spectrum is
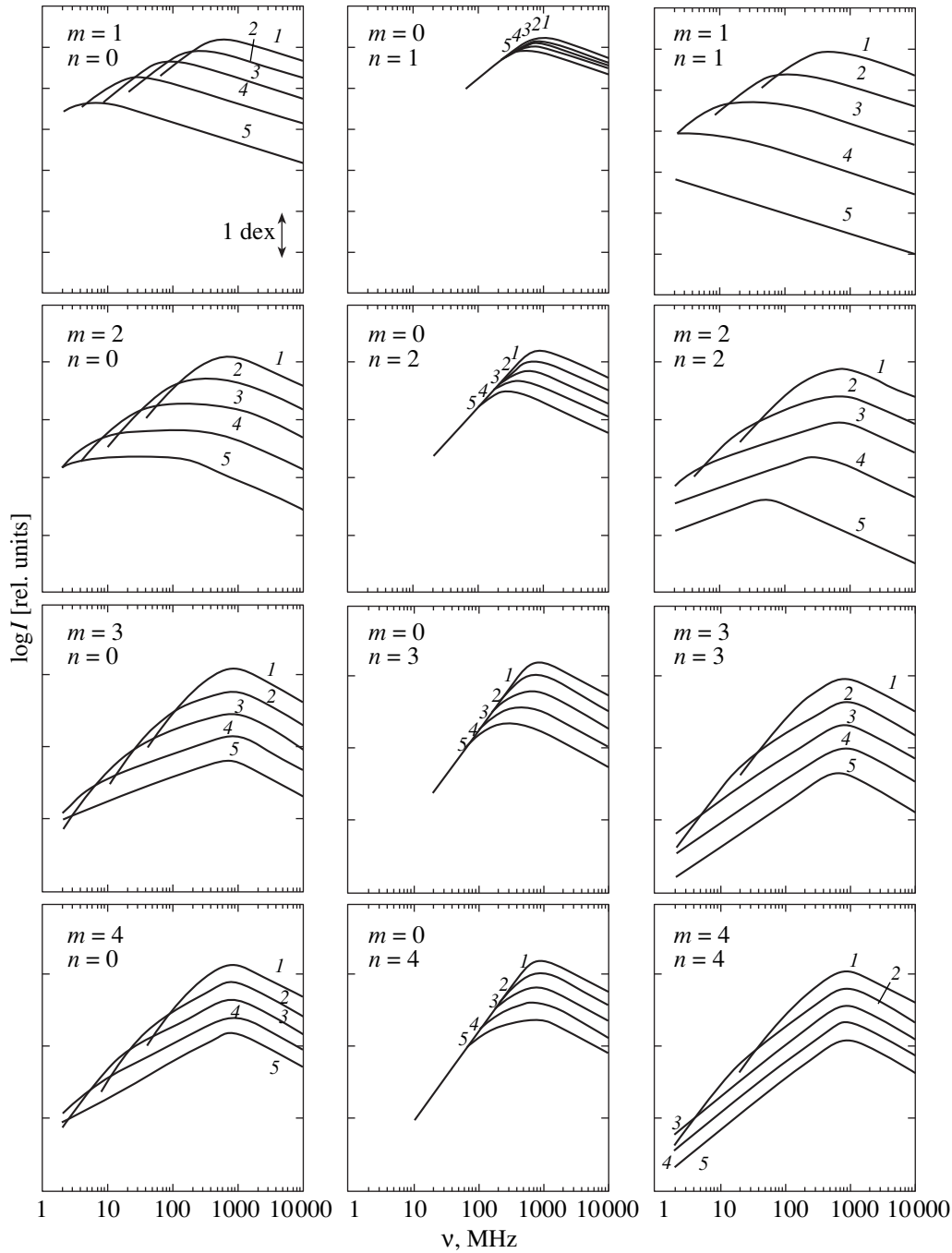
Fig. 3. Spectra of spherically symmetric inhomogeneous sources for $\gamma = 3$. The numbers of the curves correspond to the magnitude of $\log k$.

obtained at frequencies where the source is transparent, the brightness distribution of the source (and its angular size) will not depend on frequency, whereas the angular size of a self-absorbed source should vary at frequencies where the cut-off occurs (see Section 4).

Another possible explanation for flat spectra is that the compact radio source consists of several components with the usual spectrum for homogeneous sources. This possibility is often called the "cosmic conspiracy." Estimates show that, to obtain a flat spectrum, three to four homogeneous [14] or two to three inhomogeneous [7, 14] components are required. However, the total spectrum obtained in this way is not strictly flat, and has a wavy shape. It was noted in [12] that a situation in which all the components of a radio source have spectra with maxima of identical amplitude separated from each other by identical frequency
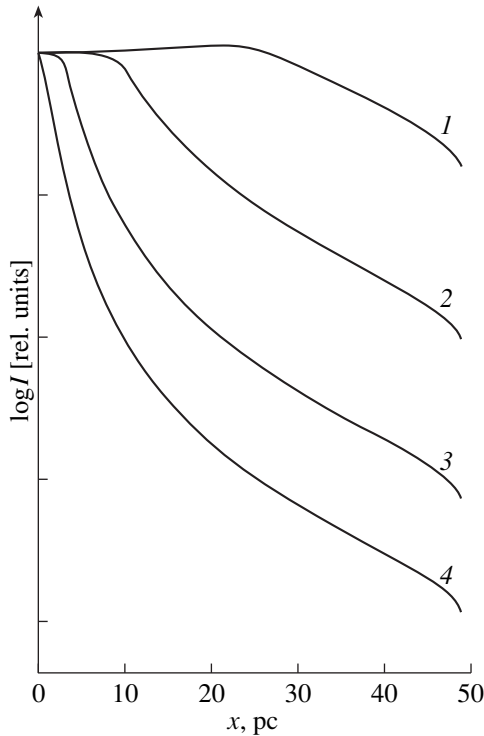
Fig. 4. Intensity distributions across the source at various frequencies: ν = (*1*) 10, (*2*) 50, (*3*) 500 MHz, (*4*) 5 GHz.

intervals is improbable. Furthermore, when there is only one unresolved radio feature on a map, all the compact components of the source must be arranged along the line of sight; this further decreases the plausibility of the "cosmic conspiracy."

Our model calculations show that there is no need for ultrahigh energy expenditures or artificial geometric structures. To obtain a flat spectrum, it is sufficient that the magnetic intensity in the source decrease with the distance from the center as $1/r^2$ and the particle distribution remain uniform.

4. MODELS WITH *H* AND *N* INCREASING WITH DISTANCE FROM THE CENTER

It follows from physical considerations that there can exist radio sources in which the magnetic intensity and relativistic particle density increase with distance from the source center. For example, a shock wave formed by some explosion at the center propagating outward and interacting with the interstellar medium can sweep up both plasma and magnetic field as it moves from the center. There are also theoretical models of active galactic nuclei in which the magnetic field increases with distance from the center of the source [15].

Ozernoy and Sazonov [16] obtained analytical expressions for the spectra of inhomogeneous sources in which the magnetic field either decreased or increased with distance from the center in accordance with a power

law. They concluded that the spectral indices must either increase or decrease compared to $\alpha = 2.5$ by identical amounts $\Delta\alpha$ near the low-frequency cut-off. On the other hand, the numerical calculations of [7] have shown that, when the magnetic intensity increases with distance from the center, the spectral index α_{LF} indeed becomes greater than 2.5, but only by a little. However, note that Ozernoy and Sazonov [16] considered a spherically symmetric source model, while the calculations in [7] were carried out for a one-dimensional source. Therefore, we decided to numerically model a spherically symmetric source in which the magnetic field and relativistic particle density increase from the center as

$$H(R) = H(0)\left[1 + k_H\left(\frac{r}{R}\right)^m\right], \qquad (15)$$

$$N(R) = E^{-\gamma}N(0)\left[1 + k_N\left(\frac{r}{R}\right)^n\right]. \qquad (16)$$

It turned out that the spectrum of such a source near the low-frequency cut-off becomes steeper than the spectrum of a homogeneous source, but only slightly. The maximum low-frequency spectral index is $\alpha_{LF} = 2.65$. Thus, we can conclude that, if the radio source has a very steep cut-off ($\alpha_{LF} > 2.7$), we are dealing not with synchrotron self-absorption but with some other mechanism, such as the Razin effect [4] or the presence of a thermal screen in the radio source.

5. THE $\theta(\nu)$ DEPENDENCE

In a number of studies, it has been noted that the brightness distribution of a radio source, and hence its angular size, should vary with frequency. Figure 4 shows the relative intensity distributions for a model source with $m = 2$, $n = 0$, and $k_H = 10^3$. Figure 5 presents calculated $R(\nu)$ dependences for two spherical models: $m = 2$, $n = 0$, $k_H = 10^{1/2}$ and $m = 2$, $n = 0$, $k_H = 10^{3/2}$. The quantity R is the half-maximum size of the source brightness distribution (central cross-section). The same figure shows the spectra for these models. We can see that the angular sizes of the sources are constant at both high and low frequencies. All changes in the source size take place in the same frequency interval as the change in the source spectrum; i.e., near the low-frequency cut-off. These results are fairly consistent with common sense. Indeed, at high frequencies, where the source is transparent, we see all the emitting regions, and its image is identical at all the frequencies. Therefore, the size does not change with frequency. However, with decreasing frequency, when part of the source becomes opaque, the observer sees increasingly fewer outer layers of the source (those that are still transparent). For this reason, its apparent size increases. At the lowest frequencies, where only a thin outer layer of the source emits, the source is seen as a uniformly luminous disk. Thus, the source size approaches the size of the entire emitting region; i.e., approaches a constant value. Note that this is also true for a homoge-

neous source, whose size should also increase with decreasing frequency, though only slightly and in a very narrow frequency interval.

When comparing model calculations with observations, we must take into account the fact that the angular sizes of sources estimated from VLBI observations are based on approximations of the true brightness distributions by Gaussian functions instead of power laws. Therefore, the measured angular size of the source should be corrected for this. This problem was considered to some extent in [9].

We note here one more circumstance. If the angular size of a source is considerably smaller than the interstellar scattering angle, we obtain from the observations an apparent angular size of the source θ that is equal to the interstellar scattering angle θ_s. Since $\theta_s \sim \nu^{-2}$ [17], we obtain a square-law dependence $\theta(\nu)$. However, this will not correlate with changes in the source spectrum (at the same frequencies) as will the $\theta(\nu)$ variation in an inhomogeneous source.

6. DISCUSSION

At high frequencies, in the transparent range, the shape of the spectra of inhomogeneous sources does not depend on the character of the non-uniformity of the magnetic-field and particle-density distributions. This result can be readily understood from the following considerations. Let us divide the emitting region into very small volumes, such that both the field and particle distributions inside each can be considered uniform. Then, according to Eq. (12), the luminosity of each elementary volume is

$$P_i = \varepsilon_i \Delta V_i = a_i \nu^{-\alpha},$$

where $a_i = c_5(\gamma) N_i H_i^{(\gamma+1)/2} (2C_1)^{(\gamma-1)/2} \Delta V_i$. Since the source is transparent, its luminosity is the sum of the luminosities of all the partial volumes:

$$P = \sum p_i = \nu^{-\alpha} \sum a_i.$$

Thus, the inhomogeneity of the radio source should not affect the shape of its spectrum at frequencies where the source is transparent.

A comparison of our calculated spectra to the approximate analytical solutions from [8, 9] shows that there exist models for which the analytical approximations are rather close to the exact (calculated) spectra, for which the approximate and calculated spectra are not so close, and for which the approximate solutions do not reflect the real situation at all. For example, the models with $n = 0$, $m = 2$, and γ from two to three possess flat regions in their spectra, where $\alpha_{LF} = 0$. However, according to [8, 9], the spectral index near the low-frequency cut-off is

$$\alpha_{LF} = \frac{13 - 5n - 3m - 2m\gamma + 2\gamma}{2 - 2n - 2m - m\gamma}. \quad (17)$$
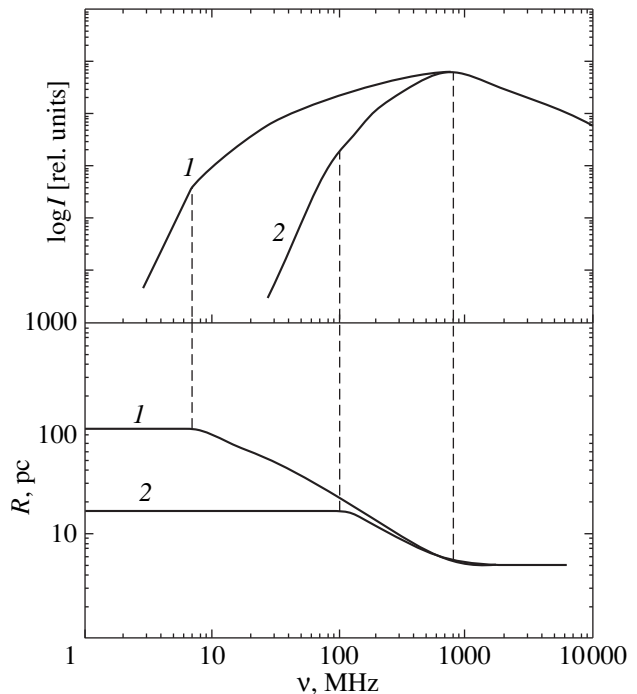
Fig. 5. Frequency dependence of the apparent source size for two models: (*1*) $m = 2$, $n = 0$, $k_H = 10^{3/2}$ and (*2*) $m = 2$, $n = 0$, $k_H = 10^{1/2}$. The spectra for these two models are also given.
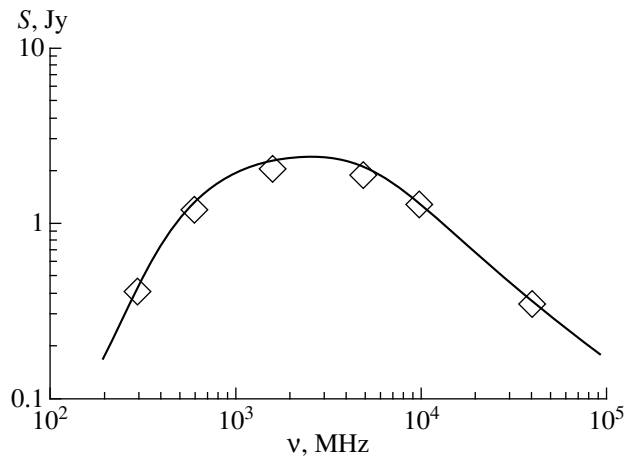
Fig. 6. Spectrum of the radio source IAU 0500 + 019. Diamonds: observational data; solid curve: the calculated spectrum.

For these n and m values, this equation gives $\alpha_{LF} = -0.5$ for $\gamma = 2$ and $\alpha_{LF} = -0.12$ for $\gamma = 3$. While the latter value of α_{LF} can be considered close to zero, the former cannot be. On the other hand, according to Eq. (17), $\alpha_{LF} = 0$ for $n = 2$, $m = 1$, and $\gamma = 2.5$. Our calculation of the exact

spectrum for the model with these parameters yielded $\alpha_{LF} = 0.16$.

Note that such discrepancies between spectral indices can be detected in observations. If the spectral maximum is at 1 GHz and observations are carried out at 0.1 GHz, then, with flux-density errors of 1% at 1 GHz and ~20% at 0.1 GHz, the error of the estimated spectral index between these frequencies will be $\Delta\alpha \cong 0.03$. Hence, the discrepancies between the exact and approximate spectral indices indicated above can be detected observationally. We conclude that a correct interpretation of radio source spectra must be based on exact solutions of the transfer equation.

In models in which the magnetic field is uniform and only the relativistic particle density is varied, the spectra are almost indistinguishable from those for homogeneous sources (second column of Figs. 1, 3). The discrepancies become appreciable only when $m > 3$. In these models, the low-frequency cut-off of the power-law spectrum with $\alpha_{LF} < 2.5$ is completely absent. In this case, the concept of the spectral index (12) simply becomes meaningless. This additionally strengthens our conclusion that accurate spectra must be interpreted using the exact solutions of the transfer equation.

Our numerical simulations indicate that the role of the relativistic particles is not entirely independent. If the magnetic field is varied and the particle distribution remains uniform, the spectra clearly differ from that of a homogeneous source. If both the field and particle density are varied, the spectra also differ appreciably from the homogeneous case. Finally, if only the particle density is varied, the spectra are virtually indistinguishable from that of a homogeneous source.

The resulting spectra (Figs. 1, 3) can also be used as a catalog of theoretical spectra for use in the interpretation of observations of real sources. As an illustration, Figure 6 shows the spectrum of the compact radio source IAU 0500 + 019 ($z = 0.5$) [18]. The spectral maximum is fairly broad; hence, homogeneous source models are completely unsuitable for descriptions of this spectrum. The solid curve shows the spectrum we have calculated for an inhomogeneous source with $n = 0$, $m = 2$, $k_H = 10^2$, $H(0) = 5$ G, and $N_0 = 7 \times 10^{-13}$ (CGSE). We can see that the theoretical inhomogeneous-source spectrum fits the experimental points very well.

7. CONCLUSION

Nonuniformity in the distributions of the magnetic field and relativistic particle density in a source of synchrotron radiation affects only the shape of the low-frequency cut-off of its spectrum at frequencies where the source is partially transparent. The source brightness distribution changes at these same frequencies. In some models, this part of the spectrum has a power-law character with spectral index $\alpha_{LF} < 2.5$, if the magnetic-field intensity and particle density decrease with distance from the source center.

The shape of the low-frequency cut-off depends on all the parameters defining the inhomogeneous source: γ, n, m, k_H, and k_N. As k increases, the extent of this part of the spectrum also increases, but α_{LF} remains unchanged. The spectra for homogeneous models are steeper than those of three-dimensional structures: in one-dimensional models, $\alpha_{LF} > 1.2$, while, in spherical models, $\alpha_{LF} < 1.4$. When only the particle density is varied, and $H = $ const, the spectra of inhomogeneous sources are virtually indistinguishable from those of homogeneous sources. Differences appear only for large values of k_N ($k_N > 10^4$). Spherical sources in which the magnetic field and energetic particles density increase with distance from the center have spectral indices larger than the canonical optically thick value, $\alpha_{LF} > 2.5$, but only slightly (the maximum value of α_{LF} is 2.65).

The accuracy of approximate analytical expressions for the spectra of inhomogeneous sources is insufficient for the interpretation of the spectra of compact sources obtained with VLBI. For this reason, the interpretation of such observations of compact radio sources must be based on exact solutions.

Since information about the physical conditions in active galactic nuclei is contained in the low-frequency cut-offs of their radio spectra and in the variation of their angular sizes at frequencies near the cut-off, low-frequency observations of compact radio sources with high resolution and high sensitivity are of primary importance in studies of the physics of galactic nuclei. At present, such observations are restricted to the decimeter band, whereas most radio sources have cut-offs at longer wavelengths. For this reason, it is desirable to create VLBI systems operating at meter wavelengths.

REFERENCES

1. V. L. Ginzburg, V. N. Sazonov, and S. I. Syrovatskiĭ, Usp. Fiz. Nauk **94**, 63 (1968) [Sov. Phys. Usp. **11**, 34 (1968)].

2. A. Pacholczyk, *Radio Astrophysics. Nonthermal Processes in Galactic and Extragalactic Sources* (Freeman, San Francisco, 1970; Mir, Moscow, 1973).

3. V. S. Artyukh, Tr. Fiz. Inst. Akad. Nauk SSSR **189**, 223 (1988).

4. V. A. Razin, Izv. Vyssh. Uchebn. Zaved., Radiofiz. **3**, 921 (1960).

5. V. I. Slysh, Dissertation, 1965.

6. S. Ya. Braude, Astron. Zh. **44**, 309 (1967) [Sov. Astron. **11**, 244 (1967)].

7. J. J. Condon and L. L. Dressel, Astrophys. J., Lett. Ed. **15**, L 203 (1973).

8. A. G. De Bruyn, Astron. Astrophys. **52**, 439 (1976).

9. A. P. Marscher, Astrophys. J. **216**, 244 (1977).

10. É. R. Mustel', *Stellar Atmospheres* (Izd. Fiz.-Mat. Lite-ratury, Moscow, 1960).

11. R. J. Gould, Astron. Astrophys. **76**, 306 (1979).

12. F. Hoyle and G. R. Burbidge, Astrophys. J. **144**, 534 (1966).

13. T. W. Jones and P. E. Hardee, Astrophys. J. **228**, 268 (1979).

14. D. B. Cook and S. R. Spangler, Astrophys. J. **240**, 751 (1980).

15. V. S. Beskin, Usp. Fiz. Nauk **167**, 689 (1997) [Phys. Usp. **40**, 659 (1997)].

16. L. M. Ozernoy and V. N. Sazonov, Astrophys. J., Lett. Ed. **8**, L 231 (1971).

17. S. Chandrasekhar, Mon. Not. R. Astron. Soc. **112**, 475 (1952).

18. C. Stanghellini, C. P. O'Dea, D. Dallacasa, *et al.*, Astron. Astrophys., Suppl. Ser. **131**, 303 (1998).

Translated by G. Rudnitskiĭ

The Detection of New Methanol Masers in the 5_{-1}–4_0E Line

S. V. Kalenskiĭ[1], V. I. Slysh[1], I. E. Val'tts[1], A. Winnberg[2], and L. E. Johansson[2]

[1]*Astro Space Center, Profsoyuznaya ul. 84/32, Moscow, 117810 Russia*
[2]*Onsala Space Observatory, S-439 Onsala 92, Sweden*
Received February 3, 2000

Abstract—Forty-eight objects were detected in the 5_{-1}–4_0E methanol line at 84.5 GHz during a survey of Class I maser sources. Narrow maser features were found in 14 of these. Broad quasi-thermal lines were detected toward other sources. One of the objects with narrow features at 84.5 GHz, the young bipolar outflow L1157, was also observed in the 8_0–7_1A^+ line at 95.2 GHz; a narrow line was detected at this frequency. Analysis showed that the broad lines are usually inverted. The quasi-thermal profiles imply that there are no more than a few line opacities. These results confirm the plausibility of models in which compact Class I masers appear in extended sources as a result of a preferential velocity field. © *2001 MAIK "Nauka/Interperiodica".*

1. INTRODUCTION

The methanol molecule (CH_3OH) is a slightly asymmetric rotor with hindered internal rotation, and has a large number of allowed transitions at radio frequencies. Many observations in various methanol lines have been carried out, leading to the detection of bright and narrow maser lines in a number of star-forming regions. A scheme for classifying methanol masers was first proposed by Batrla *et al.* [1] and modified by Menten [2]. According to Menten [2], all methanol masers can be divided into two classes, I and II. The Class I masers emit in the 7_0–6_1A^+, 4_{-1}–3_0E, 8_0–7_1A^+ etc. transitions, while the Class II masers emit in the 5_1–6_0A^+, 2_0–$3_{-1}E$, J_0–$J_{-1}E$ etc., transitions. The Class I masers are pumped by collisions, in the absence of strong radiation, whereas the Class II masers are pumped by strong external radiation [3–5]. The strongest and most widespread Class I masers emit in the 7_0–6_1A^+ and 4_{-1}–3_0E transitions at 7 and 8 mm, respectively. Weaker masers have been found in the 8_{-1}–7_0E, 6_{-1}–5_0E, and 8_0–7_1A^+, etc., transitions at 1, 2, and 3 mm, respectively as well as in the J_2–J_1E transitions at 13 mm. Several surveys in the J_2–J_1E, 7_0–6_1A^+, 8_0–7_1A^+, 4_{-1}–3_0E, and 6_{-1}–5_0E Class I transitions have been carried out [6–9], leading to the detection of more than one hundred maser sources in regions of massive star formation.

Masers in the 5_{-1}–4_0E line at 84.5 GHz were found by Batrla and Menten [12] and Menten [2] toward NGC 2264, OMC-2, and DR 21, but no extended survey in this line had been done. The 5_{-1}–4_0E transition belongs to Class I. Its excitation is similar to that of the 4_{-1}–3_0E and 6_{-1}–5_0E transitions (Fig. 1). Since methanol masers emit in several lines of the same class, we expect the detection of a fairly large number of maser sources at 84.5 GHz. Their parameters should be taken into account when modeling maser sources. Therefore, we made a survey of known Class I maser sources at 84.5 GHz. In addition, we observed the source L1157, in which the abundance of methanol and certain other molecules is enhanced towards the blue wing of a young bipolar outflow [13].

2. OBSERVATIONS

The first series of observations was carried out in May 1997 using the 20-m millimeter-wave telescope of the Onsala Space Observatory. The line rest frequency of 84 521.21 MHz was taken from the electronic database of Lovas (http://physics.nist.gov/cgi-bin/micro/table5/start.pl). Pointing errors were checked using observations of SiO masers and found to be within 5″. The main beam efficiency and the half-power beamwidth at 84.5 GHz were 0.6″ and 44″, respectively. The observations were performed in a dual-beam switching mode with a switching frequency of 2 Hz and a beam throw of 11′. A cryogenically cooled low-noise SIS mixer was used. The single sideband receiver noise temperature was about 150 K. The system noise temperature corrected for atmospheric absorption, rearward spillover and dome losses varied between about 700 and 1500 K, since the weather during the observations was fairly bad. The data were calibrated using a chopper-wheel method. The back end consisted of a 256-channel filter spectrometer with 250 kHz frequency resolution (0.887 km/s at 84.5 GHz). The relatively low spectral resolution explains why the flux densities of the maser features in NGC 2264, DR 21(OH), and DR 21 West (Table 1) were lower than the values previously reported in [12] and [2].

Since the spectral resolution in the first series of observations turned out to be insufficient, we reobserved some of the sources with the same telescope in March 2000. The back end of the receiver was an autocorrelator with 50 kHz (0.177 km/s) frequency resolution, connected in parallel with the filter spectrometer

used in the first set of observations. During the second series, we also observed the L1157 region in the 8_0–$7_{-1}A^+$ line at 95 169.440 MHz.

3. RESULTS

Emission was detected in 48 of the 51 sources observed, and was not detected in W 51 Main, 19 446 + 2505, and R 146. These results are presented in Tables 1 and 2, and the spectra of newly detected sources are shown in Figs. 2 and 3. The spectra are markedly different from those of the strongest Class I transition, 7_0–6_1A^+ at 44.1 GHz. At 44.1 GHz, most of the sources from our sample have bright and narrow maser features, whereas broad quasi-thermal components dominate at 84.5 GHz, and narrow (<1.5 km/s) features are present in the spectra of only 14 of the 48 detected sources. However, it is possible that at least some of the quasi-thermal lines contain narrow maser components, especially in the spectra of sources observed only with low (0.887 km/s) resolution.

The shape of the 84.5 GHz spectra closely resemble the shape of the spectra of the same sources in the 8_0–7_1A^+ [8] and 6_{-1}–5_0E [14] transitions at 95.2 and 132.8 GHz, respectively. Figure 4 shows the relationships between the integrated intensities of thermal lines at 84.5, 95.2, and 132.8 GHz, which can be fitted by the equations

$$\int T_{mb}dV(95.2) = 0.4\int T_{mb}dV(84.5) + 0.17 \quad (1)$$

and

$$\int T_{mb}dV(132.8) = 0.7\int T_{mb}dV(84.5) + 0.0, \quad (2)$$

where T_{mb} is the main-beam brightness temperature. The relative decrease of the line intensities at 132.8, and especially at 95.2 GHz, is probably connected with the decrease of the level populations with increase of their energies: at a gas temperature of 35 K, the population of the 8_0A^+ level is about 40% of the population of the $5_{-1}E$ level, making it possible to explain the relationships obtained.

In some sources, narrow maser features were detected at 84.5 GHz, whereas only quasi-thermal components were found at 132.8 and 95.2 GHz. The absence of maser lines at 95.2 GHz could be due to the insufficient spectral resolution (0.79 km/s) of the survey of [8], but the observations at 132.8 GHz [14] had high spectral resolution (0.11 km/s), so that not detecting narrow components at 132.8 GHz cannot be explained in this way. Apparently, in this case, we are dealing with the general tendency for maser weakening with increase in frequency, considered in detail in [15].

Note the detection of narrow features at 84.5 and 95.2 GHz toward the B2 region in the blue wing of the bipolar outflow L1157. This region is shock heated to about 100 K at the boundary between the flow and the surrounding gas, and the abundances of methanol, ammonia,
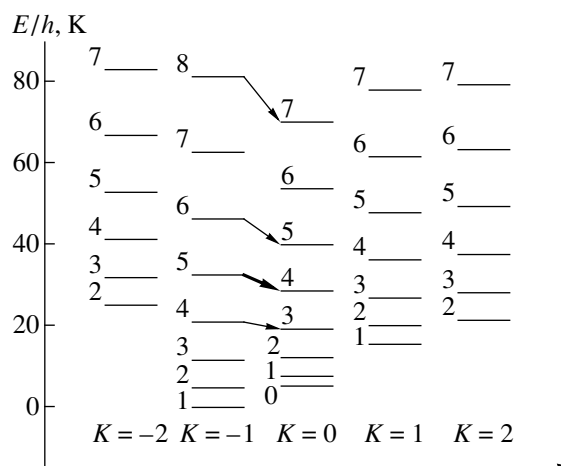
Fig. 1. Energy levels of E methanol. The thick arrow shows the observed 5_{-1}–4_0E transition. The thin arrows show other Class I transitions that operate via the same excitation mechanism.

formaldehyde, and certain other molecules are enhanced relative to those in cold gas [13]. At 84.5 GHz, we can clearly see narrow components at 0.73 and 2.05 km/s, and at 95.2 GHz, a narrow feature at 0.85 km/s. The velocity range of this last feature overlaps with that of the 0.73 km/s component of the 5_{-1}–4_0E line, and probably appears in the same region. Toward the central source (L1157-mm), where the methanol column density is two orders of magnitude lower [13], no narrow lines were detected. Unlike other methanol masers, which are associated with high-luminosity (above $10^3 L_\odot$) young stellar objects, this bipolar outflow is driven by an object with low luminosity ($11 L_\odot$). It is interesting to determine via interferometric measurements whether these lines arise, as usual, in bright and compact maser sources or whether they are associated with more extended objects.

4. EXCITATION TEMPERATURE OF THE QUASI-THERMAL LINES

Slysh *et al.* [14] showed that even quasi-thermal 6_{-1}–5_0E lines are typically inverted, and their quasi-thermal appearance indicates that the line opacities are not large enough to cause significant narrowing. Since the excitation of the 5_{-1}–4_0E transition is similar to that of the 6_{-1}–5_0E transition, it is possible that the quasi-thermal 5_{-1}–4_0E lines are also inverted. To test this hypothesis, we determined the excitation temperature of the 5_{-1}–4_0E lines using the intensities of the 4_0–$4_{-1}E$ lines at 157.2 GHz measured in [14]. The excitation temperatures were derived analytically and using statistical equilibrium calculations. The features with derived excitation temperatures are marked with asterisks in Table 1.

The excitation temperature of the 5_{-1}–4_0E transition was derived analytically as follows. If the 5_{-1}–4_0E line is optically thin and the background radiation is negli-

KALENSKIĬ *et al.*
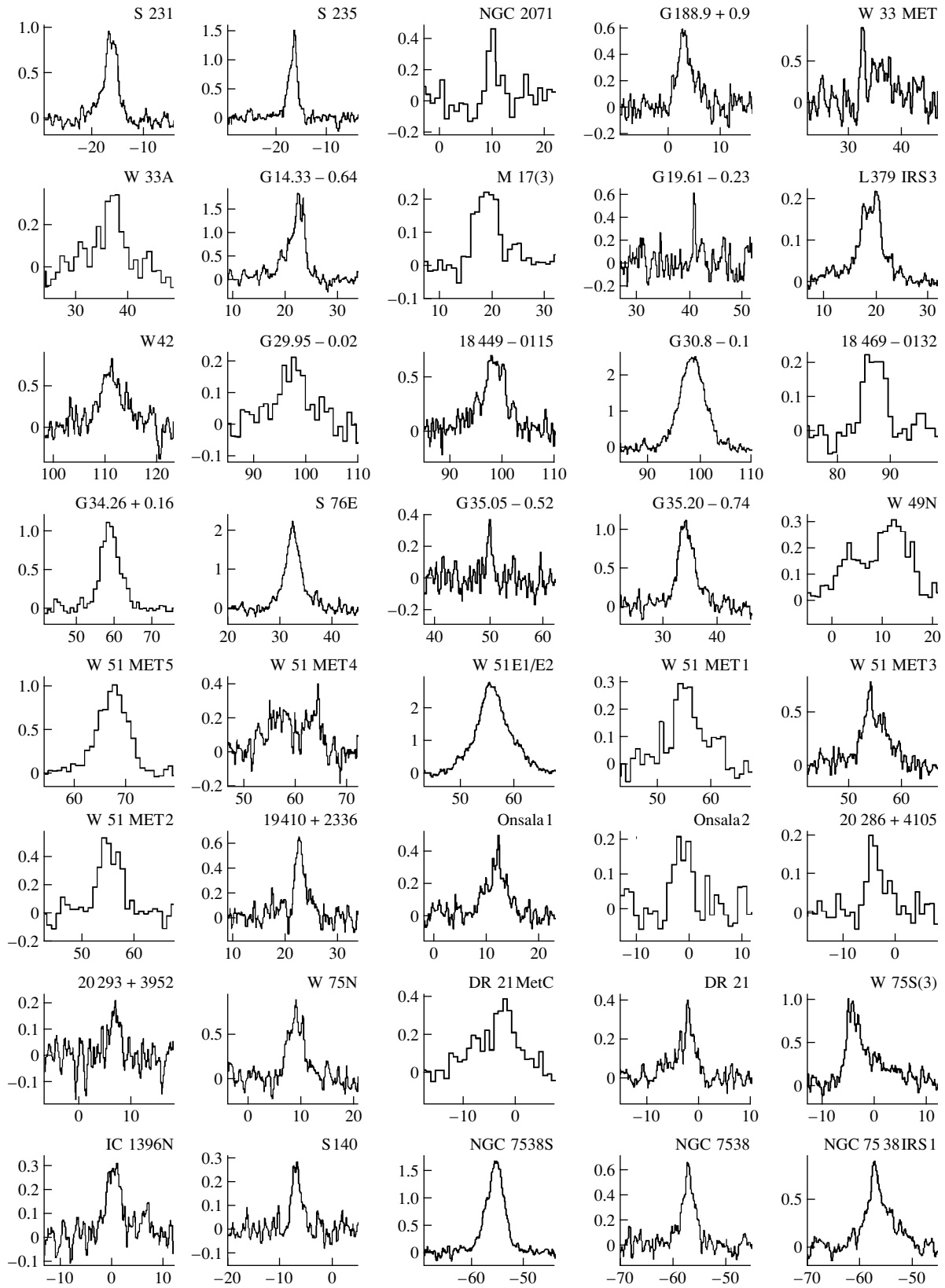
Fig. 2. Spectra of the newly detected sources. The horizontal axis plots V_{LSR} in km/s, and the vertical axis plots the antenna temperature T_A^* in K. The frequency resolution of the spectra is presented in Table 1.

Table 1. Parameters of the observed lines

Source	R.A.(J2000) Dec.(J2000)	$\int T_A^* dV$, K (km/s)	V_{LSR}, km/s	ΔV, km/s	T_A^*, K	Δv, kHz
S 231	05^{h}39^{m}12$\overset{s}{.}$9	1.82(0.12)*	−16.77(0.13)	4.72(0.27)	0.36	50
	35°45′54″	0.56(0.11)	−16.51(0.06)	0.97(0.14)	0.55	
		0.74(0.12)	−15.28(0.07)	1.23(0.16)	0.57	
S 235	05 40 53.3	2.10(0.09)*	−16.80(0.04)	2.21(0.07)	0.90	50
	35 41 49	0.48(0.07)	−16.28(0.02)	0.66(0.06)	0.68	
NGC 2071	05 47 04.1	1.30(0.22)	10.00(0.21)	2.69(0.65)	0.46	250
	00 21 42					
G188.9+0.9	06 08 54.2	1.81 (0.08)*	3.08(0.07)	3.45(0.19)	0.49	50
	21 38 37					
S 255	06 12 56.4	0.98(0.25)	−13.31(0.66)	5.24(1.62)	0.18	250
	17 59 54					
NGC 2264	06 41 09.7	1.88(1.64)	7.29(0.18)	1.25(0.50)	1.41	250
	09 29 35	2.31(1.65)*	8.70(1.07)	2.83(1.20)	0.76	
W 33 MET	18 14 11.0	0.77(0.10)	32.71(0.05)	0.81(0.10)	0.89	50
	−17 55 57	1.94(0.22)*	36.27(0.25)	4.28(0.61)	0.43	
W 33A	18 14 39.8	1.45(0.21)	37.06(0.29)	4.06(0.78)	0.34	250
	−17 51 58					
G14.33−0.64	18 18 54.6	4.41(0.21)	21.41(0.13)	5.08(0.26)	0.82	50
	−16 47 50	1.26(0.18)	22.55(0.04)	1.08(0.15)	1.10	
		0.68(0.09)	23.56(0.03)	0.56(0.06)	1.14	
M 17(3)	18 20 24.1	1.20(0.11)*	18.93(0.22)	4.88(0.49)	0.23	250
	−16 11 27					
G19.61−0.23	18 27 38.1	0.30(0.04)	40.92(0.03)	0.45(0.08)	0.64	50
	−11 56 40					
L379 IRS3	18 29 24.7	6.52(0.10)	18.73(0.18)	9.72(0.18)	0.63	50
	−15 15 29	2.49(0.10)	18.22(0.18)	2.04(0.18)	1.15	
		2.49(0.10)	20.35(0.18)	1.51(0.18)	1.55	
W 42	18 36 12.4	4.23(0.21)	111.11(0.15)	6.44(0.44)	0.62	50
	−07 12 10					
G29.95−0.02	18 46 04.0	1.20(0.14)*	97.43(0.30)	6.21(0.99)	0.18	250
	−02 39 21					
18 449−0115	18 47 34.6	0.49(0.16)	93.77(0.54)	3.79(1.08)	0.12	50
	−01 12 46	3.11(0.17)	98.57(0.12)	4.54(0.27)	0.64	
G30.8−0.1	18 47 46.9	14.5(0.13)	98.44(0.02)	5.44(0.06)	2.51	50
	−01 54 35					
18 469−0132	18 49 32.9	1.06(0.09)	86.82(0.19)	4.24(0.36)	0.24	250
	−01 28 54					
G34.26+0.15	18 53 18.5	6.94(0.21)*	58.72(0.09)	5.99(0.22)	1.09	250
	01 14 58					
S 76E	18 56 10.4	4.30(0.44)	32.73(0.15)	6.46(0.48)	0.63	50
	07 53 14	3.70(0.43)	32.41(0.03)	2.42(0.14)	1.44	
G35.05−0.52	18 57 09.0	0.34(0.05)	49.92(0.06)	0.96(0.16)	0.33	50
	01 39 03					
G35.20−0.74	18 58 12.7	4.05(0.10)	34.27(0.04)	3.64(0.11)	1.04	50
	01 40 36					
W 49N	19 10 13.4	1.04(0.15)	3.31(0.34)	5.68(0.95)	0.17	250
	09 06 14	2.36(0.16)	12.15(0.22)	7.25(0.57)	0.31	
W 51 MET5	19 23 38.2	1.23(0.18)	63.09(0.39)	4.61(0.77)	0.25	250
	14 30 05					
W 51 MET4	19 23 43.2	1.47(0.11)	56.82(0.21)	6.27(0.56)	0.22	50
	14 31 34	0.72(0.08)	63.25(0.18)	3.23(0.33)	0.21	
		0.10(0.03)	64.18(0.04)	0.38(0.09)	0.25	
W 51E1/E2	19 23 43.8	4.69(0.46)	55.50(0.05)	3.64(0.17)	1.21	250
	14 30 36	15.8(0.47)*	56.38(0.08)	9.61(0.22)	1.54	
W 51 MET1	19 23 43.9	1.72(0.14)	55.22(0.21)	6.15(0.74)	0.26	250
	14 29 25					
W 51 MET3	19 23 45.1	0.40(0.08)	53.91(0.07)	1.07(0.19)	0.35	50
	14 29 45	2.52(0.12)*	55.17(0.15)	5.83(0.26)	0.41	

Table 1. (Contd.)

Source	R.A.(J2000) Dec.(J2000)	$\int T_A^* dV$, K (km/s)	V_{LSR}, km/s	ΔV, km/s	T_A^*, K	$\Delta\nu$, kHz
W 51 MET2	19 23 46.5	2.75(0.20)*	55.07(0.17)	4.91(0.40)	0.53	250
	14 29 41					
W 51 Main	19 23 53.9				<0.08	250
	14 30 37					
19 410 + 2336	19 43 11.5	1.37(0.07)*	22.78(0.06)	2.13(0.15)	0.61	50
	23 44 06					
S 87	19 46 20.5	0.62(0.15)	22.65(0.68)	5.26(1.11)	0.11	250
	24 35 34					
19 446 + 2505	19 46 47.2				<0.08	250
	25 12 43					
Onsala 1	20 10 09.1	1.39(0.06)*	11.67(0.11)	4.83(0.26)	0.27	50
	31 31 37	0.11(0.02)	12.10(0.04)	0.44(0.09)	0.23	
20 126 + 4104	20 14 25.9	0.46(0.12)	−2.36(0.89)	5.30(1.99)	0.08	250
	41 13 32					
Onsala 2	20 21 42.1	0.77(0.10)	−1.32(0.25)	3.55(0.48)	0.21	250
	37 26 08					
20 286 + 4105	20 28 40.6	0.75(0.07)	−3.72(0.15)	3.23(0.34)	0.22	250
	41 05 38					
20 293 + 3952	20 31 10.6	0.42(0.05)	6.60(0.12)	2.17(0.31)	0.18	50
	40 03 09					
W 75 N	20 38 36.8	0.76(0.19)	7.38(0.17)	1.41(0.29)	0.51	50
	42 37 60	1.13(0.24)	8.93(0.07)	1.27(0.26)	0.84	
		0.51(0.14)	10.21(0.05)	0.72(0.14)	0.66	
		0.36(0.12)	11.70(0.33)	1.95(0.70)	0.17	
DR 21 West	20 38 54.6	1.78(0.17)	−2.41(0.05)	0.98(0.08)	1.70	250
	42 19 23	1.59(0.23)*	−2.73(0.37)	5.87(1.07)	0.25	
DR 21 MetC	20 38 59.6	2.51(0.38)	−3.96(0.83)	12.00(1.84)	0.20	250
	42 19 24	0.64(0.26)*	−2.01(0.34)	2.81(0.81)	0.21	
DR 21	20 38 59.9	0.32(0.06)	−5.87(0.39)	3.59(0.72)	0.09	50
	42 19 28	0.07(0.02)	−3.75(0.06)	0.47(0.11)	0.15	
		0.78(0.05)	−2.05(0.06)	2.35(0.17)	0.31	
DR 21(OH)	20 39 00.7	2.17(0.27)	−4.54(1.13)	19.42(2.98)	0.11	250
	42 22 51	4.15(0.17)*	−3.75(0.07)	3.74(0.13)	1.04	
		1.75(0.29)	−1.25(0.23)	1.98(0.25)	0.83	
		1.81(0.35)	0.22(0.06)	1.18(0.09)	1.44	
W 75 S(3)	20 39 03.4	1.01(0.04)	−4.90(0.18)	1.51(0.18)	0.63	50
	42 25 53	0.69(0.04)	−3.49(0.18)	1.65(0.18)	0.39	
		0.83(0.04)	−2.55(0.18)	3.92(0.18)	0.20	
		2.60(0.04)	0.80(0.18)	11.31(0.18)	0.22	
IC 1396N	21 40 42.3	1.20(0.06)	0.29(0.08)	3.55(0.23)	0.32	50
	58 16 10	0.50(0.07)	6.38(0.25)	4.20(0.87)	0.11	
21 413 + 5442	21 43 01.2	0.38(0.08)	−75.11(0.80)	5.57(1.54)	0.06	250
	54 56 15	0.36(0.07)	−60.59(0.44)	3.57(1.02)	0.09	
R 146	21 43 49.5				<0.23	250
	66 06 46					
S 140	22 19 18.3	0.58(0.03)*	−6.94(0.06)	2.03(0.13)	0.27	50
	63 18 49					
NGC 7538S	23 13 44.8	6.70(0.07)	−55.54(0.02)	3.95(0.05)	1.59	50
	61 26 51					
NGC 7538	23 13 45.4	1.63(0.06)*	−57.19(0.05)	2.71(0.12)	0.56	50
	61 28 10					
NGC 7538	23 13 46.4	0.80(0.10)	−57.20(0.04)	1.59(0.17)	0.470	50
IRS1	61 27 33	3.14(0.12)	−56.08(0.13)	6.91(0.25)	0.43	

Notes: An asterisk means that the line excitation temperature has been determined (see Section 4). The upper limits on the antenna temperature
for W 51 Main, 19 446 + 2505, and R 146 are given at the 3σ level. The frequency resolution of the spectra is given in the last column.
[1] A fit by a single Gaussian is possible for W 75 N.
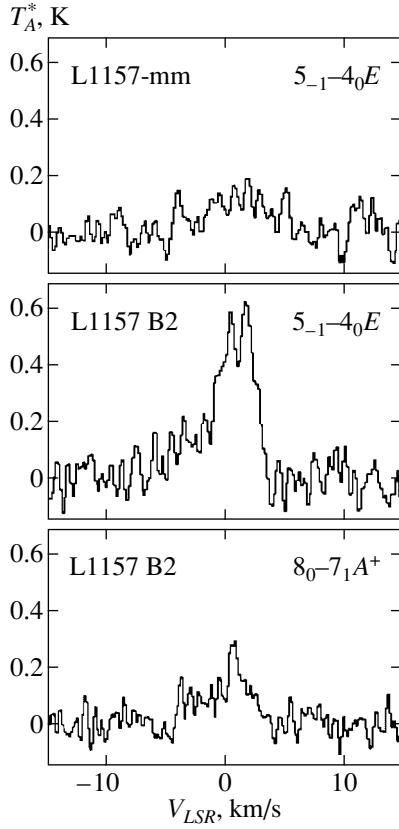
Fig. 3. Spectra of L1157 at 84.5 and 95.2 GHz. The observations had a frequency resolution of 50 kHz.

gible, the column density of methanol in the $5_{-1}E$ level (N_5) can be found from the formula

$$\frac{N_5}{g_5} = \frac{3k \int T_{\mathrm{br}} dV}{8\pi^3 \mu^2 \nu S},\qquad(3)$$

where g_5 is the rotational statistical weight of the $5_{-1}E$ level, k is Boltzmann's constant, T_{br} is the line bright-

ness temperature, μ is the permanent dipole moment, ν is the frequency, and S is the line strength.

Similarly, from the intensity of the $4_0-4_{-1}E$ line, observed in a number of sources in [14] with approximately the same spatial resolution, we can find the column density of methanol in the 4_0E level (N_4). The excitation temperature of the $5_{-1}-4_0E$ transition can then be found from

$$T_{\mathrm{ex}} = -\frac{h\nu}{k\ln\left(\dfrac{N_5 g_4}{N_4 g_5}\right)},\qquad(4)$$

where g_4 is the rotational statistical weight of the $4_{-1}E$ level. We applied this method to 20 quasi-thermal sources from our sample and, for each, obtained negative excitation temperatures between $1 \approx -1.5$ K and ≈ -4.5 K; i.e., the at 84.5 GHz quasi-thermal lines proved to be strongly inverted. The excitation temperatures derived in this way are distorted by a number of factors, such as the line opacities, influence of the microwave background, etc. [14]. Therefore, we verified the results using a grid of LVG methanol models spanning the ranges 10^4-10^8 cm^{-3} in density, 10–100 K in temperature, and $7 \times 10^{-7}-2 \times 10^{-3}$ cm^{-3}/(km/s pc^{-1}) in methanol density divided by the velocity gradient. For each source, we selected models corresponding to the observed ratio of the 84.5 and 157.2 GHz main-beam brightness temperatures. We assumed that the error of these brightness temperature ratios, stipulated mainly by possible calibration differences between the 84.5 and 157.2 GHz measurements, is no larger than 30%, and accordingly selected models that reproduced the observed ratios with accuracies no worse than 30%. We used one more condition to select the models: that the ratio of the model brightnesses of the $4_0-4_{-1}E$ and $5_0-5_{-1}E$ lines correspond to the observed ratio with an accuracy no worse than 10%. The $4_0-4_{-1}E$ and $5_0-5_{-1}E$ lines are closely spaced in frequency, and were observed simultaneously in [14]. Therefore, the ratio of their intensi-
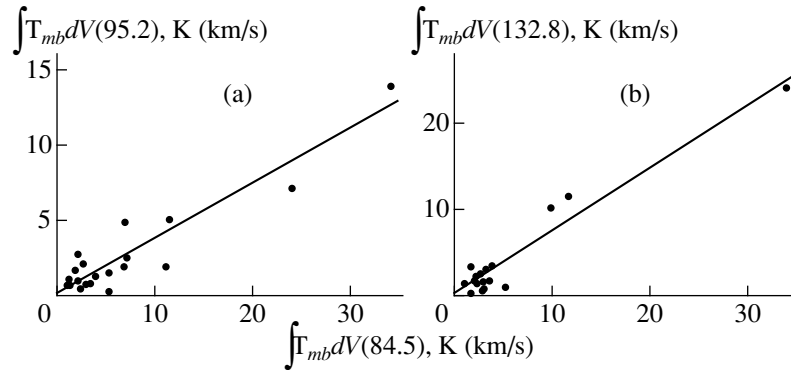
Fig. 4. Relationships between the main-beam brightness temperatures integrated over the line profiles: (a) the $5_{-1}-4_0E$ line at 84.5 GHz versus the $8_1-7_0A^+$ line at 95.2 GHz; (b) the $5_{-1}-4_0E$ line at 84.5 GHz versus the $6_{-1}-5_0E$ line at 132.8 GHz. All three lines were observed with essentially the same full-width at half-power (FWHP) for the main beam: 84.5 GHz, 44″ (this paper); 95 GHz, 39″ [8]; 132 GHz, 41″ [11].

Table 2. Parameters of lines towards L1157

Transition	R.A.(J2000) Dec.(J2000)	$\int T_A^* dV$, K (km/s)	V_{LSR}, km/s	ΔV, km/s	T_A^*, K
$5_{-1}-4_0E$	$20^h39^m06\overset{s}{.}2$	0.86 (0.08)	1.28 (0.29)	6.29 (0.63)	0.13
(L1157-mm)	68°02′16″				
$5_{-1}-4_0E$	20 39 08.6	0.87 (0.08)	−2.34 (0.31)	5.53 (0.52)	0.150
(L1157 B2)	68 00 46	0.40 (0.12)	−0.14 (0.18)	1.25 (0.33)	0.30
		0.24 (0.11)	0.73 (0.06)	0.64 (0.15)	0.35[1]
		1.01 (0.07)	2.05 (0.05)	1.65 (0.12)	0.57
$8_0-7_{-1}A^+$	20 39 08.6	0.68 (0.08)	0.04 (0.29)	5.45 (0.51)	0.12
(L1157 B2)	68 00 46	0.15 (0.04)	0.85 (0.07)	0.75 (0.20)	0.19

Notes: The spectra had frequency resolution 50 kHz.
[1] A doubtful feature.

ties is free from pointing and calibration errors, and was thus measured very accurately. The results are as follows.

For each of the 20 sources, we found a number of models with temperatures of 10–70 K, which corresponded to the observed ratios. For the three sources 19410 + 2336, S 235, and S 140, only negative excitation temperatures were found for the $5_{-1}-4_0E$ transition. For 12 sources from our list, we found models both with inversion of the $5_{-1}-4_0E$ transition and with positive excitation temperatures for this transition, with gas kinetic temperatures 10–15 K and large optical depths in the $5_{-1}-4_0E$ line, $4_0-4_{-1}E$ line, or both of these lines. Such low gas temperatures are not typical for these sources; in addition, the methanol abundances in the models with positive excitation temperatures were of the order of 10^{-7} or higher for most of the sources. Such high abundances are characteristic only of hot (≥ 100 K) gas and are at least two orders of magnitude larger than the abundances observed for cold (≈ 10 K) or warm (20–50 K) gas [16, 17]. Therefore, we believe that the models without inversion at 84.5 GHz are not applicable to the real sources, and that the quasi-thermal lines are typically inverted.

In G29.95 − 0.02, G34.26 + 0.15, NGC 7538, W 49, and W 51E1/E2, the observed intensity ratios can be obtained both in models with inversion and in realistic models with positive excitation temperatures at 84.5 GHz and gas temperatures between 10 and 25–45 K, depending on the source. The densities in the models without inversion are 10^7–10^8 cm^{-3}, i.e., much higher than those in the models with inversion, and the methanol abundances are lower than 10^{-8}. However, since a number of models with inversion (i.e., the same as those for the other 15 sources) are applicable to these objects as well, it is not clear whether they are somehow different from the others (i.e., whether these sources are the densest in our sample) or not.

Thus, the quasi-thermal $5_{-1}-4_0E$ methanol lines are typically inverted. A similar conclusion was drawn for another Class I line, $6_{-1}-5_0E$, in [14].

Models of cosmic maser sources can be divided into two groups. The first group includes models in which the source sizes coincide with the sizes of the observed maser spots; i.e., they are smaller than one arcsecond. The second group includes models in which the compact maser spots appear in extended inverted sources owing to some preferential kinematics, geometry, or both. In a random velocity field—in a turbulent medium, for example—the coherence lengths along some directions are usually larger than the mean coherence length, leading to strong maser emission along these directions, provided that the corresponding transitions are inverted. The effect of the source velocity distribution on J_2-J_1E methanol emission was considered by Sobolev *et al.* [18], who showed that emission arising in a turbulent medium can appear in the form of isolated clumps. Our results, while not implying that models of the first group are no longer valid, show the applicability of models of the second group to 84.5 GHz masers, since the quasi-thermal $5_{-1}-4_0E$ lines, which arise in extended sources, appeared to be inverted.

5. CONCLUSION

We have detected 48 objects in the $5_{-1}-4_0E$ methanol line during a survey of Class I maser sources. Narrow maser lines were detected in 14 of these. Quasi-thermal emission was detected toward other sources. We also observed one of the 14 objects with maser features at 84.5 GHz, L1157, in the $8_0-7_1A^+$ line at 95.2 GHz, and a narrow feature was detected at this frequency.

Our analysis showed that the quasi-thermal $5_{-1}-4_0E$ lines in these sources are usually inverted. The quasi-thermal profiles show that the line opacities are no larger than a few. These results confirm the applicability of models in which compact maser spots appear in extended inverted sources as a result of preferential source kinematics or geometry.

ACKNOWLEDGMENTS

REFERENCES

1. W. Batrla, H. E. Matthews, K. M. Menten, and C. M. Walmsley, Nature **326**, 49 (1987).

2. K. M. Menten, in *Proceedings of the 3rd Haystack Observatory Meeting "Skylines,"* Ed. by A. D. Haschick and P. T. Ho, Astron. Soc. Pac. Conf. Ser. **16**, 119 (1991).

3. D. M. Cragg, K. P. Johns, P. D. Godfrey, and R. D. Brown, Mon. Not. R. Astron. Soc. **259**, 203 (1992).

4. S. V. Kalenskiǐ, Astron. Zh. **72**, 524 (1995) [Astron. Rep. **39**, 465 (1995)].

5. A. M. Sobolev, D. Cragg, and P. D. Godfrey, Mon. Not. R. Astron. Soc. **288**, 39 (1997).

6. K. M. Menten, C. M. Walmsley, C. Henkel, and T. L. Wilson, Astron. Astrophys. **157**, 318 (1986).

7. A. D. Haschick, K. M. Menten, and W. Baan, Astrophys. J. **354**, 556 (1990).

8. I. E. Val'tts, A. M. Dzyura, S. V. Kalenskiǐ, *et al.*, Astron. Zh. **72**, 22 (1995) [Astron. Rep. **39**, 18 (1995)].

9. S. Liechti and T. L. Wilson, Astron. Astrophys. **314**, 615 (1996).

10. V. I. Slysh, S. V. Kalenskiǐ, I. E. Val'tts, and R. Otrupcek, Mon. Not. R. Astron. Soc. **268**, 464 (1994).

11. V. I. Slysh, S. V. Kalenskiǐ, I. E. Val'tts, and V. V. Golubev, Astrophys. J. Lett. **478**, L37 (1997).

12. W. Batrla and K. M. Menten, Astrophys. J. Lett. **329**, L117 (1988).

13. R. Bachiller and M. Pérez Gutiérrez, Astrophys. J. Lett. **487**, L93 (1997).

14. V. I. Slysh, S. V. Kalenskiǐ, I. E. Val'tts, *et al.*, Astrophys. J., Suppl. Ser. **123**, 515 (1999).

15. V. I. Slysh, S. V. Kalenskiǐ, and I. E. Val'tts, in *Proceedings of the "Astrophysics on Boundaries of Centuries," 1999*, Ed. by N. S. Kardashev, R. D. Dagkesamanskiǐ, and Yu. A. Kovalev, p. 319.

16. P. Friberg, Å. Hjalmarson, S. C. Madden, and W. M. Irvine, Astron. Astrophys. **195**, 281 (1988).

17. S. V. Kalenskiǐ, A. M. Dzura, R. Booth, *et al.*, Astron. Astrophys. **321**, 311 (1997).

18. A. M. Sobolev, B. K. Wallin, and W. D. Watson, Astrophys. J. **498**, 763 (1998).

Translated by S. Kalenskiǐ

Streaming Motions of Molecular Clouds, Ionized Hydrogen, and OB Stars in the Cygnus Arm

T. G. Sitnik, A. M. Mel'nik, and V. V. Pravdikova
Sternberg Astronomical Institute, Universitetskiĭ pr. 13, Moscow, 119899 Russia
Received November 26, 1999

Abstract—The radial velocity fields of molecular clouds, OB stars, and ionized hydrogen in the Cygnus arm ($l \sim 72°$–$85°$) are analyzed. A gradient $\Delta V_{LSR}/\Delta l$ in the mean line-of-sight velocities of molecular clouds and ionized hydrogen due to differential Galactic rotation is detected, and two groups of physically and genetically associated objects moving with different line-of-sight velocities are identified. One of the two molecular-cloud complexes ($l \sim 77.3°$–$80°$) is located within 1 kpc of the Sun, closer to the inner edge of the arm, whereas the other complex ($l \sim 78.5°$–$85°$) lies 1–1.5 kpc from the Sun and is farther from the inner edge of the arm. The residual azimuthal velocities of the objects in both groups are analyzed. The residual azimuthal velocities of the first molecular-cloud complex are directed opposite to the Galactic rotation ($V_{\Theta} \sim -7$ km/s), while those of the second complex are near zero or in the direction of Galactic rotation, independent of the distance to the complex ($V_{\Theta} \geq 1$ km/s). Like the molecular clouds, stars of the Cygnus arm form two kinematic groups with similar azimuthal velocities. On the whole, the mean azimuthal velocities V_{Θ} for the ionized hydrogen averaged over large areas agree with the velocities of either the first or second molecular-cloud complex. In terms of density-wave theory, the observed differences between the magnitudes and directions of the azimuthal velocities of the kinematic groups considered could be due to their different locations within the arm. © *2001 MAIK "Nauka/Interperiodica".*

1. INTRODUCTION

We investigate here the effect of spiral density waves on the interstellar medium of the Cygnus arm. Perturbations of the gravitational potential in a rotating galaxy and the resulting spiral shocks give rise to systematic (streaming) motions of young stars and gas [1, 2]. These streaming motions produce a characteristic residual-velocity field V_{res} for the stars and gas. The residual velocities are determined relative to a reference frame rotating uniformly with linear velocity V_{gal} (the mean circular velocity of Galactic rotation at a given Galactocentric distance): $V_{res} = V_{obs} - V_{ap} - V_{gal}$, where V_{obs} and V_{ap} are the observed heliocentric velocity and the velocity of the solar motion toward the apex, respectively.

Taking into account the influence of shocks, we expect the following behavior of the azimuthal (V_{Θ}) and radial (V_R—along the Galactocentric radius) residual-velocity components for young stars and gas inside the corotation radius [2]. The residual velocities of the stars and gas should be maximum near the inner edge of the arm, which coincides with the shock front. The radial and azimuthal residual velocities of these motions are directed toward the Galactic center and opposite to the Galactic rotation, respectively. The residual velocity decreases in magnitude with distance from the inner edge of the arm. At the outer edge of the arm, the residual velocity V_R is close to zero, and the azimuthal velocity V_{Θ} is in the direction of Galactic rotation.

Thus, the residual azimuthal velocity reverses direction across the arm. The perturbation of the gravitational potential also forces the stars and gas to deviate from circular orbits in the inter-arm space. In contrast to the density-wave arms, the inter-arm radial residual velocity is directed away from the Galactic center.

The interstellar medium, like stars, must react to the spiral density waves propagating through it. The main problem in analyses of streaming motions of interstellar clouds and rarefied gas is the determination of their heliocentric distances. The distances to interstellar clouds are usually derived from their observed line-of-sight velocities and an adopted Galactic rotation curve. When estimating kinematic distances, it is assumed that line-of-sight velocities are determined solely by Galactic rotation and that the residual velocity is zero. Therefore, the residual gas velocity can be determined only if an independent distance estimate is available. However, we would not attempt even a qualitative analysis without the previous discovery of systematic residual motions of OB associations in the Carina and Cygnus arms (Fig. 1a), predicted by density-wave theory [3, 4]. We have also made use of the special observing conditions in the Cygnus arm ($l \sim 70°$–$90°$); namely, it is possible to analyze variations of the azimuthal velocity, which nearly coincides with the radial velocity up to a distance of ~ 2 kpc. Note that only line-of-sight velocities are known for the gas, whereas our analyses of stellar motions included both line-of-sight velocities and proper motions.
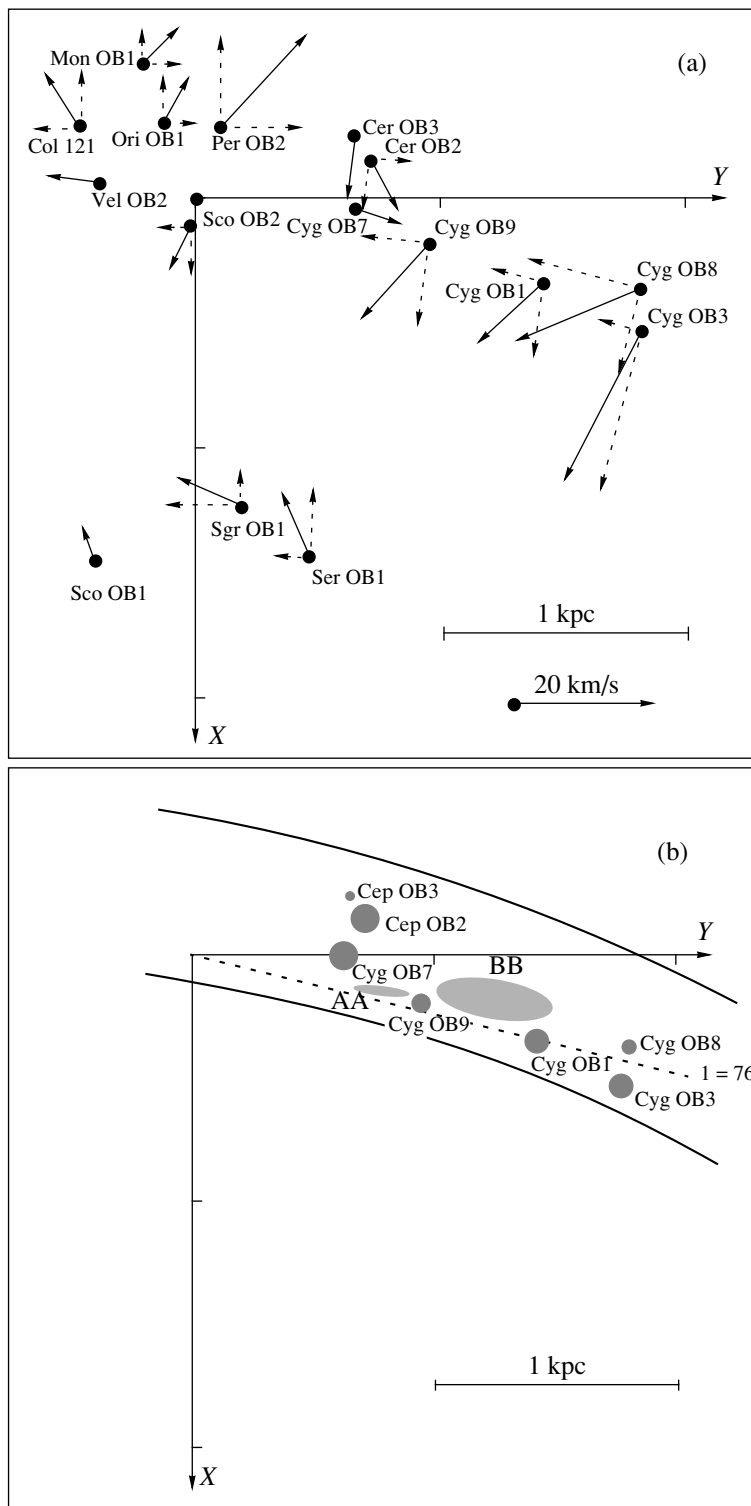
Fig. 1. (a) The observed residual-velocity field of Cygnus-arm associations and the surrounding interarm space. The dashed lines show the radial (V_R) and azimuthal (V_Θ) velocity components. The X axis is directed toward the Galactic center and the Sun is at the coordinate origin. (b) The molecular-cloud complexes AA and BB and Cygnus-arm associations in projection into the Galactic plane. The boundaries of the Cygnus arm for a pitch angle of $i = 10°$ are shown schematically. The dashed line indicates the direction $l = 76°$, which is the adopted boundary separating the Cyg OB1 stars into two groups.

We will investigate the behavior of the interstellar medium in the spiral density wave in the direction of the Cygnus arm ($l \sim 72°–87°$) by analyzing the residual line-of-sight motions of molecular clouds and ionized hydrogen. Section 2 describes streaming motions in Cygnus-arm associations [4]. Section 3 investigates the residual line-of-sight motions and localization of molecular clouds. Section 4 considers the specifics of stellar kinematics of the Cygnus-arm associations and their relationship to molecular clouds. Section 5 investigates the distribution of ionized hydrogen. We conclude that the resulting kinematic pattern is consistent with the predictions of density-wave theory.

2. RESIDUAL RADIAL VELOCITIES OF CYGNUS-ARM OB ASSOCIATIONS

The Cygnus arm contains two star–gas complexes: the distant Cygnus complex ($l \sim 70°–81°$, $b \sim -1.0°…+5.8°$, $r \sim 1.0–1.8$ kpc), and nearby Cygnus–Cepheus complex ($l \sim 81°–122°$, $b \sim -5°…+12.5°$, $r \sim 0.6–0.9$ kpc) [5]. The Cyg OB1, OB2, OB3, OB8, and OB9 associations belong to the Cygnus complex and Cyg OB7, OB4, Cep OB2, OB3, OB4, and Cas OB14 belong to the Cygnus–Cepheus complex (Fig. 1b). The Galactic coordinates l and b and the names of associations at Galactic longitudes $l \sim 70°–90°$ are given in the table. A detailed analysis of the residual velocities of Cygnus-arm OB associations was performed by Sitnik and Mel'nik [4]. Here we make note only of the main results of that study.

We determined the residual velocities of stars in OB associations and interstellar clouds using the Galactic rotation velocity, V_{gal}, and the velocity of the Sun toward the apex, V_{ap}, derived from an analysis of Cepheid motions (see version A in [6] and Table 1 in [7]). We adopted a Galactocentric distance for the Sun $R_0 = 7.1$ kpc [6, 8]. We assumed that the heliocentric distances r of associations were 80% of the distances of Blaha and Humphreys [9], based on the fact that this results in an OB-association distance scale that kinematically matches the Cepheid distance scale used in the rotation-curve solution [7]. In other words, we used a so-called short distance scale. The table gives the heliocentric distances r, median line-of-sight velocities (V_{LSR}), residual line-of-sight velocities $V_{r, res}$, and residual azimuthal velocities V_Θ for the Cygnus-arm associations (see also [4]).

Figure 1a shows the distribution of residual azimuthal and radial velocities of the Cygnus-arm associations and in the surrounding inter-arm region [4]. The azimuthal velocities of associations near the inner edge of the Cygnus arm (at Galactic longitudes $l \sim 70°–80°$) are directed opposite to the Galactic rotation, and have values $V_\Theta \sim -16…-3$ km/s (see also table). The azimuthal velocities of associations at $l \sim 84°–122°$ (closer to the outer edge) are in the direction of Galactic rotation and have values $V_\Theta \sim 0–7$ km/s. The residual radial velocities V_R of all associations in this region are directed toward the Galactic center and their magnitude

in the Cygnus-arm cross section decreases with Galactocentric distance, from 10–23 to 2–8 km/s. Analysis of the stability of the derived residual velocities showed that variations in the rotation-curve parameters and the distance scale used over a broad range do not lead to qualitative changes in the residual velocity field in the Cygnus arm (see Fig. 6 in [4]).

The derived variations of the magnitude and direction of the residual velocities V_R and V_Θ for Cygnus-arm associations testify to the density-wave nature of the spiral arm, and its location inside the corotation radius [1, 2, 4]. For convenience, we will refer to regions where the azimuthal motions of associations are opposite to or coinciding with the direction of Galactic rotation as the inner and outer arm regions, respectively.

3. RESIDUAL VELOCITIES OF MOLECULAR CLOUDS IN THE DIRECTION $l \sim 73°–87°$

The Cygnus arm and the Sun are located at approximately the same Galactocentric distance, so that, in the longitude interval $l \sim 70°–90°$, we are looking at a cross section of the Cygnus arm (Fig. 1b). The line of sight runs along the arm (at least up to heliocentric distances of ~ 2 kpc) and is almost tangential to circular orbits. The residual velocities of stars and gas $V_{r, res}$ must therefore nearly coincide with the azimuthal residual velocity V_Θ, as can be seen from a comparison of $V_{r, res}$ and V_Θ for OB associations (see table).

If streaming motions are induced by density waves, the residual line-of-sight velocities of interstellar clouds and gas $V_{r, res}$ should change direction across the arm, from opposite of the Galactic rotation near the inner edge of the arm to coinciding with it at the outer edge [1, 2]. Since the inner edge of the Cygnus arm is seen at smaller Galactic longitudes (Fig. 1), these longitudes should be characterized by predominantly Sunward residual motions, whereas the residual motions at larger longitudes should be directed away from the Sun. To look for density-wave effects, we analyzed the distribution of CO in the direction toward the Cygnus arm.

3.1. Analysis of the CO Distribution in the Direction of the Cygnus Arm

Leung and Thaddeus [10] have published detailed CO emission maps for the region $l \sim 73°–87°$, $b \sim -4°…+5°$. Figure 2 shows the latitude-averaged CO distribution in the (l, V_{LSR}) plane adopted from [10]. Two molecular-cloud ridges can be identified in the velocity interval $\Delta V_{LSR} \sim -25…+25$ km/s (Fig. 2), which we will refer to as AA ($l \sim 77.3°–80°$, $\Delta V_{LSR} \sim -6…+4$ km/s) and BB ($l \sim 78.5°–85°$, $\Delta V_{LSR} \sim -1…+13$ km/s). We distinguished these clouds—shaded areas in Fig. 2—around the brightest CO emission features at the level 3.8 K deg [10]. The Galactic longitudes, names, and velocity intervals ΔV_{LSR} where a cloud (or part of a cloud) is

Table

Associations							CO-clouds		
l, deg	b, deg	name	r, kpc	V_{LSR}, km/s	$V_{\text{r, res}}$, km/s	V_Θ, km/s	name	ΔV_{LSR}, km/s	$V_{\text{r, res}}$, km/s
71–74	0.5–3.6	Cyg OB3	1.8	9 ± 2	−4 ± 3	−5			
74–78	−0.8–3.0	Cyg OB1	1.5	2 ± 2	−7 ± 2	−8			
74–76		Cyg OB1B		13 ± 3		2			
76–78		Cyg OB1A		−2 ± 2		−11			
76.3–79.5	2.0–5.8	Cyg OB8	1.8	−8 ± 3	−15 ± 4	−15			
77–80	0.5–2.2	Cyg OB9	1.0	0 ± 5	−7 ± 5	−8			
77.3–80			1.0				AA	−6…+4	−8
78–80			1.5				BB	+3…+13	1
80–80.7	0.7–1.3	Cyg OB2	1.5						
80–81.7			1.5				BB	+3…+8	0
81.7–82			1.5				AA–BB	−4…+11	−1
82–83			1.5					+3…+6	1
83–84			1.5					−1…+6	0
			1.0						−1
84–85			1.5				AA–BB	−4…+5	−1
			1.0						−2
84–96	−4.9–9.0	Cyg OB7	0.7	8 ± 2	7 ± 2	7			

identified are summarized in the table. Bright CO emission features are projected onto various parts of the plane of the sky (see Fig. 8 in [10]). Therefore, the BB and AA ridges should be viewed as complexes of molecular clouds that could be located at different heliocentric distances. In particular, the features of BB seen at negative velocities in the direction $l \sim 81.8°–82°$ and $l \sim 84.5°–85°$ could be extensions of AA.

The most striking feature of Fig. 2 is the systematic decrease of the line-of-sight velocities V_{LSR} of bright CO emission features with increasing Galactic longitude, especially conspicuous for ridges BB. (The radial velocity V_{LSR} is referred to the local standard of rest; i.e., it is corrected for the solar motion toward the standard apex, $V_{LSR} = V_{\text{obs}} - V_{\text{ap}}$). This monotonic decrease of V_{LSR} must be due to a decrease of the Galactic rotational velocity $V_{\text{gal}}(l, r)$ with longitude, since V_{gal} depends only slightly on distance up to $r \sim 2$ kpc in the direction considered. What we actually observe is the variation of the Galactic rotational velocity with Galactocentric distance. To illustrate this, we show in Fig. 3 the mean line-of-sight velocities V_{LSR} of molecular clouds AA and BB superimposed on a family of curves defining the Galactic rotational velocity V^*_{gal} at each longitude for various Galactocentric distances. We computed the mean line-of-sight velocities V_{LSR} of the clouds by averaging the corresponding values for each longitude over the shaded areas shown in Fig. 2. We computed the Galactic rotational velocity V_{gal} using a rotation curve based on the

motions of Cepheids [6]. To compare V_{LSR} and V_{gal}, we introduced a correction to allow for the difference between the velocity of the standard solar motion ($V_X = 10$ km/s, $V_Y = 15$ km/s, $V_Z = 7$ km/s) [11] and the solar velocity inferred from the Cepheid-motion analysis ($V_X = 10$ km/s, $V_Y = 13$ km/s, $V_Z = 7$ km/s) [6]. We added this correction, equal to $\Delta V_{\text{ap}} = 2 \sin l \sim 2$ km/s, to the velocity of Galactic rotation V_{gal}. Both velocities shown in Fig. 3, V_{LSR} and $V^*_{\text{gal}} = V_{\text{gal}} + \Delta V_{\text{ap}}$, are thus corrected for the solar motion toward the standard apex.

It is evident from Fig. 3 that the mean kinematic distances of the molecular-cloud complexes can be roughly estimated from the relative positions of the observed line-of-sight velocities V_{LSR} of the molecular clouds relative to the family of Galactic-rotation curves. In the longitude interval $l \sim 77°–85°$, the observed line-of-sight velocities V_{LSR} of molecular clouds AA and BB coincide, on average, with the Galactic rotational velocities for heliocentric distances of 3 and 1.5 kpc, respectively. These are precisely the distances of molecular clouds identified by OH absorption [12], CH emission [13], and H_2CO absorption [14] (see references in the above papers). These molecular clouds were observed at the same line-of-sight velocities V_{LSR} as the molecular-cloud complexes AA and BB. However, in view of the distribution of residual velocities of OB associations in the Cygnus arm, we suggest that a different location of the AA clouds is possible.
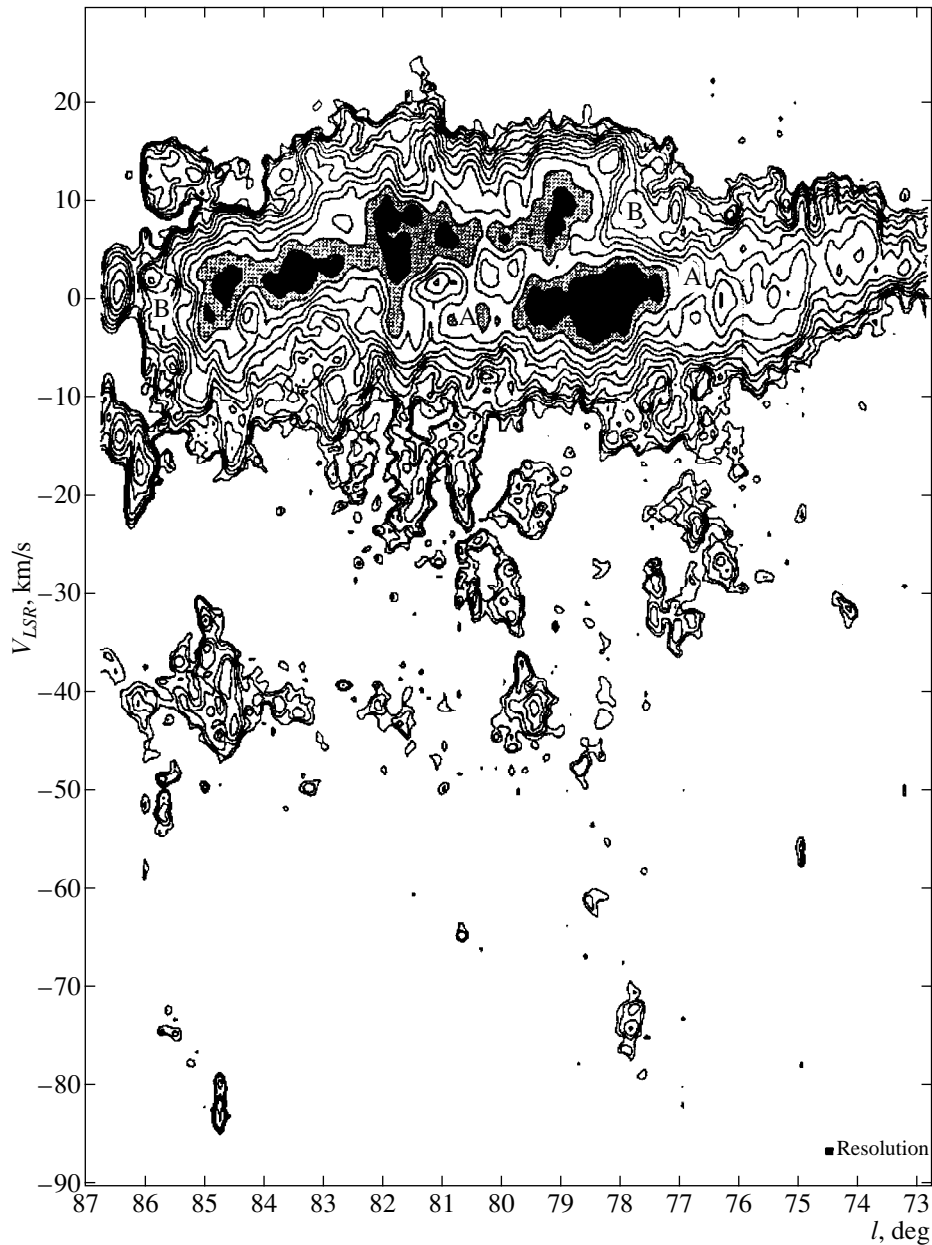
Fig. 2. The distribution of CO emission in the (l, V_{LSR}) plane summed over the interval $\Delta b \sim -4°\ldots+5°$ [10]. The lower level corresponds to 3σ (0.38 K deg) and each subsequent level is 1.33 times the previous one. The clouds AA and BB are indicated by shaded areas.

3.2. Location and Residual Radial Velocities of Molecular-Cloud Complex AA

AA ($l \sim 77.3°–80°$, $b \sim -1.6°\ldots+1.5°$, $\Delta V_{LSR} \sim -6\ldots+4$ km/s) is the brightest extended CO-emission feature seen toward Cyg X (Fig. 2). (We set the Galactic latitude boundaries for AA based on the distribution of CO emission in the plane of the sky for the corresponding interval of line-of-sight velocities and Galactic longitudes (see Fig. 8 in [10]).)

The AA clouds are projected against an area occupied by associations of the inner part of the cloud, Cyg OB9

and, partially, Cyg OB1, which are located within 1.5 kpc of the Sun. The residual line-of-sight velocities of these associations are directed toward the Sun and have values $V_{r,\,res} \sim -7$ km/s [4]. If the molecular clouds AA, like the associations, are located near the inner edge of the arm, they, too, must have negative residual velocities $V_{r,\,res}$. Allowance for this velocity reduces the inferred distances to the clouds (Fig. 3).

In fact, there is certain circumstantial evidence that the AA clouds are nearby. In the direction in which most of the clouds of complex AA are observed, i.e.,

$l \sim 77°–82°$, $b \sim 0°–4°$, there is strong optical absorption ($A_V \sim 3–6^m$) at heliocentric distances <1 kpc (see Fig. 8a and areas 76/0, 78/1, 80/1, and 81/3 in [15]). In other directions toward the area considered $l \sim 70°–100°$, $b \sim -5°…+5°$, the extinction has similar or lower values ($A_V \sim 3–4^m$) at larger distances. It is very probable that the brightest cloud of CO emission coincides with a region of isolated interstellar absorption, not only in the plane of the sky, but also in heliocentric distance; i.e., AA lies no further than 1 kpc from the Sun. Based on their comparison of the distributions of CO emission and absorbing material toward $l \sim 65°–100°$, Dame and Thaddeus [16] also concluded that some of the molecular clouds were close to the Sun, and associated with a well-known region of strong optical absorption—the so-called Cygnus Dust Tongue, at a heliocentric distance of $r \sim 0.7$ kpc (see also [17] and references therein).

There are independent estimates of the distance to the stellar and gas populations in this region. The star WR 143 and association Cyg OB9, with distances of $r \sim 0.8$ [18] and 1 kpc (see table), respectively, lie in the direction of AA. Since the optical absorption exceeds 3^m for 63% of the stars of Cyg OB9 [9], this association is most likely located behind AA. The well-known compact star-forming region ON2 (G75.8+0.4) and the star WR 142 ($r \sim 0.9$ kpc [18]) are projected against the region occupied by the wedges of the AA ridges. WR 142 and ON2 are associated with the young open cluster Be 87, whose photometric distance is 0.9 kpc [19].

Thus, the molecular-cloud complex AA with its embedded star-forming regions may actually be a nearby object located within 1 kpc of the Sun (Fig. 1b). The velocity of Galactic rotation toward $l \sim 77°–80°$ is $V^*_{gal} = 6–7$ km/s at a heliocentric distance of $r \sim 1$ kpc. In this case, the residual radial velocity of AA, $V_{r, res} = V_{LSR} - V^*_{gal}$, falls in the interval $-12…+3$ km/s. This is equal, on average, to $V_{r, res} \sim -7$ km/s, and is therefore close to the velocities $V_{r, res}$ of the inner-arm associations Cyg OB9 and OB1 at heliocentric distances of 1–1.5 kpc (see table). Note that, in the direction $l \sim 77–85°$, the velocity of Galactic rotation V^*_{gal} varies by less than 3 km/s over the rather broad distance interval from 0.5 to 2 kpc and, consequently, the residual line-of-sight velocities of clouds are only weakly sensitive to distance errors (Fig. 3).

The observed line-of-sight velocities V_{LSR} of molecular clouds AA can therefore be explained by density-wave effects without putting the clouds at a heliocentric distance of 3 kpc. Figure 4 and table give the residual velocities $V_{r, res}$ of the molecular-cloud complex for an assumed heliocentric distance of $r = 1$ kpc. It is evident from Figs. 3 and 4 that, if the distance of complex AA is less than 3 kpc, its residual radial velocity $V_{r, res}$ should always be negative. Therefore, the azimuthal component of the residual velocity of AA is opposite to the Galactic rotation, as must be the case for objects in the inner part of a density-wave arm.
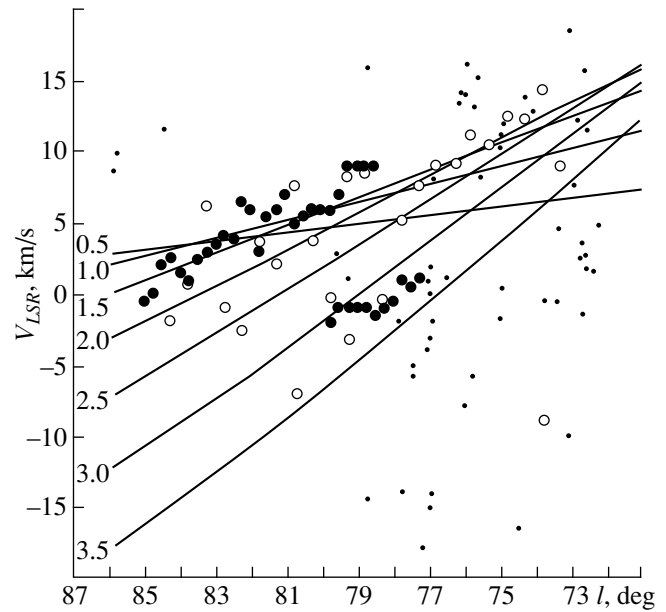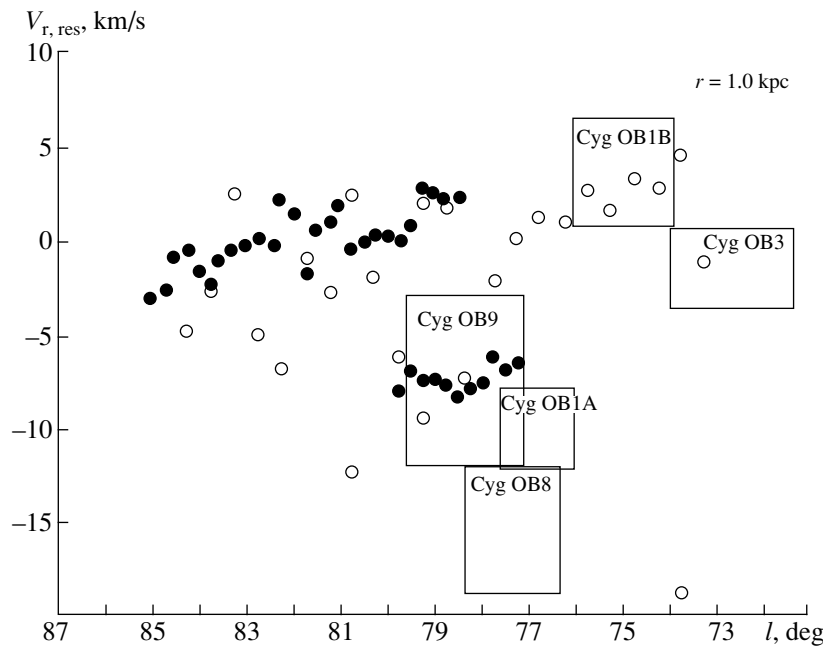
Fig. 3. Mean line-of-sight velocities V_{LSR} of molecular clouds AA and BB (filled circles), the ionized hydrogen (open circles), and stars of the Cyg OB1, OB3, OB9, and OB8 associations (dots), together with a family of curves defining the velocity of Galactic rotation V^*_{gal} at each longitude for various heliocentric distances. Distances (in kpc) are given to the left of the curves. Both V_{LSR} and V^*_{gal} are corrected for the solar motion toward the standard apex. Only stars with V_{LSR} errors of less than 15 km/s are shown.

It is quite possible that complex AA, which is a relatively compact object in the plane of the sky, is actually extended along the line of sight and, consequently, along the edge of the arm (Fig. 1b). This could explain the unique optical absorption in this direction.

3.3. Location and Residual Radial Velocities of Molecular-Cloud Complex BB

The extended molecular-cloud complex BB ($l \sim 78.5°–85°$, $\Delta V_{LSR} \sim -1…+13$ km/s; see Fig. 2) is seen projected against a region occupied by associations of both the inner (Cyg OB9 and Cyg OB8; $l < 80°$) and outer (part of Cyg OB7, $l > 84°$) arm (see table). No associations are observed at longitudes $l \sim 80°–84°$, i.e., toward most of BB.

It is clear from Fig. 3 that, at each longitude except $l > 83°$, the mean line-of-sight velocities V_{LSR} of bright features of the molecular clouds BB are greater than or equal to the maximum possible velocities of Galactic rotation V^*_{gal}. (In this direction, the Galactic rotational velocities peak within 2 kpc). Therefore, most of the BB clouds have positive or almost zero residual line-of-sight velocities $V_{r, res}$, independent of their heliocentric distances (Fig. 4), as is characteristic of the central and outer arm regions. It is precisely such line-of-sight stel-

Fig. 4. Residual velocities V_Θ of molecular clouds AA and BB (filled circles), the ionized hydrogen (open circles), and Cygnus-arm associations (rectangles) determined for heliocentric distance 1 kpc. Two groups, A and B, are identified in the Cyg OB1 association.

lar stream patterns with positive $V_{r,res}$ that Sitnik and Mel'nik [4] found in associations of the outer part of the Cygnus arm, including Cyg OB7 (Fig. 1a).

We can say the following about distances to the molecular-cloud complex BB.

(1) Numerous analyses of extinction in the direction of the Cygnus arm indicate that the dust is concentrated in the same regions as the OB stars (see, e.g., [20]), and that the photometric distances to Cygnus OB associations are 0.7–1.8 kpc (see table).

(2) The relative positions of the complexes AA and BB in the plane of the sky and their kinematics suggest that BB is located near the middle of the arm, implying a minimum residual azimuthal velocity. The kinematic distance of BB corresponding to the minimum residual velocity $V_{r,res}$ is 1–1.5 kpc (Fig. 3).

(3) Dame and Thaddeus [16] believe that some molecular clouds at $l \sim 65°–100°$ are associated with the radio source Cyg X, which is extended along the arm and has (according to [16]) a heliocentric distance of $r \sim 1.7$ kpc (the molecular-cloud complex BB, in our case).

Apparently, BB consists of molecular clouds at distances of ~1 to ~1.5 kpc (Fig. 1b).

To summarize, we have direct evidence for variations of the residual line-of-sight velocities $V_{r,res}$ (or V_Θ) of molecular clouds across the Cygnus arm. Given the relative positions of molecular clouds AA and BB, their residual velocities, and the fact that the Galactic spiral arms are trailing, we conclude that complexes AA and BB are located in different parts of the arm cross section.

Figure 1b shows schematically the positions of the molecular clouds and Cygnus-arm associations. Molecular-cloud complex AA ($l \sim 77.3°–80°$), which is located within 1 kpc of the Sun, lies near the middle-arm line and has zero or positive residual velocities $V_{r,res}$. Although AA and BB are located at different heliocentric distances, they represent a cross section of the arm in the plane of the sky. Therefore, the change in the direction of V_Θ for the molecular clouds observed at $l \sim 78°–79°$, which is opposite to and coincides with the direction of Galactic rotation in complexes AA ($V_\Theta \sim V_{r,res} \sim -7$ km/s) and BB ($V_\Theta \sim V_{r,res} \geq +1$ km/s), respectively, is characteristic of the velocity-variation pattern predicted by density-wave theory.

4. LINE-OF-SIGHT VELOCITIES OF OB STARS IN CYGNUS-ARM ASSOCIATIONS

Figure 3 also shows the line-of-sight velocities V_{LSR} of stars in the Cyg OB1, OB3, OB8, OB9, and OB7 associations, which are located in the region studied and have heliocentric distances of 0.7–1.8 kpc. We adopted the lists of association stars from the catalog of Blaha and Humphreys [9] and their radial velocities from the WEB catalog [21].

The distribution of line-of-sight velocities V_{LSR} of stars in the interval $l \sim 72°–80°$ proved surprising. The stars in Cyg OB1, Cyg OB3, Cyg OB8, and Cyg OB9 separated into two groups with line-of-sight velocities $V_{LSR} < 5$ km/s and $V_{LSR} > 7$ km/s (Fig. 3). The histogram of stellar velocities V_{LSR} has two pronounced maxima (Fig. 5). This bimodal distribution indicating two

velocity groups is due primarily to stars of the richest association, Cyg OB1. The kinematically identified stellar groups in Cyg OB1 are shifted relative to each other in Galactic longitude (Fig. 6a). The stars of Cyg OB1 belonging to the first group (A), have $l \sim 76°–78°$ and move with a median velocity of $V_{LSR} = -2 \pm 1$ km/s, whereas stars belonging to the second group (B) have $l \sim 74°–76°$ and move with a median velocity of $V_{LSR} = 13 \pm 3$ km/s (Figs. 3, 6a). The stars of the first group are concentrated in the (l, V_{LSR}) plane near the molecular-cloud complex AA (Fig. 3); i.e., they move with the same radial velocities as the AA clouds. However, in the plane of the sky, these stars lie outside regions of bright CO emission. The radial velocities of stars of the second group are in good agreement with the longitude dependence of the mean V_{LSR} values for molecular clouds BB (Fig. 3), and continue the linear $V_{LSR}(l)$ relation toward lower Galactic longitudes ($l \sim 73°–76°$).

The agreement of the line-of-sight velocities of stars of the first and second groups with those of molecular clouds AA and BB (Fig. 3), respectively, can be explained as follows. OB stars of Cyg OB1, like those of other Cygnus-arm associations, formed from clouds in extended molecular–dust complexes. AA and BB could be the remnants of such complexes. The stars have the same velocities as the remnants of their parent cloud complexes. It is possible that stars of the first and second groups in Cyg OB1 do not only have different line-of-sight velocities, but also, like the clouds, have different heliocentric distances. Figure 1b shows how Cyg OB1 stars with positive and negative residual line-of-sight velocities could be observed along the same line of sight in a spiral arm with pitch angle $i = 10°$ [22, 23]. However, we were not able to separate these kinematically distinct groups of the Cyg OB1 association into radial subgroups. This might suggest that the separation between the two groups is less than the standard errors in their heliocentric distances, 0.3 kpc. Differences in distance estimates for Cyg OB1, 1.8 kpc [9] and 1.2 kpc [24], may be partially due to the fact that the two stellar groups have been combined into a single association. Since photometric distances to the associations are known (see table), as we can see from Fig. 3, the residual line-of-sight velocities of stars of one group at $l < 80°$ are directed opposite to the Galactic rotation, while those of the other group are either close to zero or are directed along the Galactic rotation (Fig. 4).

Figure 6b shows how the residual line-of-sight velocities $V_{r, res}$ of stars in the Cyg OB1, OB3, OB8, and OB9 associations depend on the absolute bolometric magnitude M_{bol}. (See [3] for a description of corrections applied to the M_V values adopted from Blaha and Humphreys [9].) We can see from this figure that stars with streaming motions opposite of the Galactic rotation are, on average, more luminous and possibly younger than stars with streaming motions along the direction of Galactic rotation. Consequently, we expect the stars of different kinematic groups in the Cygnus arm to have different ages.
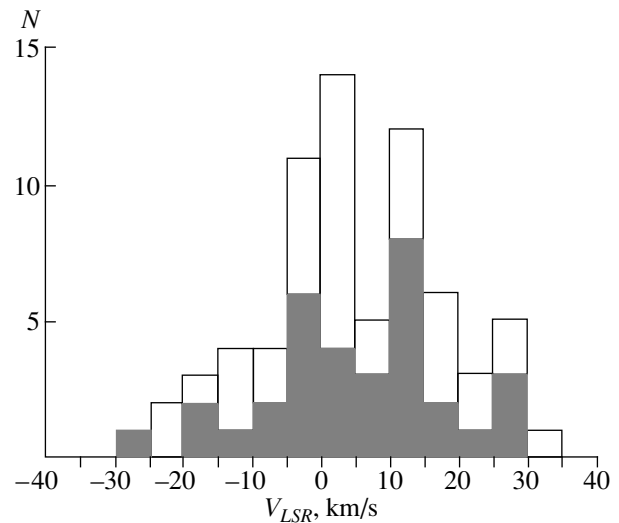
Fig. 5. Histograms of V_{LSR} for stars of the Cyg OB1, OB3, OB9, and OB8 associations. The shaded area is the velocity histogram for the stars of Cyg OB1.

Thus, the stars of Cygnus-arm associations and the remnants of the parent molecular clouds form two kinematic groups, with the residual azimuthal velocities of one group directed opposite to the Galactic rotation and those of the other group being close to zero or directed along the Galactic rotation. Since stars are genetically and physically associated with molecular clouds, it is possible that stars with $V_{r, res}$ directed opposite to the Galactic rotation have, like AA and BB, different locations in the arm cross section. Should this be the case, the direction of the residual velocities of young stars and molecular clouds could be interpreted in terms of density-wave effects in the gaseous subsystem of the Galaxy.

5. IONIZED HYDROGEN TOWARD GALACTIC LONGITUDES $l \sim 72.5°–85°$

We used the database of Lozinskaya *et al.* [17] to analyze the radial velocity field of ionized hydrogen in the direction of the Cygnus arm ($l \sim 72.5°–85°$, $b \sim -1°…+4°$). The ionized hydrogen line-of-sight velocities were determined at the positions of intensity peaks for each feature of the H_α profile. (See [17] for a detailed description of the observations and their reduction.)

The bulk of the ionized gas, which is described by the bright component in the line profile, emits in the radial velocity interval from –20 to +25 km/s. This nearly coincides with the radial velocity interval for bright CO emission associated with the Cygnus arm. To compare the line-of-sight velocities V_{LSR} of the ionized hydrogen and molecular clouds, we averaged the velocities of the main component of the H_α line over areas with $\Delta l = 0.5°$ and $\Delta b = 5°$ [17]. Figure 3 shows the resulting velocities. Note that the number of main-line velocity measurements per area varies from 100–970 V_{LSR} values
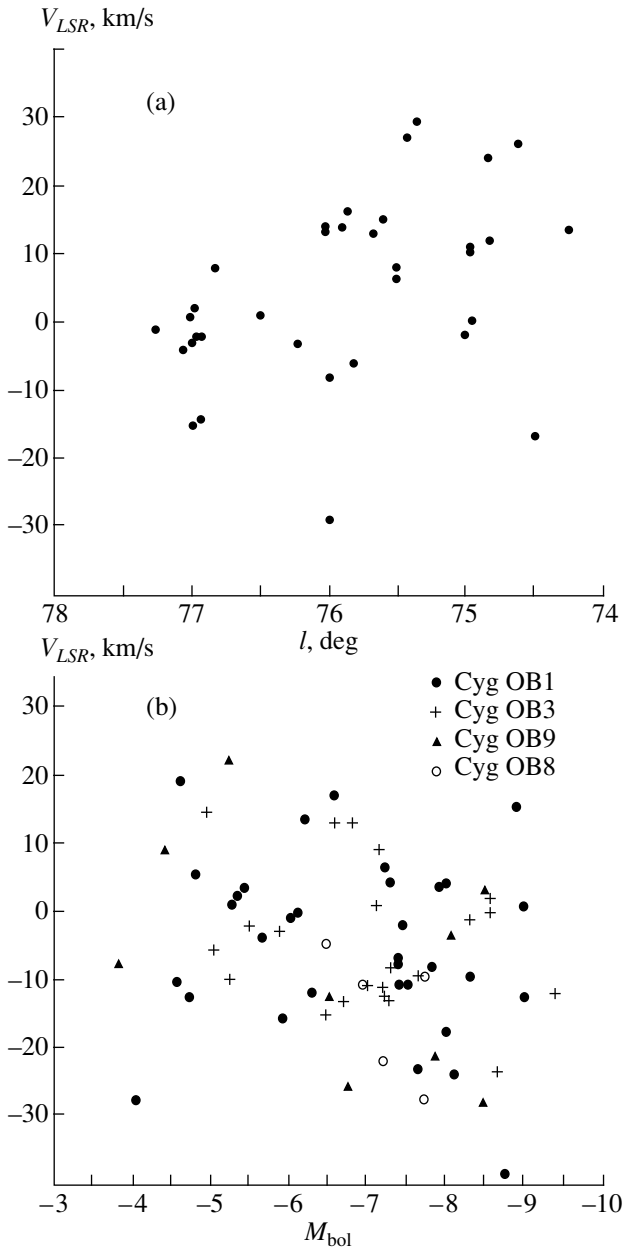
Fig. 6. (a) Dependence of V_{LSR} for stars in the Cyg OB1 association on Galactic longitude and (b) dependence of $V_{r,\,res}$ for stars in Cygnus-arm associations on M_{bol}.

in the interval $l \sim 73°–82.5°$ to 20–40 in other regions. Thus, the mean ionized-hydrogen velocity has the highest frequency of occurrence in each area.

The distributions of the mean velocities V_{LSR} of the main H_α component and of molecular clouds are in good agreement (Fig. 3). The gradient of line-of-sight velocities V_{LSR} of the bulk of ionized hydrogen in Galactic longitude is, as for the molecular clouds, due to the fact that the Galactic rotational velocity decreases with longitude (see also [17]). The linear dependence of the HII radial velocity V_{LSR} at Galactic longitudes $l \sim 72.5°–77°$ continues the similar $V_{LSR}(l)$ dependence for the molecular

clouds of ridges BB (Fig. 3). In this region, ionized hydrogen is observed at positive line-of-sight velocities that are close to the corresponding velocities for the second group of Cyg OB1 stars. Both in the interval $l \sim 77°–80°$, where both molecular clouds are observed, and in the interval $l \sim 80°–85°$, the ionized hydrogen has line-of-sight velocities that are either equal to those of the BB or AA molecular-cloud complexes, or fall in the interval between the mean velocities of the two clouds. This could be partially due to the fact that the mean velocities of the ionized gas were derived for large areas that overlap with both clouds. (The mean ionized-hydrogen velocities derived for a finer partition— e.g., into 0.5×0.5 deg^2 areas—are, indeed, close to the mean velocities of the clouds observed in the corresponding directions). Furthermore, we cannot rule out the possibility of effects due to peculiar gas motions driven by ionizing radiation and stellar winds from young stars in such a dynamically active region as Cygnus [17], especially since the observing coverage is higher toward HII regions than between them.

Since the ionizing radiation is produced by stars of the Cyg OB1, OB2, OB3, OB8, OB9, and OB7 associations, most of the ionized hydrogen is located in the regions occupied by these associations; i.e., at photometric distances of 0.7–1.8 kpc. OB stars and the hydrogen they have ionized are primarily observed outside molecular clouds, although the Galactic longitude distribution of the radial velocities of the bulk of ionized hydrogen and OB stars agrees with the corresponding distribution for CO emission. Figure 4 shows the residual azimuthal velocities of the ionized hydrogen $V_{r,\,res}$ for a heliocentric distance of 1 kpc. On the whole, the ionized-hydrogen streaming motions are in agreement with those for either AA or BB.

6. CONCLUSIONS

We have analyzed the distribution of young stars, molecular clouds, and ionized hydrogen in the direction of the Cygnus arm ($l \sim 72°–85°$) and discovered the following features.

(1) There is a considerable radial velocity gradient $\Delta V_{LSR}/\Delta l$ for molecular clouds and ionized hydrogen due to differential Galactic rotation (Fig. 3).

(2) We have identified two kinematically distinct groups of genetically and physically associated objects.

(a) Two molecular-cloud ridges have mean line-of-sight velocities $\Delta V_{LSR} \sim -2\ldots+1$ km/s (AA) and $\Delta V_{LSR} \sim 0\ldots+9$ km/s (BB) (Figs. 1b, 2, 3).

(b) Of two OB-star groups in Cygnus-arm associations, the first has V_{LSR} that are negative or close to zero and is located near the clouds AA, and the second is located outside the clouds BB but has the positive velocities expected for clouds BB at these Galactic longitudes (Figs. 3, 5). In the case of Cyg OB1, the mean velocities of the OB-star groups are -2 ± 1 km/s and $+13 \pm 3$ km/s, respectively.

(c) The hydrogen ionized by Cygnus-arm stars and emitting in the interval $l \sim 72°$–$85°$ has mean radial velocities corresponding to both AA and BB (Fig. 3).

(3) The molecular clouds are situated at different heliocentric distances and at different locations in the Cygnus-arm cross section.

(a) Clouds AA ($l \sim 77.3°$–$80°$) are within 1 kpc of the Sun and are closer to the inner edge of the arm.

(b) Clouds BB ($l \sim 78.5°$–$85°$) are located at heliocentric distances of 1–1.5 kpc and are further from the inner edge of the arm.

(4) The residual azimuthal velocities V_Θ of the two groups of objects have opposite directions.

(a) The nearby clouds AA, most stars in Cyg OB1 (Cyg OB1 A group), OB3, OB9, and OB8, and a small fraction of the ionized hydrogen move opposite to the Galactic rotation, with $V_\Theta \sim -13...-2$ km/s (Fig. 4).

(b) The more distant BB clouds, the remaining stars of Cyg OB1 (Cyg OB1 B), OB3, OB9, and OB8, and most of the ionized hydrogen have velocities $V_\Theta \sim -2...+5$ km/s; i.e., they are close to zero or are directed along the Galactic rotation (Fig. 4).

The large-scale motions of molecular clouds, OB stars, and ionized hydrogen are dominated by Galactic rotation and residual motions due to spiral density-wave effects. The role of Galactic rotation is clearly illustrated by the gradient of the mean line-of-sight velocities of the molecular clouds and ionized hydrogen observed along a 13° interval of Galactic longitude (corresponding to more than 200 pc at an average distance of 1 kpc). The role of density-wave effects is demonstrated by the kinematic signatures of the residual azimuthal velocities of molecular clouds, ionized hydrogen, and OB stars in the observed field. Analysis of the relative positions and velocity fields of molecular clouds indicates that the azimuthal component of the residual velocity reverses direction across the Cygnus arm: from being opposite of the Galactic rotation (clouds AA) to coinciding with it (clouds BB). Since the stellar and gaseous populations of each group are genetically and physically related, the OB stars of the Cygnus-arm associations and ionized hydrogen in each of the two kinematical groups should, like the molecular clouds, have different locations in the arm cross section.

Thus, in spite of problems with localizing the clouds and ionized hydrogen, we were able to detect the azimuthal-velocity variations characteristic of density-wave arms: a decrease of the magnitude of V_Θ, with a possible reversal of its direction. The most common residual motions in the interstellar medium of the Cygnus arm, like the residual motions of stars in associations in this arm, reflect its density-wave nature.

REFERENCES

1. C. C. Lin, C. Yuan, and F. H. Shu, Astrophys. J. **155**, 721 (1969).
2. W. W. Roberts, Astrophys. J. **158**, 123 (1969).
3. A. M. Mel'nik, T. G. Sitnik, A. K. Dambis, *et al.*, Pis'ma Astron. Zh. **24**, 689 (1998) [Astron. Lett. **24**, 594 (1998)].
4. T. G. Sitnik and A. M. Mel'nik, Pis'ma Astron. Zh. **25**, 194 (1999) [Astron. Lett. **25**, 156 (1999)].
5. Yu. N. Efremov and T. G. Sitnik, Pis'ma Astron. Zh. **14**, 817 (1988) [Sov. Astron. Lett. **14**, 347 (1988)].
6. A. K. Dambis, A. M. Mel'nik, and A. S. Rastorguev, Pis'ma Astron. Zh. **21**, 331 (1995) [Astron. Lett. **21**, 291 (1995)].
7. T. G. Sitnik and A. M. Mel'nik, Pis'ma Astron. Zh. **22**, 471 (1996) [Astron. Lett. **22**, 422 (1996)].
8. E. V. Glushkova, A. K. Dambis, A. M. Melnik, and A. S. Rastorguev, Astron. Astrophys. **329**, 514 (1998).
9. C. Blaha and R. M. Humphreys, Astron. J. **98**, 1598 (1989).
10. H. O. Leung and P. Thaddeus, Astrophys. J., Suppl. Ser. **81**, 267 (1992).
11. P. G. Kulikovskiǐ, *Stellar Astronomy* (Nauka, Moscow, 1985).
12. M. I. Pashchenko, Astron. Zh. **50**, 685 (1973) [Sov. Astron. **17**, 438 (1973)].
13. O. E. H. Rydbeck, E. Kollberg, A. Hjalmarson, *et al.*, Astron. Astrophys., Suppl. Ser. **31**, 333 (1976).
14. A. Piepenbrink and H. J. Wendker, Astron. Astrophys. **191**, 313 (1988).
15. Th. Neckel and G. Klare, Astron. Astrophys., Suppl. Ser. **42**, 251 (1980).
16. T. M. Dame and P. Thaddeus, Astrophys. J. **297**, 751 (1985).
17. T. A. Lozinskaya, V. V. Pravdikova, T. G. Sitnik, *et al.*, Astron. Zh. **75**, 514 (1998) [Astron. Rep. **42**, 453 (1998)].
18. I. Lundstrom and B. Stenholm, Astron. Astrophys., Suppl. Ser. **58**, 163 (1984).
19. D. G. Turner and D. Forbes, Publ. Astron. Soc. Pac. **94**, 789 (1982).
20. N. B. Kalandadze and L. P. Kolesnik, Astron. Astrophys. **32**, 57 (1977).
21. M. Duflot, P. Figon, and N. Meyssonier, Astron. Astrophys., Suppl. Ser. **114**, 269 (1995).
22. Ju. N. Efremov, Astron. Astrophys. Trans. **15**, 3 (1998).
23. A. M. Mel'nik, A. K. Dambis, and A. S. Rastorguev, Pis'ma Astron. Zh. **25**, 602 (1999) [Astron. Lett. **25**, 518 (1999)].
24. C. D. Garmany and R. E. Stencel, Astron. Astrophys., Suppl. Ser. **94**, 214 (1992).

Translated by A. Dambis

The Dust Envelope of the Symbiotic Nova HM Sge

M. B. Bogdanov[1] and O. G. Taranova[2]

[1]*Chernyshevskiĭ State University, Saratov, Russia*
[2]*Sternberg Astronomical Institute, Universitetskiĭ pr. 13, Moscow, 119899, Russia*
Received March 28, 2000

Abstract—We have studied the brightness and color variations of the symbiotic nova HM Sge based on long-term *UBVRJHKLM* photometry of the star and data on its energy distribution in the middle infrared (7.7–22.7 µm) obtained with the low-resolution spectrometers of the IRAS satellite and ISO orbital observatory. We have also calculated models for the steady-state, spherically symmetrical, extended dust envelope of the star for two extreme heating cases: heating only by radiation from the cool component of the system and by the combined radiation from both components. Model fitting to the IRAS and ISO data indicates that models with a single, central Mira-type source are more appropriate. This indicates that the radiation of the hot component is largely processed by the surrounding gas, and does not substantially affect the infrared spectrum of the symbiotic nova directly. The mean spectral energy distribution based on 1983 IRAS data differs appreciably from the ISO spectrum obtained on October 1, 1996. The observed evolution of the envelope spectrum probably reflects an increase of the density and decrease of the temperature of the dust grains near the inner boundary of the envelope, related to a decrease of the luminosity and increase of the temperature of the hot component. We estimate the total mass-loss rate, velocity of gas expansion at the outer envelope boundary, and upper limit for the mass of the central source of radiation. © *2001 MAIK "Nauka/Interperiodica".*

1. INTRODUCTION

The peculiar object HM Sge (= N Sge 1975) is presently classified as a D-type (dusty) symbiotic nova. The cool component of the binary is a Mira star; the hot component is a white dwarf, whose outburst in 1975 (by roughly 5^m in the visible) led to the discovery of the object [1]. Since that time, HM Sge has been active from the X-ray to the radio, and has been vigorously observed at all accessible wavelengths. Before the outburst, both components were submerged in the dense gas–dust envelope formed by the stellar wind from the Mira star. The high luminosity of the system is maintained by thermonuclear burning of hydrogen captured from the envelope and supplied by the stellar wind of the cool component to the white-dwarf surface. During the outburst, dust in the central region of the envelope was evaporated and its gaseous component ionized.

At visible wavelengths, the spectrum of the system resembles that of a planetary nebula, with strong emission lines dominating against the background of the weak continuum. In the infrared (IR), a strong continuum is observed, with the CO and H_2O molecular emission and distinctive silicate peaks characteristic of Mira-type oxygen stars [2, 3]. The ionized envelope gas also produces a fairly large flux at radio wavelengths. Observations with high spatial resolution have detected bipolar structure, as is typical of numerous planetary nebulae. The observed pattern of the flux variations of HM Sge is very complicated, since the Mira star's variability is superimposed on slow variations of the gas envelope and dust density associated with the variability of the luminosity and effective temperature of the hot component.

Here, we analyze the brightness and color variations of the symbiotic nova HM Sge based on our 1978–1999 photometry in the visible and IR, present a model for its dust envelope, and estimate the parameters of the stellar wind.

2. OBSERVATIONS

Photometric observations of HM Sge at visible and IR wavelengths have been made since 1978 with the 1.25-m telescope at the Crimean station of the Sternberg Astronomical Institute, as part of a program to study circumstellar dust envelopes. The stars BD $17°4103$ (for the *UBVR* bands) and BS 7488 (for the *JHKLM* bands) were chosen as photometric standards. The angular diameter of the photometer entrance aperture was approximately $12''$, and the spatial separation of the beams during modulation was $\sim30''$ in the east–west direction. The errors in the *JHKL* and *M* estimates do not exceed $0\overset{m}{.}03$ and $0\overset{m}{.}05$, respectively.

Figure 1 presents our 1978–1999 stellar magnitudes and color indices for HM Sge (circles). Figure 2 presents the mean brightness curves in the *U* and *J* filters and the variations in the (*J–K*) and (*U–B*) color indices (also circles). The variability phases are calculated for the pulsation period of the Mira star $P = 535^d$. We adopted the initial epoch $JD_0 = 2443718$, corresponding to the
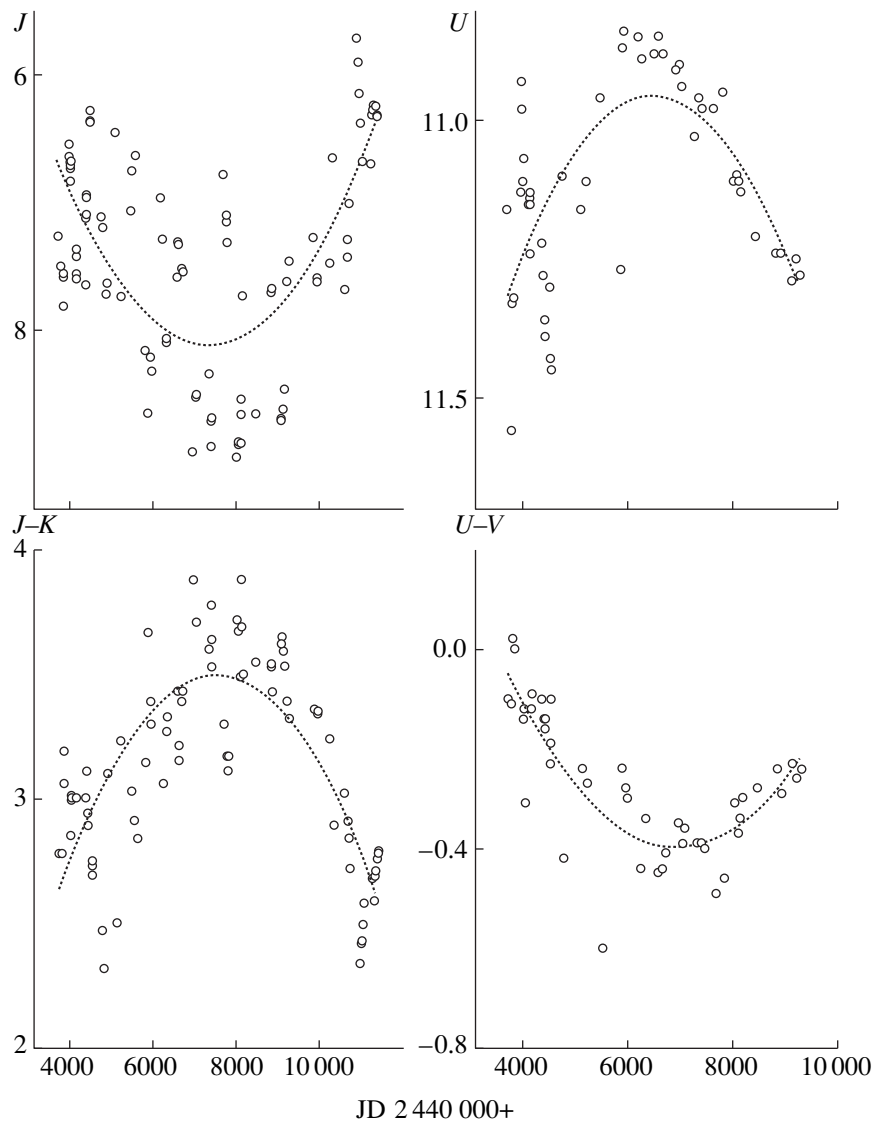
Fig. 1. Variation of the brightness and color indices of HM Sge at visible and IR wavelengths in 1978–1999 (circles). The dotted curves represent parabolic approximations to the observational data.

beginning of our observations. Our *JHKLM* photometry of HM Sge is discussed in more detail in [4].

Using the Brackett-series hydrogen emission lines at 1.5–2.3 μm, Thronson and Harvey [5] estimated the interstellar absorption of HM Sge to be $A(V) \sim 12^m$. Estimates based on the Balmer lines [6] yielded $A(V) \sim 1^m$–2^m. We adopted a value close to this latter result (corresponding to a color excess $E(B–V) \sim 0\overset{m}{.}6$).

3. BRIGHTNESS AND COLOR VARIATIONS

Figure 1 presents a parabolic fit to our observations (dashed curves). We can see that the brightness in the *J* filter (as well as in the other IR filters, *HKLM*) decreased from the beginning of the observations in 1978 until 1989, and later increased until the end of 1999. On average,

during the minimum IR brightness in 1989, a relative reddening of the system was also observed. In [4], smooth variations of the IR brightness and colors are explained by the variations of the optical depth of the dust envelope, which reached its maximum in 1989. Later, the dust envelope began to decay, and its optical depth had appreciably decreased by the end of 1999.

We can see in Fig. 1 a distinctive feature of the visible and IR brightness and color variations of HM Sge: they occur in antiphase with each other. After the outburst, the radiation of HM Sge in the visible is almost totally formed in the ionized gaseous envelope, and the observed brightness and color variability are due to variations of the envelope parameters. From 1978 until 1989, the *U* brightness increased, while the color index *U–V* decreased. This suggests that the density of the ionized envelope increased in this period. In 1989, the
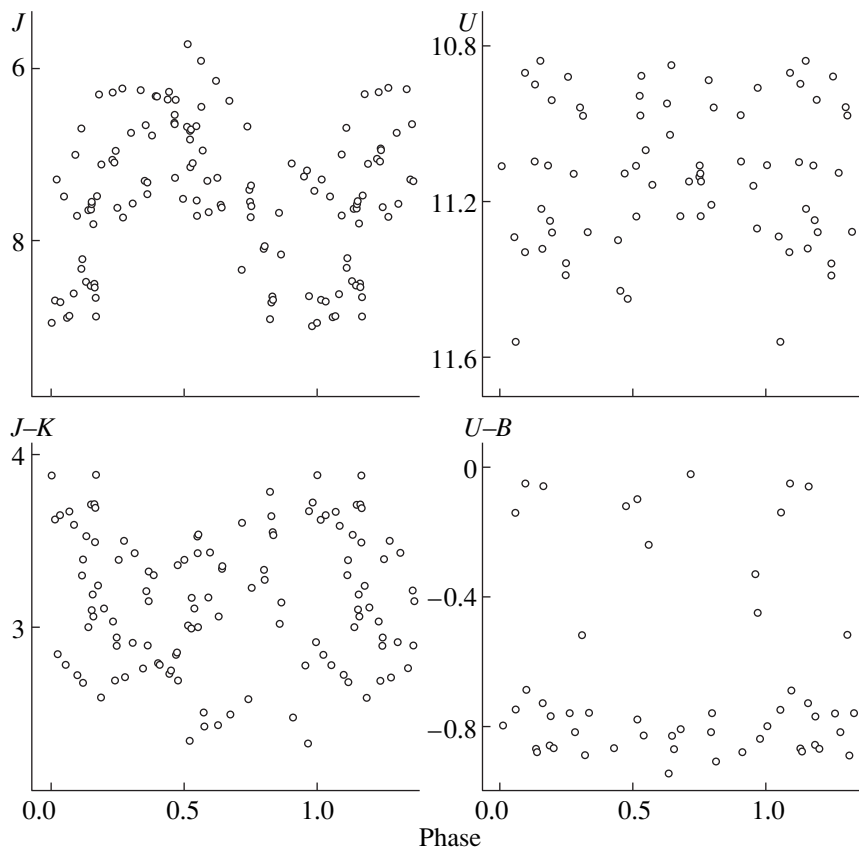
Fig. 2. Convolution of the photometric data for HM Sge obtained in 1978–1999 with the period for brightness variations of the Mira star, 535^{d}.

density reached its maximum; later, the ionized gaseous envelope apparently began to expand, resulting in a smooth decrease of the U-band flux and the U–V excess in 1989–1999 (Fig. 1). Thus, the densities of both the dust and gas components of the envelope have decreased synchronously since 1989, probably due to expansion. Note that the observed IR brightness and color variations of HM Sge are consistent with a period of 5600^{d}, which may be the orbital period of the binary.

4. THE DUST ENVELOPE OF HM Sge

The infrared excess of HM Sge detected shortly after its outburst indicates the presence of a rather dense dust envelope that reprocesses the short-wavelength radiation of the symbiotic nova. The envelope parameters have been estimated in numerous studies; however, the most interesting results based on IRAS observations were obtained in [7–10], where previous studies are also referenced.

The central problem in performing model calculations of the dust envelopes of symbiotic novae is that there exist two sources of heating with comparable luminosities but dramatically different temperatures. The presence of distinctive silicate emission peaks in the spectrum of HM Sge IR, characteristic of Mira oxy-

gen stars, provides evidence that the cool component is the main supplier of dust in the system. However, the radiation and stellar wind from the hot component undoubtedly affect the thermal balance and dynamics of the dust grains. The presence of this component, whose hard radiation is reprocessed by the surrounding gas, makes the spectrum of the dust-heating radiation difficult to specify, and violates the spherical symmetry of the envelope. This latter factor has especially unpleasant consequences for modeling, since essentially all modern procedures for calculating radiation transfer in circumstellar envelopes assume spherical symmetry.

Making envelope model calculations feasible in practice requires various simplifying assumptions. For example, Anandarao *et al.* [7] suggested that the dust envelope of HM Sge consists of several spherical layers and is heated only by the hot component. In contrast, heating of the dust grains only by the cool component at the center of symmetry of the envelope was considered in [8, 9]. Bryan and Kwok [9] justified this assumption based on the fact that, when the temperature exceeds 10^5 K, most radiation from the hot component is emitted at wavelengths below the Lyman continuum limit, and is essentially totally absorbed by the surrounding gas. In addition, the expected distance between the binary components (~10–100 AU) is much smaller

than the size of the envelope (~1 pc), so that they can be taken to be located at the center of the envelope, while the envelope itself can be assumed to be spherically symmetrical. These arguments were criticized by Yudin [10], who calculated a multi-component model for the envelope, which he took to be made up of a combination of elementary isothermic dust layers. This model was also able to describe the variations of the energy distribution in the near IR, associated with the variability of the cool component.

We have calculated models for a steady-state, spherically symmetrical, extended dust envelope for HM Sge for two extreme cases of heating: only by the cool component (Model 1) and by the combined radiation from both components, without taking into account high-energy photons absorbed by the gas (Model 2).

5. DUST ENVELOPE MODEL CALCULATIONS

To justify the basic assumptions that the envelope is in a steady-state and has spherical symmetry, we should chose an optimum spectral interval for comparing the models and observational data. The variability of the cool component is manifest in the near IR. The influence of the hot component is important mainly in the central region of the envelope, where there are high–temperature dust grains that also produce short-wavelength radiation. We expect that the effect of inhomogeneities in violating the spherical symmetry of the envelope is proportional to the ratio of their combined solid angle to that of the area of the envelope that effectively radiates at a given wavelength λ. This ratio should decrease appreciably in the transition to longer wavelengths. In the far IR ($\lambda > 60$ micron), however, the flux of HM Sge is rather low, and can be measured only with large uncertainty. In addition, the optical parameters of silicate at these wavelengths are not known sufficiently well. Therefore, we limit our model fitting to the energy distributions at middle IR wavelengths (7.7–22.7 μm), which were measured by the IRAS and ISO low-resolution spectrometers. We obtained fluxes $F(\lambda)$ via the Internet from the databases of the University of Calgary and the ISO observatory. The IRAS observations were reduced using the calibration relations from [11]. Figure 3 presents $\lambda F(\lambda)$ in erg s^{-1} cm^{-2} as a function of wavelength λ in microns (circles).

We can see from Fig. 3 that the mean spectral energy distribution for the 1983 IRAS data differs appreciably from the ISO spectrum obtained on October 1, 1996. We attribute this difference to long-term variations of the parameters of the hot component of HM Sge. According to [12], its luminosity and effective temperature during the period of the IRAS observations were $L_h = 24\,600 L_\odot$ and $T_{\text{eff},h} = 150\,000$ K, respectively, whereas extrapolation of these values from [12] to the epoch of the ISO observations yields $L_h = 9000 L_\odot$ and $T_{\text{eff},h} = 200\,000$ K. To take the effect of these variations into account, we carried out independent fitting of Models 1 and 2 using the IRAS and ISO observations.

$\lambda F(\lambda)$, 10^{-8}erg s^{-1} cm^{-2}
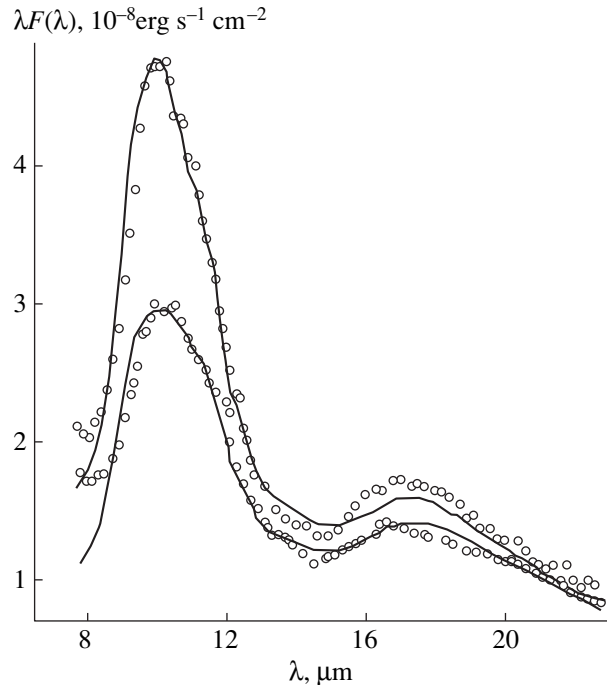
Fig. 3. Spectral energy distribution $\lambda F(\lambda)$ of HM Sge (circles) measured by the IRAS (upper curve) and ISO (lower curve) low-resolution spectrometers. The solid curves display the energy distributions for models with a single source of radiation (see model parameters in the table).

To estimate the luminosity of the cool component, we used the period–luminosity relation [13] obtained from observations of Mira oxygen stars in the Large Magellanic Cloud, $M_b = 2.88–3.00 \log P$, in spite of the fact that our adopted period for the brightness variations ($P = 535^{\text{d}}$) exceeds the longest periods for which this relation was derived. We took the absolute bolometric magnitude of the Sun to be $M_{b,\odot} = 4^m\!.75$ [14]. The effective temperature for the Mira star $T_{\text{eff},c}$ was derived from the relation $\log T_{\text{eff},c} = 3.888–0.174 \log P$ [15].

We adopted the usual assumptions for both Models 1 and 2. We assumed that the dust envelope has a sharp inner boundary a distance r_1 from the center and that the density of dust grains decreases in inverse proportion to the square of the distance up to the outer boundary of the envelope at $r_2 = 1000\, r_1$. The optical parameters of the dust grains were chosen to coincide with those of "warm" silicate [16]; their size distribution $n(a)$ was described by the model of [17] ($n(a) \propto a^{-q}$) for spherical dust grains with radii $a_{\min}$ and $a_{\max}$, with $q = 3.5$, $a_{\min} = 0.005$ micron, and $a_{\max} = 0.25$ micron. In Model 1, a blackbody with the parameters of the Mira star $L_c = 10\,600 L_\odot$ and $T_{\text{eff},c} = 2600$ K is located at the center of the envelope, while, in Model 2, the flux from the central source is equal to the sum of those from two blackbodies with the luminosities and effective temperatures in the table. This corresponds to the assumption that the

log F [erg s^{-1} cm^{-2} cm^{-1}]
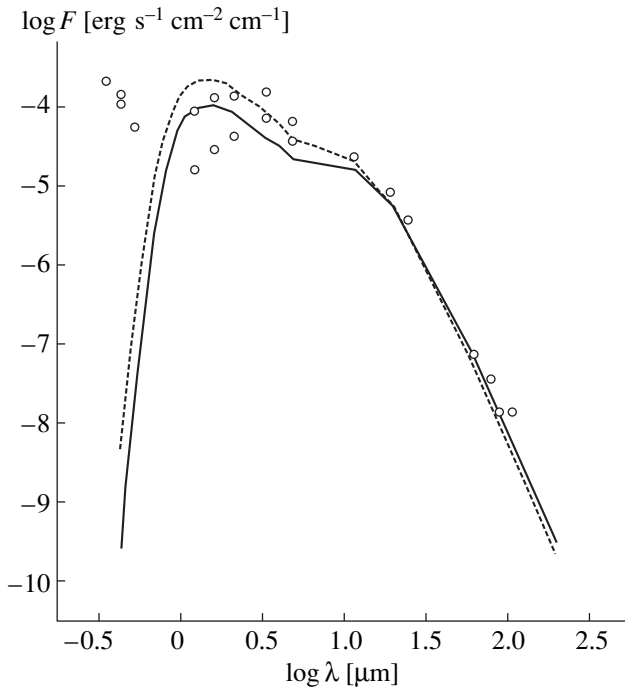
Fig. 4. Spectral energy distribution of HM Sge at 0.36–200 µm (circles). The dashed and solid curves display the distributions for single-source models fitted to the IRAS and ISO data, respectively (see text for details).

components do not eclipse each other, and are located within a sphere of radius r_1. As noted above, given the small distance between the components compared to the size of the dust envelope, we can take this condition to be approximately satisfied.

We solved for the radiation transfer in the dust envelope using the DUSTY code (version 2.0) for grids of 30 points in radius and 99 wavelength steps from 0.01 micron to 3.6 cm. The basis for this code is described in [18, 19]. The input parameters of the models were the dust temperature at the inner boundary T_1 and the optical depth of the envelope τ_V at 0.55 micron. After the model spectral energy distribution was calculated, the distance d was fit by minimizing the sum of the squared deviations between the observed and model fluxes Σ. The resulting optimum parameters for both models for the IRAS and ISO data are presented in the table.

The results indicate that Model 2 is unable to adequately describe the observed energy distributions at middle IR wavelengths. Evidence for this is provided by the table: the sums of the squared deviations Σ for Model 2 are roughly twice those for Model 1. Since the total radiation flux remains constant, an increase in the central source's luminosity results in overestimated d values that are in contradiction with previous studies of HM Sge. Taken together, these facts support the hypothesis that the short-wavelength radiation from the

hot component is essentially totally absorbed by the surrounding gas [8, 9]. Therefore, from this point on, we will concentrate primarily on Model 1.

Figure 3 presents spectral energy distributions for Model 1 (solid curves) fitted to the data for the IRAS (upper) and ISO (lower) low-resolution spectrometers. As we can see, these models are in satisfactory agreement with the observations. Figure 4 presents a comparison with the observations over a broader spectral interval. The dashed and solid curves represent the logarithm of the flux (in erg s^{-1} cm^{-2} cm^{-1}) as a function of the logarithm of the wavelength (in microns) for Model 1 fitted to the IRAS and ISO data, respectively. The circles show the logarithms of the mean fluxes for our *UBVJHKLM* photometry, and also IRAS and ISO photometry, at the maximum and minimum of the 535-day period. The results for $\lambda > 60$ micron have low reliability. Despite the fact that these fluxes were not used in the model fitting, the calculated curves are fairly close to the observations over virtually the entire IR range.

We can see from Fig. 3 that the intensity of the silicate emission peaks in HM Sge's low-resolution IR spectrum decreases with time. At the long-wavelength end of the spectrum, the IRAS and ISO fluxes are essentially the same, as are the fluxes in the far IR. This is probably due to the fact that variations in the parameters of the hot component influence the formation of dust in the central region of the envelope without affecting the bulk of its mass. In this model, these variations are manifest as an increase of the optical depth of the envelope due to an increase of the dust-grain density, which is accompanied by a decrease of the dust temperature near the inner boundary (see the table). It is evident that the presence of the hot component inhibits the condensation of dust at the typical distance for this from the Mira star. The decrease of the hot component's luminosity is accompanied by an increase of its temperature. In the process, a larger and larger fraction of the flux radiated by the hot component exceeds the Lyman continuum limit and is absorbed by the surrounding gas. Both factors facilitate dust formation in the central region of the envelope, affecting the envelope model parameters.

6. DETERMINATION OF THE STELLAR WIND PARAMETERS

To estimate the parameters of HM Sge's stellar wind, which originates under the action of the radiation pressure on dust and the subsequent transfer of momentum to the surrounding gaseous medium, we applied the DUSTY code in a gas–dynamical regime for the considered sources of radiation and derived values for the envelope optical depth. In this case, the code implements a self-consistent procedure to solve for the radiation transfer and dust motion in the stellar envelope [20]. It was assumed that the silicate density was 3 g/cm^3, and that the ratio of the gas and dust mass in the envelope was 200. Using these data, the DUSTY

Models for the HM Sge dust envelope and stellar wind obtained by fitting to IRAS and ISO observations

Parameter	IRAS		ISO	
	Model 1	Model 2	Model 1	Model 2
L_h, $L_\odot$		24 600		9000
L_c, $L_\odot$	10 600	10 600	10 600	10 600
$T_{\mathrm{eff},h}$, K		150 000		200 000
$T_{\mathrm{eff},c}$, K	2600	2600	2600	2600
T_1, K	900	900	700	900
r_1, 10^{14} cm	3.42	35.6	5.85	22.1
τ_V	10.1	6.4	12.5	8.8
d, kpc	2.0	4.4	2.6	3.7
$\dot{M}$, 10^{-5} $M_\odot$/yr	1.0	6.7	1.5	4.2
V_e, km/s	11.2	7.0	8.3	6.0
M_s, $M_\odot$	2.0	18.6	2.0	6.8
Σ, 10^{-10}	2.12	4.08	2.41	4.17

code calculates the total mass-loss rate $\dot{M}$, gas expansion velocity at the outer boundary of the envelope V_e, and an upper limit to the mass of the central radiation source M_s. The resulting stellar-wind parameters for various models are presented in the table.

We can see that Model 2 (with two radiation sources) again proves to be inadequate. In particular, the upper limits for the stellar mass are implausibly large. The estimated mass-loss rate is also unreasonably high. In contrast, Model 1 yields stellar-wind parameters that are fairly close to the results of previous studies. As could be expected, the variation of the hot component's parameters during the 13-year interval between the IRAS and ISO observations, which facilitated dust condensation in the central region of the envelope, resulted in an increase of the mass-loss rate.

Note that we have considered here only the stellar wind due to the action of radiation pressure on the dust. The intrinsic stellar wind from the hot component due to the pressure of its radiation on the gaseous component of the envelope should be added. Despite its low density, the very high velocity of this wind (~500 km/s) could result in an appreciable mass-loss rate. Therefore, the Model 1 values for $\dot{M}$ in the table should be considered lower limits to the real mass-loss rate of the symbiotic nova.

7. CONCLUSIONS

Our model fitting based on the results of IRAS and ISO observations indicates that models with only a single, central Mira-type source are preferable. This conclusion verifies the hypothesis that a large fraction of the radiation of the hot component is reprocessed by the surrounding gas, and has little direct effect on the IR spectrum of the symbiotic nova. However, the presence of the hot component affects the conditions for dust condensation in the central region of the envelope. The evolution of the envelope spectrum at middle IR wavelengths over 13 years reflects an increase of the concentration and decrease of the temperature of the dust grains near the inner envelope boundary, associated with a decrease of the luminosity and increase of the temperature of the hot component. The parameters of the dust envelope and stellar wind of HM Sge obtained using new algorithms and code for calculating the radiation transfer and dust dynamics together with independent observational data are consistent with the results of previous studies.

REFERENCES

1. O. D. Dokuchaeva, Inf. Bull. Var. Stars, No. 1189 (1976).

2. K. Davidson, R. M. Humphreys, and K. M. Merrill, Astrophys. J. **220**, 239 (1978).

3. R. C. Puetter, R. W. Russell, B. T. Soifer, and S. P. Willner, Astrophys. J. Lett. **223**, L93 (1978).

4. O. G. Taranova and V. I. Shenavrin, Pis'ma Astron. Zh. 2000 (in press) [Astron. Rep. 2000 (in press)].

5. H. A. Thronson and P. M. Harvey, Astrophys. J. **248**, 584 (1981).

6. W. P. Blair, R. E. Stencel, G. Shaviv, and W. A. Feibelman, Astron. Astrophys. **99**, 73 (1981).

7. B. G. Anandarao, A. R. Taylor, and S. R. Pottasch, Astron. Astrophys. **203**, 361 (1988).

8. S. J. Kenyon, T. Fernández-Castro, and R. E. Stencel, Astron. J. **95**, 1817 (1988).

9. G. L. Bryan and S. Kwok, Astrophys. J. **368**, 252 (1991).

10. B. F. Yudin, Astron. Zh. **71**, 900 (1994) [Astron. Rep. **38**, 801 (1994)].

11. M. Cohen, R. G. Walker, and F. C. Witteborn, Astron. J. **104**, 2030 (1992).

12. U. Murset and H. Nussbaumer, Astron. Astrophys. **282**, 586 (1994).

13. M. W. Feast, I. S. Glass, P. A. Whitelock, and R. M. Catchpole, Mon. Not. R. Astron. Soc. **241**, 375 (1989).

14. C. W. Allen, *Astrophysical Quantities* (Athlone, London, 1973; Mir, Moscow, 1977).

15. R. Álvarez and M. O. Mennessier, Astron. Astrophys. **317**, 761 (1997).

16. V. Ossenkopf, T. Henning, and J. S. Mathis, Astron. Astrophys. **261**, 567 (1992).

17. J. S. Mathis, W. Rumpl, and K. H. Nordsieck, Astrophys. J. **217**, 425 (1977).

18. Z. Ivezic and M. Elitzur, Mon. Not. R. Astron. Soc. **287**, 799 (1997).

19. Z. Ivezic and M. Elitzur, Mon. Not. R. Astron. Soc. **303**, 864 (1999).

20. Z. Ivezic and M. Elitzur, Astrophys. J. **445**, 415 (1995).

Translated by K. Maslennikov

Photometry and Polarimetry of the Classical Herbig Ae Star VV Ser

A. N. Rostopchina[1], V. P. Grinin[1, 2], D. N. Shakhovskoĭ[1]

[1]Crimean Astrophysical Observatory, National Academy of Sciences of Ukraine,
p/o Nauchnyĭ, Crimea, 334413 Ukraine
[2]St. Petersburg State University,
Universitetskaya nab. 7/9, St. Petersburg, 199164 Russia
Received December 28, 1999

Abstract—We present the results of our long-term photometric and polarimetric observations of the classical Herbig Ae star VV Ser, performed at the Crimean Astrophysical Observatory as part of a program of photometric and polarimetric monitoring of UX Ori stars. We recorded an unusually deep minimum of VV Ser ($\Delta V \approx 3^m$), with a turn of the color tracks in the V–(U–B) and V–(B–V) diagrams ("the blueing effect") observed for the first time for this star. The increase of the linear polarization during the minimum brightness was consistent with expectations for variable circumstellar extinction models, and the maximum polarization in the B band reached a record value for UX Ori stars in the deepest part of the minimum ($12.8 \pm 1.4\%$). Our results cannot be explained by models with an axially symmetrical circumstellar dust disk consisting of silicate grains. They point to the existence of a large-scale nonuniformity in the azimuthal dust distribution near VV Ser attributable to the presence of a second component or protoplanet. © *2001 MAIK "Nauka/Interperiodica".*

1. INTRODUCTION

Herbig Ae/Be stars are young stars with intermediate masses (2 to 10 $M_\odot$) evolving toward the main sequence. The main features distinguishing these stars, suggested by Herbig [1], are the presence of emission lines, especially H_α; a location close to star formation regions; and association with reflection nebulae, which are the remnants of the "parent" nebulae of young stars. Later, stars not associated with nebulae (the so-called "isolated" Herbig stars) were added to the classical Herbig stars. These isolated stars, like the classical Herbig stars, possess significant infrared (IR) radiation excesses due to circumstellar dust, and are essentially indistinguishable from the classical Herbig Ae/Be stars in all other respects [2].

The subgroup of Herbig Ae/Be stars showing high photometric activity is of special interest. These are UX Ori stars, with amplitudes for their brightness changes Δm reaching, in some cases, 4^m in the V band [3]. Simultaneous photometric and polarimetric observations (cf. [2–5] and references therein) show that one characteristic feature of this type of star is an anticorrelation between brightness changes, Δm, and changes of the linear polarization P. The general character of the dependence of P on Δm is in agreement with variable circumstellar extinction models [6], which explain the brightness decreases of these stars as the result of screening of their direct radiation by opaque fragments (clouds) of a circumstellar dust disk. During such screening, the contribution of radiation scattered by the circumstellar dust increases, explaining both the observed increase of the linear polarization and the turnover of

color tracks in color–magnitude diagrams (the so-called "blueing effect").

The blueing effect, however, has not been detected for every UX Ori star. Some do not show this effect, despite the fairly large range of brightness changes, about 1.5^m, covered by photometric measurements (e.g., [7]). In the model of [6], this means that the intensity of the scattered radiation is low, and its influence on the color indices of the combined radiation can be detected only during deep minima, which are observed very seldom. However another explanation is also possible: that variable circumstellar extinction models are not applicable to all UX Ori stars.

This paper deals with the star VV Ser, in which the blueing effect had not been detected until now. Our results show that its absence was due to the first of the two reasons above.

2. GENERAL DATA ON VV Ser

The variable star VV Ser was identified as a young Ae/Be star by Herbig [1]. It is close to a small ($0.5' \times 3'$) reflection nebula. It varies from 11.1^m to -13.3^m in the V band [8]. Photometry of VV Ser has been carried out by Fernandez [9], Shevchenko *et al.* (see the database [10]), and Eimontas and Sudzius [11]. Kardopolov *et al.* [12–15] studied the photometric behavior of VV Ser in detail, and noted the complex character of the variable's brightness changes and the absence of the blueing effect. A period of about 1000^d in the star's brightness variations was suspected in [16, 17], based on an analysis of photometric observations. The existence of this period was confirmed in [18].
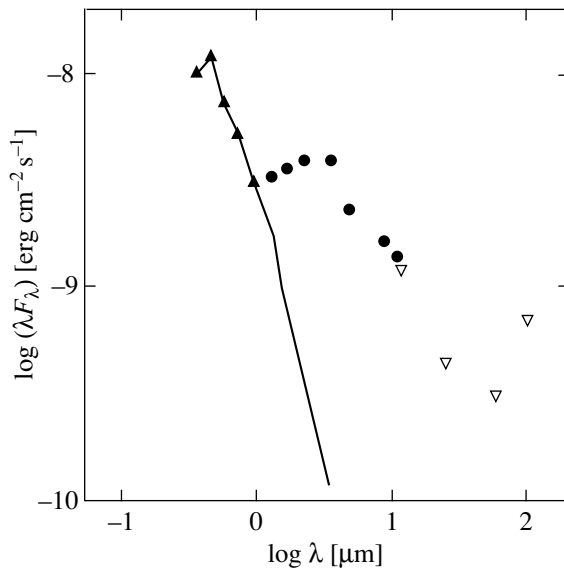
Fig. 1. Spectral energy distribution of VV Ser in its bright state. The curve shows the spectral energy distribution of an A2III star for a Kurucz model. See text for details.

Polarimetric observations of VV Ser were performed by Kardopolov *et al.* [19, 20] and Kardopolov and Rspaev [21], who noted an increase in the linear polarization during decreases in the variable's brightness. It was suggested in [20] that a polarization sign change—a 90° rotation of the polarization plane—could occur in the brightest state, not covered by the observations.

VV Ser has been observed in the IR a number of times. Both ground-based observations [22, 23] and IRAS data [24, 25] reveal an IR excess. Figure 1 presents the star's spectral energy distribution based on our *UBVRI* data for the brightest state, the IR fluxes of [26] corrected for interstellar reddening, and the IRAS data of [25]. The estimated IR excess of VV Ser corresponds to about 30% of the star's bolometric luminosity, comparable to the IR excesses of other UX Ori stars [4].

Spectroscopic studies of the star have been carried out by many authors [27–29]. VV Ser shows emission both in H_α and H_β. The star's spectral type, reproduced in many catalogs, was determined in [30] as B1–B3, based on the presence of the HeI 5876 Å line. The spectral type was found to be A2eβ in [24], where it was noted that the helium line was most probably circumstellar. Recently, this line has been found in the spectra of many young A stars [31, 32], and it may be associated with hot regions of the accretion disk.

No companion of VV Ser was found at distances exceeding 2800 AU [33] and 0″.4–8″ [34]. However, physically unrelated IR stars were discovered in its neighborhood [35] (so-called "clustering").

3. OBSERVATIONS

Observations of VV Ser at the Crimean Astrophysical Observatory were commenced in 1987 by N.Kh. Minikulov (12 nights), as part of a program of photopolarimetric monitoring of UX Ori stars, and then continued by us starting in 1993. All observations used the AZT-11 telescope ($D = 1.25$ m), equipped with a double-image chopping photometer/polarimeter [36], making it possible to conduct simultaneous photometry and polarimetry in the *UBVRI* bands. The effective wavelengths of the instrumental system are close to those of the standard Johnson photometric system. All photometric observations were reduced to the standard system. On nights with good seeing, we used a 10″ diaphragm; a 15″ diaphragm was used on other nights. The mean photometric error was 0.04^m in *U–B* and $0^m.02$ in the *V* band and other color indices.

To determine the instrumental polarization correction and the zero point, we observed standard stars each month. VV Ser is relatively faint, and we performed from 16 to 48 determinations of the Stokes parameters each night and then averaged them. The results of our observations are presented as an electronic table available at ftp://cdsarc.u-strasbg.fr/pub/cats/J.

4. RESULTS OF OBSERVATIONS

Figure 2 shows a frequency diagram of the variable's photometric activity based on the data from this study and from [9, 10, 12–15]. It is apparent that the star is mostly bright. In 1998, we recorded a unique event in the star's photometric history: as stated above, the brightness minima of VV Ser usually reach 13.3^m in the *V* band, while, on the night of JD 2 450 982, we observed the variable at $V = 14.81^m \pm 0.07^m$! On the two following nights, during the full Moon, we were not able to measure the brightness, but is was definitely fainter than 12.5^m. This limit is based on our brightness estimates for stars around VV Ser that were observed at the visibility limit on those nights, whereas VV Ser itself was invisible against the bright sky.

Figure 3 presents the light curves and curves of the polarization parameters in the *V* band, based on the electronic table noted above. It is evident that the degree of polarization in the bright state is about 2%. In the deep minimum, it reached approximately 12%, the highest linear polarization ever observed for a UX Ori star. In the minimum, the polarization position angle remained essentially unchanged.

We present color–magnitude diagrams for VV Ser in Fig. 4. We can see that the star becomes redder as it its brightness decreases, typical of most UX Ori stars. A reddening law with coefficient $dV/d(B–V) \approx 4$, slightly higher than for interstellar extinctions towards the Serpens molecular cloud ($R = 3.4$ [26]), is obeyed over a large range of the variable's brightness changes (about 2^m in the *V* band), to $V \approx 13.5^m$. Further *U–B* begins to decrease, and the star becomes bluer as it continues to
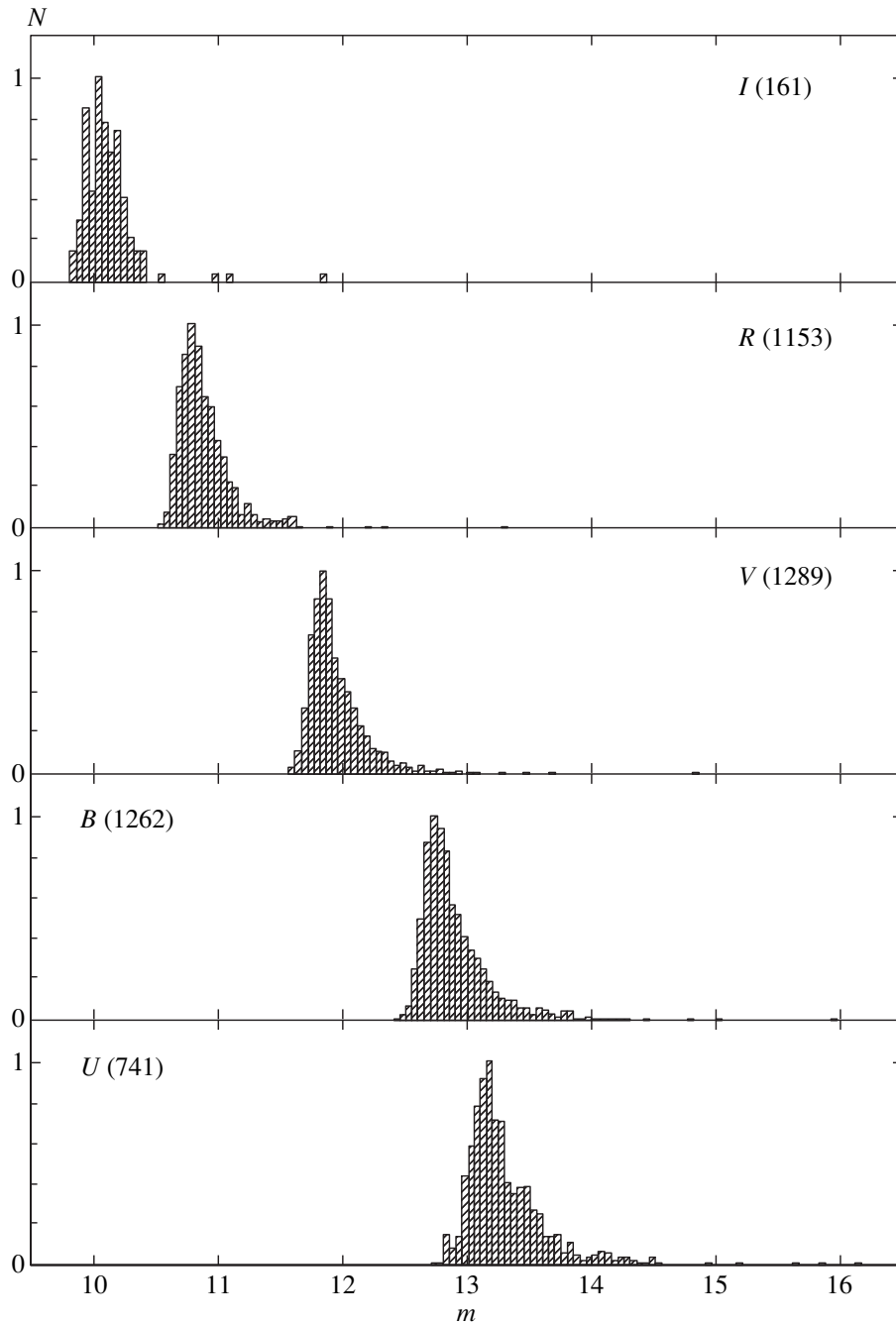
Fig. 2. Normalized histograms of the *UBVRI* photometric activity of VV Ser based on the literature (see text) and the present study. We indicate the number of observations used to plot each histogram in brackets. Each observation means one night.

fade. The *U–B* during the deepest part of the minimum observed by us is nearly the same as in the brightest state of the star. Figure 4 shows that the "blueing effect" can also definitely be seen in *B–V*. The effect is much less pronounced in the "red" color indices *V–R* and *V–I*, and is revealed only in slight deviations of the color tracks from a linear reddening law during the minimum.

The growth of the star's linear polarization, to 12% in the *V* band and 16% in the *U* band, also testifies to an increased contribution by scattered light as VV Ser

fades. We can clearly see from Fig. 5 that the increase of the polarization is nonlinear. Figure 6 shows the behavior of the Stokes parameters in the *V* band. Within the error limits, the Stokes parameters change along the same direction as the star fades, in agreement with variable circumstellar extinction models, in which the position angle of the variable component of the polarization is constant and determined by the orientation of the scattering dust disk.
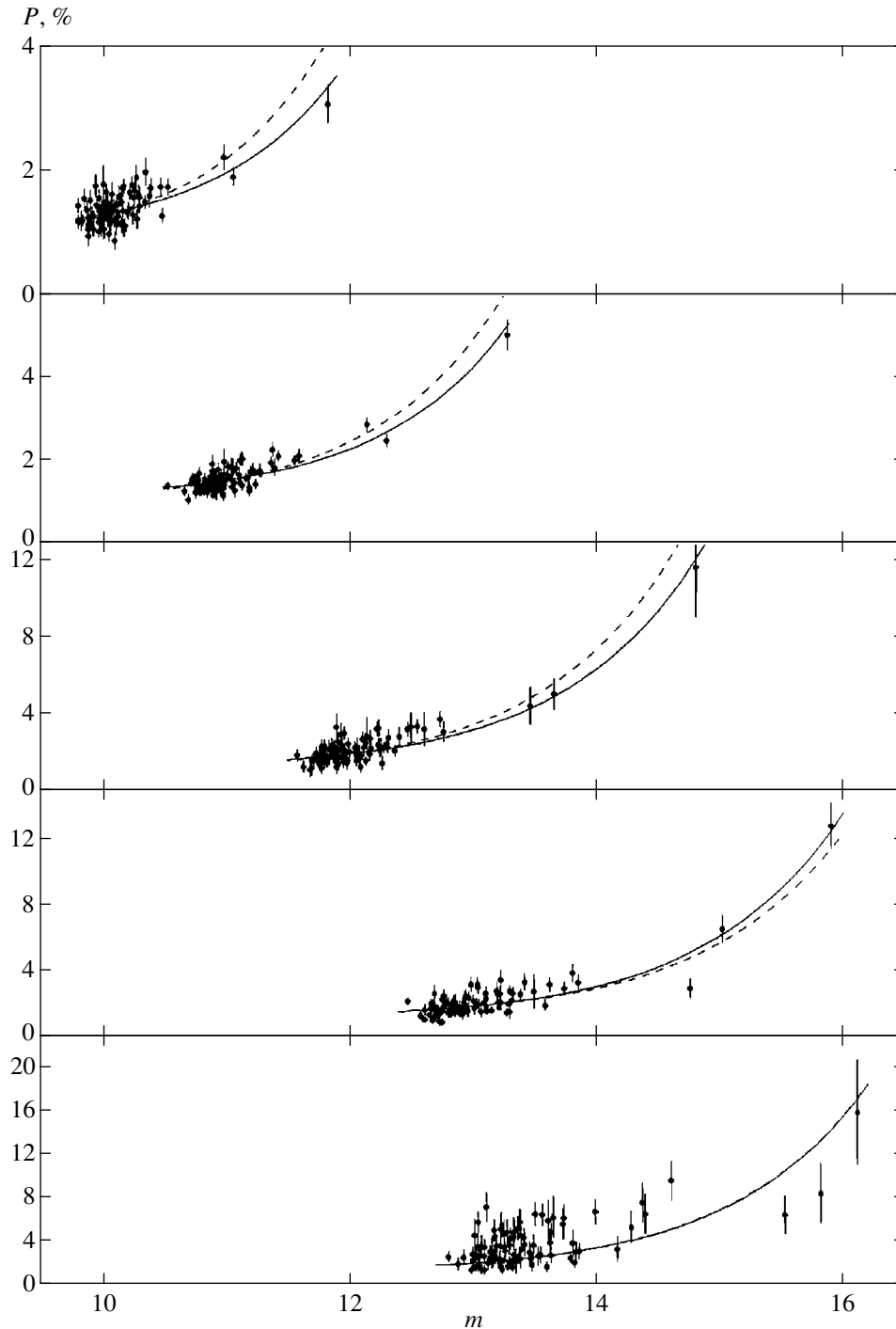
The wavelength dependences of the linear polarization for different brightness levels are presented in Fig. 7.
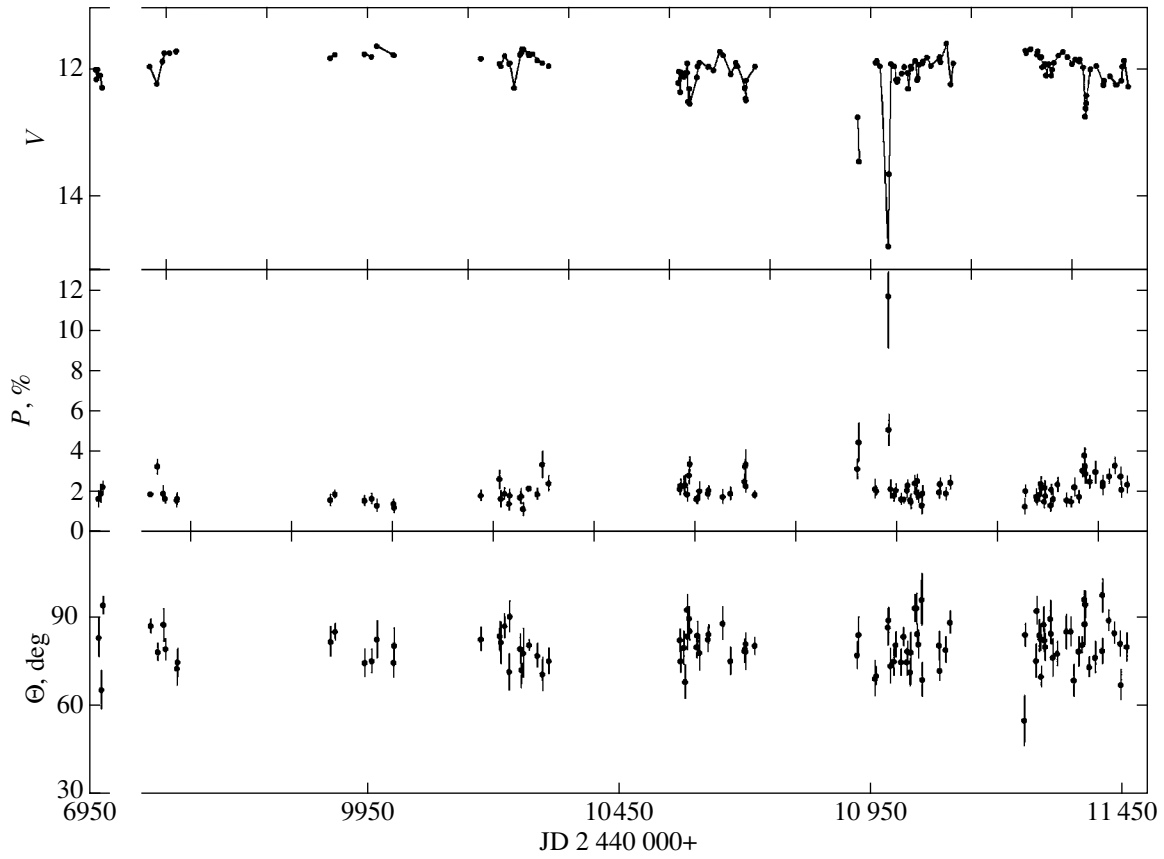
Fig. 3. Light, polarization, and polarization position angle curves for VV Ser in the *V* band, from this study.
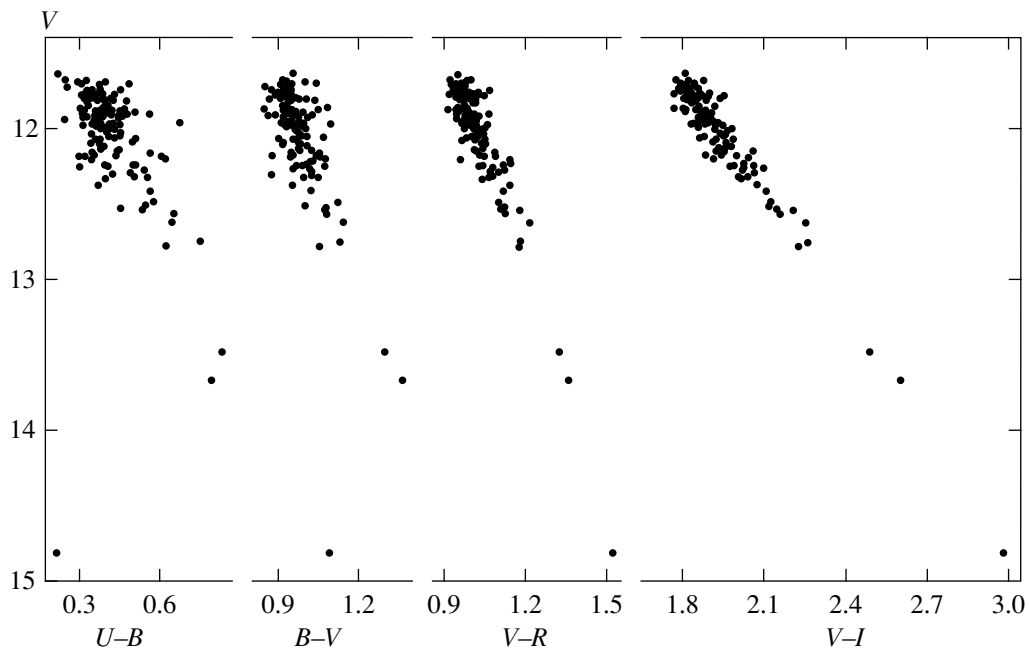

Fig. 4. Color–magnitude diagram for VV Ser, from this study.

Fig. 5. Relations between the degree of linear polarization and the brightness of VV Ser in *UBVRI*, from this study. The solid curves are theoretical relations derived from all the observations by solving Eq. (1) with weights inversely proportional to the squared error of each observation. The dashed curves are the same, but with observations at minimum brightness excluded.

They show that the polarization spectrum does not strongly change during the brightness decline. In all cases, the polarization increases towards the blue. When the brightness decreases by approximately 1^m, the growth of the polarization in the blue filters overtakes the growth in the red filters. This can be explained by the wavelength dependence of the amplitude of the brightness decrease, due to the selective extinction law in circumstellar dust clouds, so that the decrease is strongest in the blue. For this reason, the contribution of scattered light increases more quickly in the blue than at longer wavelengths.
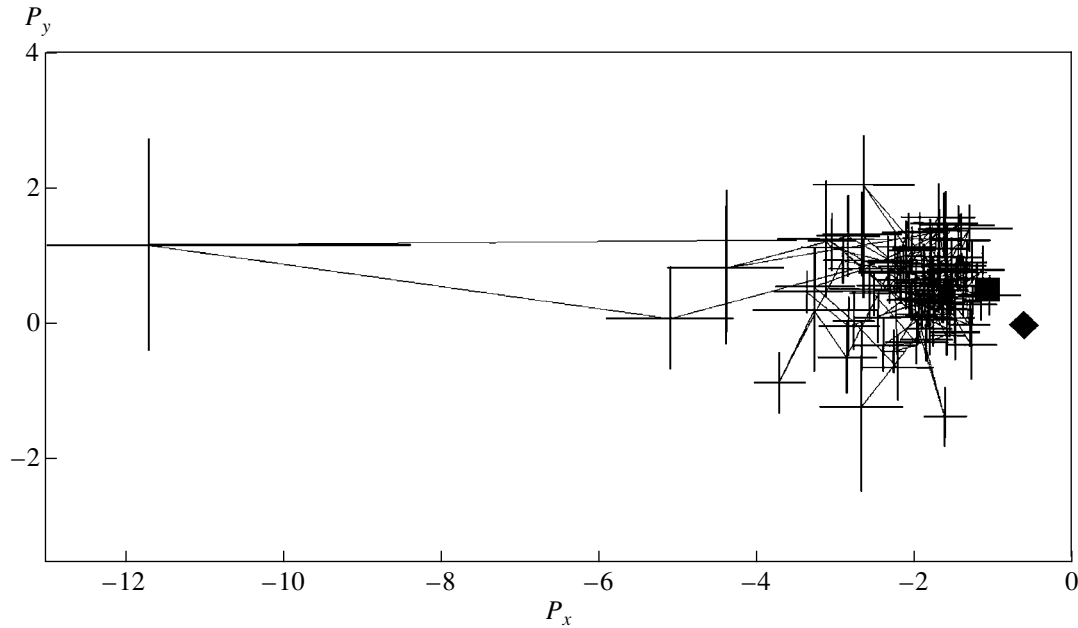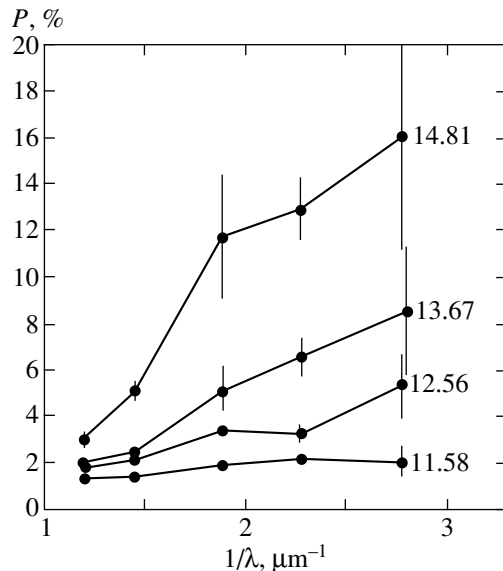
Fig. 6. Stokes parameters of the linear polarization of VV Ser in the *V* band P_x and P_y. The diamond indicates the intrinsic polarization of VV Ser in its bright state; the square indicates the interstellar polarization [derived from solution of Eq. (1)].

5. ANALYSIS AND INTERPRETATION

It is especially important that VV Ser is associated with a reflection nebula. Its size (see above) means that, when observing with 10″ or 15″ diaphragms, some of the nebular light enters the diaphragm. As a result, the contribution of the nebula to the observed radiation will differ for observations with different diaphragms and, most importantly, as the star's brightness changes. To estimate the contribution of the nebula to the observed

Fig. 7. Linear polarization spectra of VV Ser for different brightness levels.

radiation, we carried out observations of the variable with both diaphragms on several moonless nights at different brightness levels of VV Ser ($V = 11.8^m$, 12.4^m, 13.7^m). The results did not indicate differences exceeding the observational errors, for either the polarimetric or photometric measurements obtained with the two diaphragms. This means that, from the brightness maximum to ~14^m, there is no difference in brightness or polarization for VV Ser observed through the 10″ and 15″ diaphragms; i.e., the contribution of the nebula to the observed radiation remains insignificant when the star's magnitude decreases to 14^m.

5.1. Comparison with Other Results

Comparison of our photometric observations with earlier results [9, 10, 15] shows that the minimum we observed is unique, almost 1.5^m deeper than any minimum earlier observed. It is noted in [12–15] that VV Ser does not show the turnover of its color tracks in the color–magnitude diagrams that is characteristic of this type of star. Having now observed the star in a deeper minimum, we were able to reliably detect the "blueing effect" at blue wavelengths (*U–B* and *B–V*) and to find some evidence for its presence in the red. Thus, the absence of the effect in earlier observations was due to the rareness of sufficiently deep minima.

Note that the brightness minimum was very short, and lasted only a few days. Based on the shape of the minimum, the circumstellar dust cloud that crossed the line of sight was compact, with rather sharp edges. Comparison of our photometric data with observations from other studies does not show any deviations in the

Interstellar and intrinsic polarization in the bright state of VV Ser from Eq. (1)

P_{is}, %	$\sigma_{P_{is}}$, %	P.A.$_{is}$, deg	$\sigma_{P.A._{is}}$, deg	P_{in} (0), %	$\sigma_{P_{in}}$, %	P.A.$_{in}$ (0), deg	$\sigma_{P.A._{in}}$, deg
1.232	0.278	81.62	6.46	0.763	0.155	89.58	5.82
1.167	0.065	80.90	1.60	0.539	0.023	88.13	1.23
1.183	0.064	76.18	1.55	0.589	0.026	89.09	1.27
1.082	0.033	72.18	0.87	0.396	0.018	93.65	1.31
0.939	0.051	68.47	1.57	0.426	0.035	95.50	2.35

behavior of the color tracks in ranges of brightness changes that are in common. Consequently, the optical parameters of the dust grains in the various circumstellar dust clouds (including the cloud that gave rise to the deep minimum) are approximately the same.

The earlier polarization observations of VV Ser in the *BVR* bands by Kardopolov *et al.* [19, 20] and Kardopolov and Rspaev [21] are few in number, and correspond mainly to the variable's bright state. There are only four observations in minima, obtained during brightness decreases of $\Delta V \simeq 0.5^m$. Here, the observed polarization reached 4% in the *V* band and grew as the star's brightness decreased more rapidly than in our observations. The accuracy of the observations of [19–21] is not high, but we cannot exclude the possibility that this difference is real.

Kardopolov *et al.* [20] suggested two mechanisms related to the circumstellar disk and bipolar flows to explain the polarization behavior of VV Ser. They suggested that the contribution to the polarization from scattering in flows during the bright state of VV Ser exceeds the contribution from scattering in the disk; i.e., after minimum polarization, when these two components are equal, we should observe a growth of the polarization and the rotation of the polarization position angle by $\pi/2$. Our polarization observations, obtained over a larger time interval, completely cover the range of brightness changes of VV Ser, and do not show either significant changes of the polarization position angle or an increase of the degree of polarization in the maximum brightness states of the variable.

5.2. The Intrinsic Polarization of VV Ser

Our observations in the bright state of VV Ser showed no significant changes in the linear polarization over 12 years, so that the Stokes parameters of the light scattered by the circumstellar disk can be considered constant. If all the observed polarization and brightness changes of VV Ser are due exclusively to eclipses of the star by dust clouds crossing the line of sight and the contribution of other variability mechanisms is insignificant, the following simple relations will hold:

$$P_{obs}(\Delta m) = P_{is} + P_{in}(\Delta m), \qquad (1)$$

where

$$P_{in}(\Delta m) = P_{in}(0) \times 10^{0.4\Delta m}. \qquad (2)$$

Here, $P_{obs}(\Delta m)$ is the observed linear polarization of VV Ser; $P_{in}(0)$ is the intrinsic polarization during the bright state; and P_{is} is the interstellar polarization toward the variable.

If we write such equations for each observation of VV Ser, separately for each of the Stokes parameters, we will obtain a system of equations whose weighted least-squares solution will yield the interstellar polarization and intrinsic polarization in the bright state (see table). Figure 5 presents "polarization–brightness" relations based on the solution of this system of equations for each of the *UBVRI* bands (solid curves). In all five bands, these relations describe the observed changes of polarization with brightness quite well.

To evaluate the dependence of the solution obtained on the only polarization observation in a deep minimum, we solved the system of equations again without this observation (the dashed curves in Fig. 5). The new solution of system (1) is only slightly different from the solution taking the deep minimum into account. The deviation between the two solutions is smallest in the *U* band, where the photometric variability amplitude is rather high even without the deep minimum, and gradually increases toward the red. Nevertheless, even in the *R* and *I* filters, where the deviation between the two solutions is largest, we can consider it negligible.

5.3. The Interstellar Polarization of VV Ser

The position angle of the interstellar polarization of stars near VV Ser changes only slightly from star to star [37] and coincides with that for the solution of (1) for the bright state of VV Ser. Thus, the symmetry axis of the circumstellar dust disk is directed along the local interstellar magnetic field. This provides evidence for the importance of the magnetic field in the early stages of gravitational collapse that resulted in the formation of VV Ser. Similar results were found earlier for other UX Ori stars [2–5].

Note that the interstellar polarization in the direction toward VV Ser shows a clear dependence on absorption [37]. The position of VV Ser in the P–A_V diagram is in

a good agreement with the positions of other heavily absorbed stars in the same cloud. The mean degree of linear polarization for these stars, 1.1%, agrees within the errors with that for the solution of system (1).

We note also that the wavelength dependence of the interstellar polarization of VV Ser obtained from (1) is described well by the formula of Serkowski:

$$P_\lambda / P_{max} = \exp(-1.15(\ln(\lambda_{max}/\lambda))^2). \qquad (3)$$

The maximum interstellar polarization determined from observations of stars near VV Ser [37], like that determined from (1), is in the *UB* bands.

We should emphasize that the coincidence of the interstellar polarization parameters derived from two completely independent methods—from observations of surrounding stars and from the separation of the observed polarization into intrinsic and interstellar components based on the solution of system (1)—confirms the correctness of the latter method and of our conclusions based on it. Our main conclusion is that the observed variability of VV Ser's polarization and brightness are due to eclipses by circumstellar dust clouds.

We stress this here because of the recent paper by Herbst and Shevchenko [38] claiming that there is no direct observational proof for variable circumstellar extinction models in the case of UX Ori stars, and that it is preferable to use an FU Ori model to explain their Algol-like brightness decreases. We are not going to discuss FU Ori models or their applicability to UX Ori stars, since Herbst and Shevchenko [38] did not suggest any reasonable explanation for polarization effects such as those discussed here, which are among the main characteristic features of this type of star [2–4]. We note only that the synchronism of the increase of VV Ser's linear polarization and brightness, with the polarization and brightness related by (1), offers a direct demonstration of the eclipsing nature of the minima for stars of this type.

5.4. Numerical Simulation Results

A comparison of the polarimetric activity of VV Ser with that of other UX Ori stars shows considerable similarity in the behavior of the linear polarization for different stars of this class. As shown above, the observed changes of the degree of polarization of VV Ser can readily be explained in the variable circumstellar extinction model [6]. The main difference between VV Ser and other UX Ori stars is the observation of a high degree of polarization in a deep brightness minimum. We note here that the degree of linear polarization in deep minima is also quite significant (5–7%) for other stars of this type. For this reason, it was suggested in [4, 5] that the circumstellar dust disks of UX Ori stars are predominantly oriented edge-on or at a small angle to the line of sight. Subsequently, this suggestion was supported in [39–41]. In particular, the existence of a weak, but statistically significant, correlation of the

photometric variability amplitudes of UX Ori stars and related objects with their rotation rates, $v\sin i$, was indicated in [41].

On these grounds, similar to earlier studies of numerical models for the circumstellar disks of UX Ori stars (for example, [42, 43]), we consider a model with an axially symmetrical disk-like envelope observed edge-on. Our Monte-Carlo simulations [44] of multiple scattering of the stellar light by spherical grains (Mie theory) showed that the polarization observed in the deep minimum of VV Ser could be achieved only if most of the envelope particles have a large imaginary part for their index of refraction, as do graphite or metallic grains. However, this seems improbable, since the main component of circumstellar dust for most Herbig Ae/Be stars is silicate grains [45].

One possible explanation for the anomalously high polarization in the brightness minimum of VV Ser retaining a "standard" mixture of silicate and graphite grains (as is usually assumed for the interstellar medium) is that the scattering envelope is not axially symmetric. Our calculations show that the observed polarization and intensity of the scattered light determined from the "blueing effect" can result from scattering in the denser part of a non-axially symmetric disk-like dust envelope (for simplicity, we considered scattering by a spherical cloud of silicate grains 3–4 times further from the star than the radius of the cloud). Our Monte-Carlo simulation used a modified routine from [44] for the case of spherical grains. We chose the size of the grains to achieve agreement between the theoretical and observed wavelength dependence of the interstellar extinction, derived from the slope of the upper part of the tracks in the color–magnitude diagrams (Fig. 3). The cloud grain sizes derived from this simulation are similar to those found earlier for other UX Ori stars [42, 43].

6. CONCLUSIONS

The variable star VV Ser is the second (after RR Tau) classical Herbig Ae/Be star we have studied. In observations covering six observing seasons, we recorded the deepest brightness minimum in the entire history of photometric studies of VV Ser. In this minimum, the star was 1.5^m fainter than the faintest state observed before. It appears that VV Ser, like other UX Ori stars, shows color-track turnovers during deep brightness minima, attributable to an increase of the contribution of light scattered by the circumstellar dust. The variable's brightness decrease was accompanied by a growth in the degree of polarization in a way that was consistent with variable circumstellar extinction models.

During the minimum, we observed a record linear polarization (about 12% in the *V* band), which cannot be explained in models with an axially symmetrical dust disk using reasonable assumptions about the composition of the circumstellar grains. Our analysis indicates that the most probable reason for the high polarization is that the

circumstellar dust disk scattering the stellar light is non-uniform in azimuth. This disk structure could be the result of perturbations from a companion in a binary system or a massive protoplanet. This explanation seems rather plausible, since the light curve of VV Ser exhibits a low-amplitude wave with a 1000^d period, which could naturally be attributed to periodic perturbation of the circumstellar disk by the second component. In this connection, spectroscopic observations aimed at detecting periodic changes in the star's radial velocity would be of interest, and could make it possible to estimate the mass of the second component of the system.

ACKNOWLEDGMENTS

REFERENCES

1. G. H. Herbig, Astrophys. J., Suppl. Ser. **4**, 337 (1960).
2. V. P. Grinin, N. N. Kiselev, and N. Kh. Minikulov, Pis'ma Astron. Zh. **15**, 1028 (1989) [Sov. Astron. Lett. **15**, 448 (1989)].
3. A. N. Rostopchina, V. P. Grinin, A. Okazaki, *et al.*, Astron. Astrophys. **327**, 145 (1997).
4. V. P. Grinin, N. N. Kisilev, N. Kh. Minikhulov, *et al.*, Astrophys. Space Sci. **186**, 283 (1991).
5. V. P. Grinin, Astron. Astrophys. Trans. **3**, 17 (1992).
6. V. P. Grinin, Pis'ma Astron. Zh. **14**, 65 (1988) [Sov. Astron. Lett. **14**, 27 (1988)].
7. E. A. Bibo and P. S. Thé, Astron. Astrophys., Suppl. Ser. **89**, 319 (1991).
8. G. H. Herbig and K. R. Bell, Lick Obs. Bull., No. 1111 (1988).
9. M. Fernández, Astron. Astrophys., Suppl. Ser. **113**, 473 (1995).
10. W. Herbst, D. K. Herbst, and E. A. Grossman, Astron. J. **108**, 1906 (1994).
11. A. Eimontas and J. Sudzius, Baltic Astron. **7**, 407 (1998).
12. V. I. Kardopolov, G. K. Filip'ev, and V. P. Kuleshov, Perem. Zvezdy **21**, 682 (1982).
13. V. I. Kardopolov and G. K. Filip'ev, Perem. Zvezdy **22**, 103 (1985).
14. V. I. Kardopolov and G. K. Filip'ev, Perem. Zvezdy **22**, 153 (1985).
15. V. I. Kardopolov and G. K. Filip'ev, Astron. Zh. **65**, 951 (1988) [Sov. Astron. **32**, 498 (1988)].
16. V. S. Shevchenko, K. N. Grankin, M. A. Ibragimov, *et al.*, Astrophys. Space Sci. **202**, 121 (1993).
17. V. S. Shevchenko, K. N. Grankin, M. A. Ibragimov, *et al.*, Astrophys. Space Sci. **202**, 137 (1993).
18. D. N. Shakhovskoĭ, V. P. Grinin, and A. N. Rostopchina, Pis'ma Astron. Zh. 2001 (in press).
19. V. I. Kardopolov, L. A. Pavlova, and F. K. Rspaev, Astron. Tsirk., No. 1452, 1 (1986).
20. V. I. Kardopolov, L. A. Pavlova, and F. K. Rspaev, Astron. Zh. **68**, 565 (1991) [Sov. Astron. **35**, 278 (1991)].
21. V. I. Kardopolov and F. K. Rspaev, Astron. Tsirk., No. 1544, 15 (1990).
22. I. S. Glass and M. V. Penston, Mon. Not. R. Astron. Soc. **167**, 237 (1974).
23. C. Chavarría-K, E. de Lara, U. Finkenzeller, *et al.*, Astron. Astrophys. **197**, 151 (1988).
24. C. Y. Zhang, R. J. Laureijs, F. O. Clark, and P. R. Wesselius, Astron. Astrophys. **199**, 170 (1988).
25. D. A. Weintraub, Astrophys. J., Suppl. Ser. **74**, 575 (1990).
26. E. de Lara and C. Chavarría-K, Mex. Astron. Astrofiz. **18**, 180 (1989).
27. L. A. Hillenbrand, S. E. Strom, F. J. Vrba, and J. Keene, Astrophys. J. **397**, 613 (1992).
28. B. Reipurth, A. Pedrosa, and M. T. V. T. Lago, Astron. Astrophys., Suppl. Ser. **120**, 229 (1996).
29. C. A. Grady, M. R. Pérez, A. Talavera, *et al.*, Astron. Astrophys., Suppl. Ser. **120**, 157 (1996).
30. U. Finkenzeller and R. Mundt, Astron. Astrophys., Suppl. Ser. **55**, 109 (1984).
31. C. Catala, T. Böhm, J.-F. Donati, and M. Semel, Astron. Astrophys. **278**, 187 (1993).
32. O. V. Kozlova, V. P. Grinin, and A. N. Rostopchina, Astron. Astrophys. Trans. **8**, 249 (1995).
33. C. Leinert, A. Richichi, and M. Haas, Astron. Astrophys. **318**, 472 (1997).
34. N. Pirzkal, E. J. Spillar, and H. M. Dyck, Astrophys. J. **481**, 392 (1997).
35. L. Testi, F. Palla, and A. Natta, Astron. Astrophys. **342**, 515 (1999).
36. V. Piirola, Ann. Acad. Sci. Fenn., Ser. A6, No. 418, 61 (1975).
37. A. N. Rostopchina and D. N. Shakhovskoĭ, Astrofizika **43**, 3 (2000).
38. W. Herbst and V. S. Shevchenko, Astron. J. **116**, 1419 (1998).
39. V. P. Grinin and A. N. Rostopchina, Astron. Zh. **73**, 194 (1996) [Astron. Rep. **40**, 171 (1996)].
40. A. Natta, V. P. Grinin, V. Mannings, and H. Ungerehts, Astrophys. J. **491**, 885 (1997).
41. V. P. Grinin and O. V. Kozlova, Astrofizika 2000 (in press).
42. N. V. Voshchinnikov and V. P. Grinin, Astrofizika **34**, 181 (1991).
43. N. A. Krivova and V. B. Il'in, Pis'ma Astron. Zh. **23**, 908 (1997) [Astron. Lett. **23**, 791 (1997)].
44. N. V. Voshchinnikov and V. V. Karjukin, Astron. Astrophys. **288**, 883 (1994).
45. D. H. Wooden, Publ. Astron. Soc. Pac. **62**, 138 (1994).

Translated by N. Samus'

Numerical Simulation of a Solar Flare Produced by the Emergence of New Magnetic Flux

A. I. Podgornyĭ[1] and I. M. Podgornyĭ[2]

[1]Lebedev Institute of Physics, Leninskiĭ pr. 53, Moscow, 117924 Russia
[2]Institute of Astronomy, Pyatnitskaya ul. 48, Moscow, 109017 Russia
Received January 13, 2000

Abstract—A scenario for the production of a current sheet above an active region during the emergence of new magnetic flux is considered. The formation of a current sheet is demonstrated via a numerical solution of a system of MHD equations with dissipative terms. The flare energy is stored in the magnetic field of the current sheet. The decay of the current sheet can account for a number of solar-flare phenomena, including the observed divergence of H_α ribbons. © 2001 MAIK "Nauka/Interperiodica".

1. INTRODUCTION

In our previous studies [1–4], we showed that, if a singular line of the magnetic field is present in an active region, virtually any photospheric perturbation results in the formation of a current sheet near this region. Depending on where perturbations arise under the singular line, the current sheet can be parallel to the photospheric surface or inclined at a considerable angle to it. As it evolves, the current sheet loses mass and becomes unstable [5]. During the decay of the sheet, the energy stored in its magnetic field is transformed into heat in a flare-like fashion. Some of the energy stored in the sheet magnetic field is transformed into the kinetic energy of the plasma accelerated along the sheet by magnetic tension. In this case, the flow of accelerated plasma is expelled from the sheet beyond the corona; i.e., a transient is ejected. The energy of the transient is often comparable to the energy of the flare. The flare model of [4, 6], based on numerical simulations of the energy stored in a current sheet and its subsequence rapid release, can explain many of the main observational effects associated with flares: the generation of longitudinal currents and acceleration of charged particles in them, leading to H_α emission and radio emission; the acceleration of particles to high energies along the neutral line; the appearance of post-flare loops due to local chromospheric evaporation under the action of infalling electrons, etc. A necessary condition for these processes is the existence of a singular line of the magnetic field in an active region.

At the same time, for a number of years, various authors [7–11] have emphasized that frequently new magnetic flux emerges just before a flare. At the same time, the old field does not necessarily have a complicated configuration, suggesting the possible existence of a singular line in it. In such cases, it is tempting to explain flares as a result of interactions between new and old fields with opposite directions, with the formation of a current sheet. One simple case when this situation comes about is when two old and two new sunspots lie in a line and their magnetic fluxes are opposite. With this sunspot arrangement, the field dynamics during the emergence of new flux can readily be traced in the vertical plane passing through the sunspots. We can consider the development of similar events in a two-dimensional approximation with a high degree of certainty.

The main problems encountered in numerical solutions of MHD equations in restricted computation domains have to do with correct specification of the boundary conditions. When calculating any physical process inside a region, perturbations arrive at the boundaries, and the boundary conditions at each subsequent time step must be modified. The PERESVET software we used automatically modifies the boundary conditions to take into account the changes introduced by moderate perturbations. The boundary conditions are corrected at each time step via solution of linearized MHD equations along characteristics [12]. However, after some time, the emerging new magnetic flux leads to rather strong perturbations at the boundaries, and the method of characteristics becomes inadequate in long calculations. Therefore, it is necessary to set simpler boundary conditions that approximately reflect the real processes. Such conditions might be the constancy of quantities or their derivatives along the normal to the boundary. In long calculations, errors accumulate due to the inadequacy of these conditions to describe the physical situation. The gradients at the boundaries become large, and further computation becomes meaningless. Thus, the assignment of boundary conditions imposes restrictions, sometimes rather rigid ones, on the duration of computations such that the conditions at the boundaries of the computation region adequately describe the actual physical processes involved. These restrictions would be absent if the equations could be

solved in very large computation domains using very powerful computers.

2. THE EQUATIONS AND METHODS USED

We numerically solved a system of two-dimensional MHD equations with dissipative terms in a region of compressible plasma with size L. The equations were solved in dimensionless form. We took the size L to be unity, so that the solution domain was $0 \le x \le 1, 0 \le y \le 1$. The dimensionless MHD equations are

$$\frac{\partial \mathbf{B}}{\partial t} = \mathrm{curl}(\mathbf{V} \times \mathbf{B}) - \frac{1}{\mathrm{Re}_m}\mathrm{curl}\left(\frac{\sigma_0}{\sigma}\mathrm{curl}\mathbf{B}\right), \qquad (1)$$

$$\frac{\partial \rho}{\partial t} = -\mathrm{div}(\mathbf{V}\rho), \qquad (2)$$

$$\frac{\partial \mathbf{V}}{\partial t} = -(\mathbf{V}, \nabla)\mathbf{V} - \frac{\beta_0}{2\rho}\nabla(\rho T)$$
$$\qquad\qquad (3)$$
$$-\frac{1}{\rho}(\mathbf{B} \times \mathrm{curl}\mathbf{B}) + \frac{1}{\mathrm{Re}\rho}\Delta\mathbf{V} + G_g\mathbf{G},$$

$$\frac{\partial T}{\partial t} = -(\mathbf{V}, \nabla)T - (\gamma - 1)T\,\mathrm{div}\mathbf{V}$$

$$+ (\gamma - 1)\frac{2\sigma_0}{\mathrm{Re}_m\sigma\beta_0\rho}(\mathrm{curl}\mathbf{B})^2 \qquad (4)$$

$$- (\gamma - 1)G_qL'(T)\rho + \frac{\gamma - 1}{\Pi\rho}\mathrm{div}\left(\frac{\kappa}{\kappa_0}\nabla T\right).$$

For the unit of the field, we adopted the mean field B_0 at the photosphere in the active region. For the units of plasma density and temperature, we adopted the initial plasma density ρ_0 and initial temperature T_0 in the corona. We adopted the Alfvén velocity $V_A = B_0/(4\pi\rho_0)^{1/2}$ for the unit of velocity, the Alfvén time $t_A = L/V_A$ for the unit of time, and $B_0^2/4\pi$ for the unit of energy density. The unit of current density was $j = cB_0/4\pi L_0$. The dimensionless values of the kinetic energy density, magnetic-field energy, and plasma pressure are $\rho V^2/2$, $B^2/2$, and $\beta\rho T/2$, respectively. All the computation results are presented in these dimensionless units.

We adopt the following notation for the dimensionless parameters: $\mathrm{Re}_m = VL/\nu_{m0}$ is the magnetic Reynolds number, $\nu_{m0} = c^2/4\pi\sigma_0$ is the magnetic viscosity for conductivity σ_0 at temperature T_0, σ is the conductivity, $\sigma/\sigma_0 = T^{3/2}$, $\beta_0 = 4\pi n_0 kT_0/B_0^2$ ($n_0 = \rho_0/m_i$, m_i is the mass of an ion), $\mathrm{Re} = L_0V_0/\eta$ is the Reynolds number, η is the viscosity, $G_q = L(T_0)\rho_0 t_0/T_0$, $L(T)$ is the radiation function for ionization equilibrium in the solar corona [13], $L'(T) = L(T)/L(T_0)$ is the dimensionless radiation function, $\Pi = \rho_0 L_0 V_0/\kappa_0$ is the Peclet number, κ_0 is the thermal conductivity at temperature T_0, κ is the thermal

conductivity $\kappa/\kappa_0 = T^{5/2}$, $G_g\mathbf{G}$ is the dimensionless gravitational acceleration, which did not play a significant role in the calculations, and γ is the adiabatic index.

In the computations, we took into account anisotropy of the thermal conductivity in the magnetic field. In these cases, the last term in Eq. (4) becomes

$$\frac{\gamma - 1}{\rho}\mathrm{div}\left(\mathbf{e}_{\|}\frac{\kappa}{\Pi\kappa_0}(\mathbf{e}_{\|}, \nabla T)\right.$$

$$\left. + \mathbf{e}_{\perp 1}\kappa_{\perp dl}(\mathbf{e}_{\perp 1}, \nabla T) + \mathbf{e}_{\perp 2}\kappa_{\perp dl}(\mathbf{e}_{\perp 2}, \nabla T)\right),$$

where $\mathbf{e}_{\|}$, $\mathbf{e}_{\perp 1}$, and $\mathbf{e}_{\perp 2}$ are unit orthogonal vectors parallel and perpendicular to the magnetic field, $\kappa_{\perp dl} = \dfrac{(\kappa\kappa_0^{-1}\Pi^{-1})(\kappa_B\kappa_{0B}^{-1}\Pi_B^{-1})}{(\kappa\kappa_0^{-1}\Pi^{-1}) + (\kappa_B\kappa_{0B}^{-1}\Pi_B^{-1})}$ is the dimensionless thermal conductivity perpendicular to the magnetic field, and $\Pi_B = \rho_0 L_0 V_0/\kappa_{0B}$ is the Peclet number for thermal conductivity across a strong magnetic field (when the Larmor radius is much smaller than the mean free path). This thermal conductivity is denoted κ_B, and κ_{0B} is its value at temperature T_0, density ρ_0, and magnetic field B_0; $\kappa_B/\kappa_{0B} = \rho^2 B^{-2}T^{-1/2}$.

According to the principle of restricted modeling, we must have $\mathrm{Re}_m \gg 1$ [14]. In the calculations, Re_m was taken to be 2×10^6; however, the actual value of Re_m was determined by the spatial step size, and was ~100. All the results were obtained using a 121×121 computation grid. As in the corona, $\beta_0 \ll 1$; we chose $\beta_0 = 10^{-6}$. The viscosity term does not considerably affect the results, but is important to increase the stability of the solutions. The Peclet number along the magnetic field $\Pi = 1$, and across the field $\Pi_B = 10^2$. We used the PERESVET code [1–4] to obtain the solution. The finite-difference scheme used to approximate the MHD equations was absolutely implicit; this rendered it very stable. The scheme was solved iteratively.

During the entire computation time, the magnetic-field component normal to the boundary was found from the condition $\mathrm{div}B = 0$. Initially, throughout the boundary, except for at $Y = 0$, the magnetic-field components parallel to the boundary, the plasma density, and all the velocity components were found from the condition of free escape, using the method of characteristics. Invariants corresponding to outgoing characteristics were found by solving the equations on the characteristics, and invariants corresponding to characteristics coming into the region were taken from the previous step. After the plasma reaches the boundaries, the large gradients near the boundaries make it impossible to use the method of characteristics; therefore, for all these quantities, we imposed the condition of zero normal derivative. We fixed the boundary temperature; i.e., the normal derivative of the temperature was set to zero.
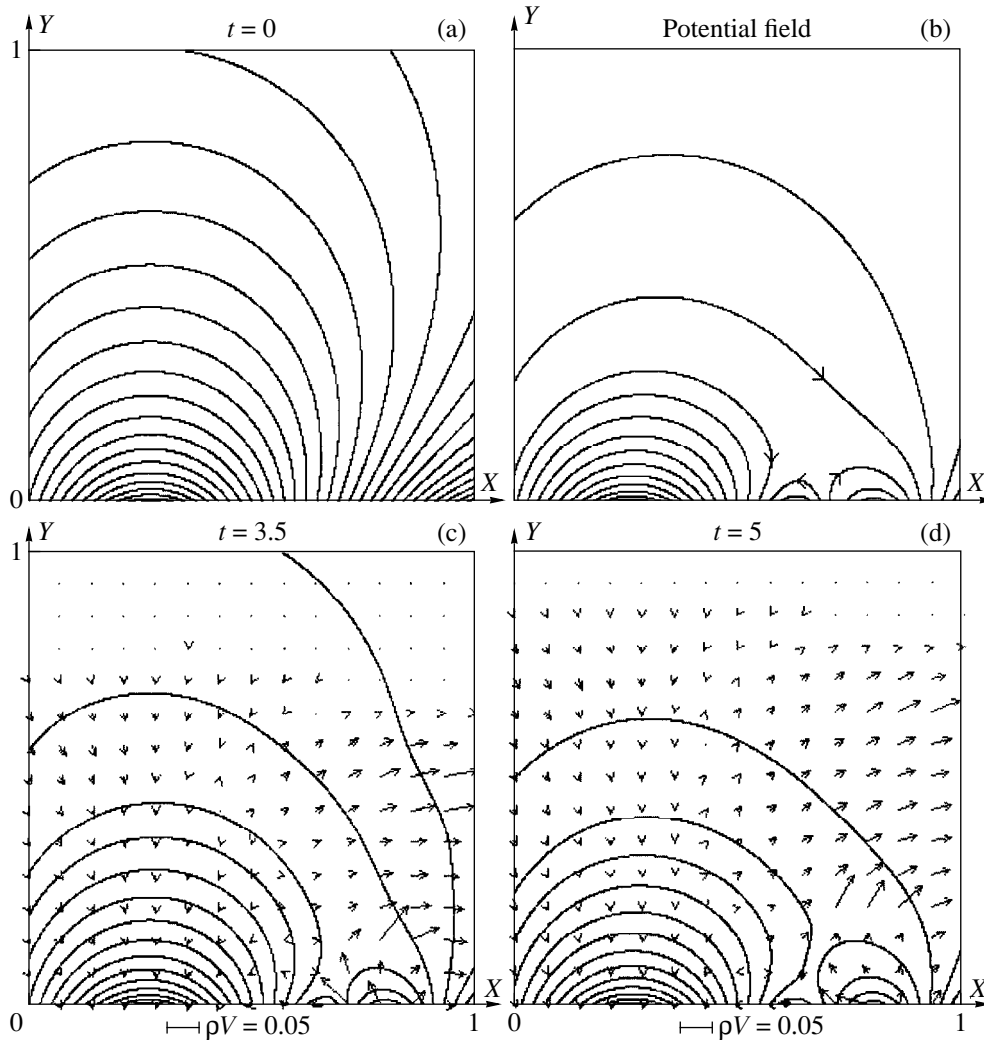
Fig. 1. (a) Lines of the initial magnetic field; (b) the potential magnetic field of four dipoles; lines of the magnetic field and of the flux vector during the emergence of new flux for times (c) 3.5 and (d) 5.

3. RESULTS

The flare development simulated here consists of the following. At the initial time $t = 0$, the active region consists of two sunspots with opposite polarity. They are approximated by two vertical dipoles located under the photosphere: $\mu_1 = 0.25$, $X_1 = 0.1$, $Y_1 = -0.5$ and $\mu_2 = -0.25$, $X_2 = 0.45$, $Y_2 = -0.5$. The positive dipole moment corresponds to the sunspot with northern polarity. Figure 1a shows the magnetic lines in the computation domain for these sunspots. At $t = 0$, the magnetic moments of two new dipoles, located beneath the photosphere at $X_3 = 0.78$, $Y_3 = -0.2$ and $X_4 = 0.85$, $Y_4 = -0.2$, begin to grow. By $t_r = 10$, their magnetic moments increase from zero to $\mu_3 = 0.25$ and $\mu_4 = -0.25$.

In the absence of plasma in the computation domain ($\rho = 0$), the resulting (vacuum) magnetic field after the maximum values of the magnetic moments μ_3 and μ_4 are reached is shown in Fig. 1b. The arrows show the field direction. The field is potential, and contains a singular point ($B = 0$).

If there is plasma in the computation domain, as in the corona, the field configuration dramatically changes as the dipole moments μ_3 and μ_4 slowly increase. The magnetic flux emerging from beneath the photosphere moves upward together with the plasma frozen in it. The perturbation introduced by this flux propagates across the computation domain at the Alfvén velocity. We can see in Fig. 1c that, 3.5 Alfvén timescales after the beginning of the increase of the magnetic fields of μ_3 and μ_4, the plasma in the entire active region has started moving. The velocity perturbations are everywhere perpendicular to the magnetic-field lines; this reflects the MHD character of the perturbations. Simultaneous with the emergence of the new flux, a boundary layer forms between the oppositely directed magnetic lines of the new and old fluxes.
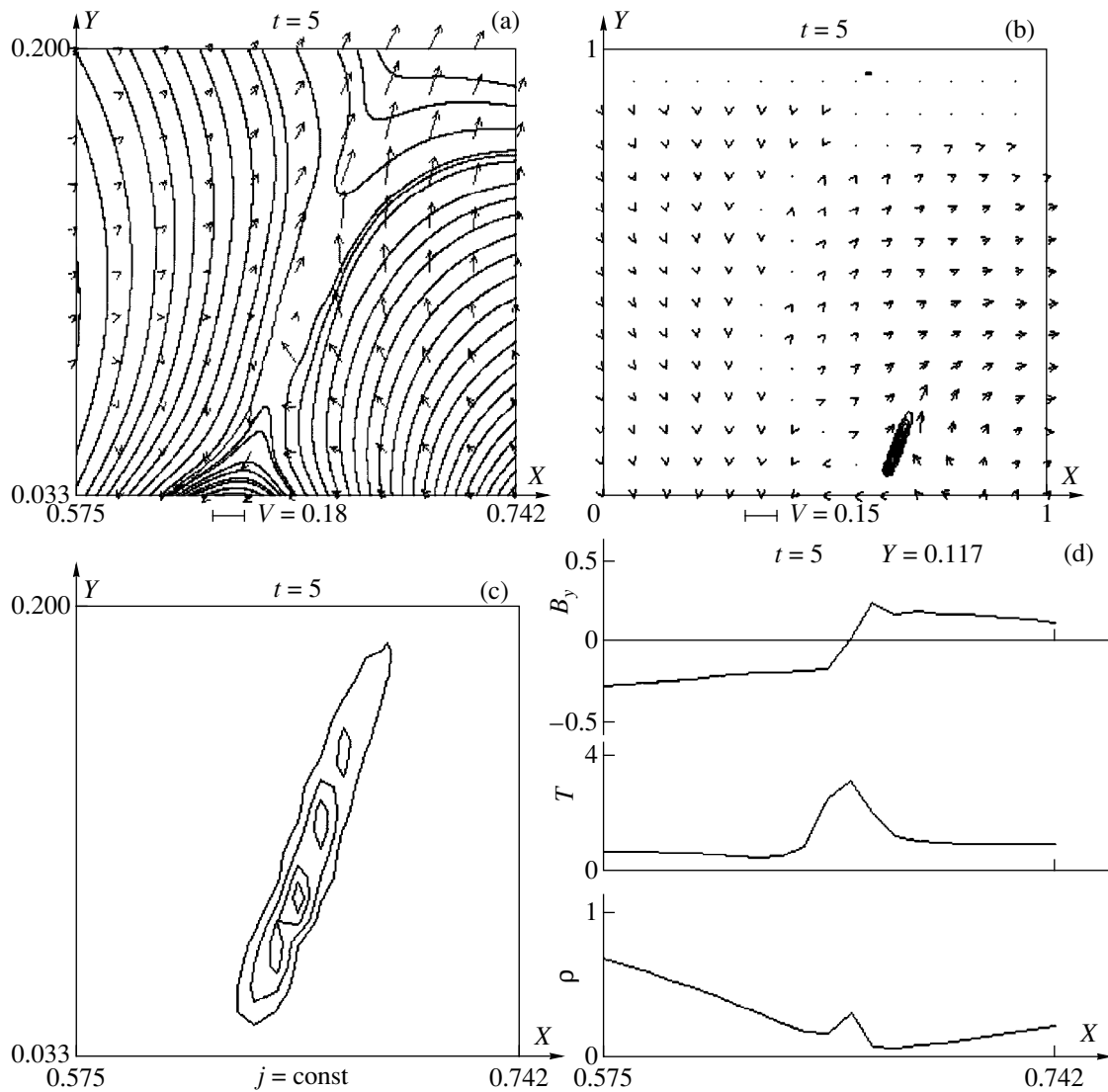
Fig. 2. (a) Lines of the magnetic field and of the velocity vector in a current sheet; levels of equal current density in an active region on (b) normal and (c) extended scales; (d) distributions of the longitudinal component of the magnetic field, temperature, and plasma density across the sheet.

The boundary layer is a current sheet of finite thickness. The high plasma conductivity ($\mathrm{Re}_m \gg 1$) does not allow the reconnection of oppositely directed magnetic lines to proceed rapidly. At this stage, the flow in the sheet makes it stable. Figure 1d presents lines of the magnetic field and plasma-flow vector ρV in the active region. The plasma flows into the sheet mainly through its left-hand boundary, and flows out along the sheet mainly upward, in the direction of the magnetic-tension forces. Rapid downward outflow is impeded by the strong magnetic field in the photosphere. This flow pattern is more clearly visible in Fig. 2a, which shows scaled-up field lines and the distribution of plasma-velocity vectors. Levels of equal current density in the computation domain are presented in Fig. 2b, and in more detail, on a larger scale, in Fig. 2c.

It follows from these data that the field configuration of the current sheet formed by the emergence of new magnetic flux is virtually the same as that for a sheet formed by the focusing of small photospheric perturbations in the vicinity of a singular line (or in a plane, of a singular point) [15]. The main feature of the configuration is the magnetic-tension force, which pushes plasma upward along the sheet. The normal component of the magnetic field inside the sheet is a factor of 30–35 smaller than the field strength at the sheet boundary. The length of the sheet exceeds its width by a factor of 10. Here, the sheet width is determined by the numerical, not magnetic, viscosity, $\nu_{m\text{-num}}$, for which the numerical Reynolds number, corresponding to the Alfvén velocity, $\mathrm{Re}_{m\text{-num}} = L_0 V_A / \nu_{m\text{-num}} = (h/L)(V/V_A) \sim 10^{-2}$. Here, h is the spatial integration step. The distri-
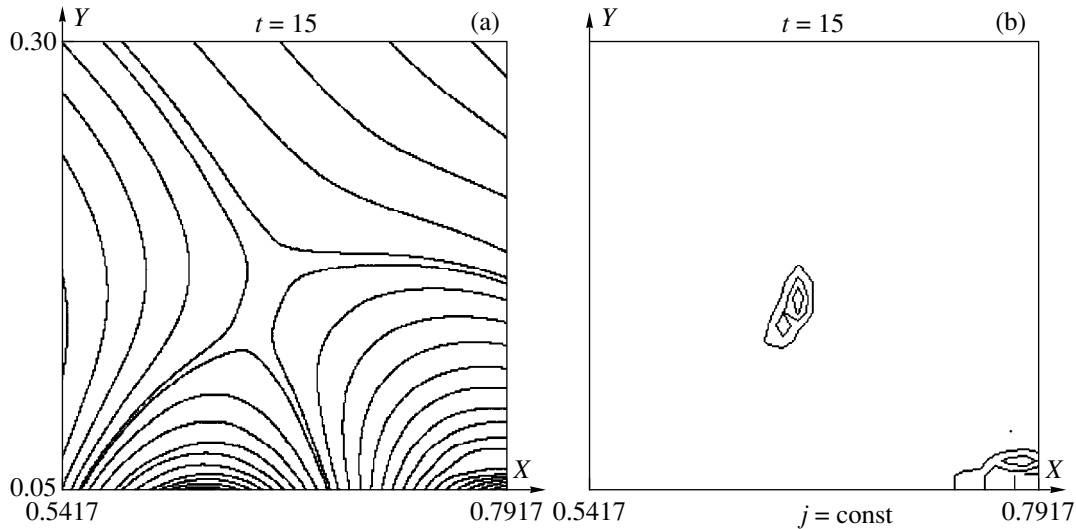
Fig. 3. (a) Lines of the magnetic field and (b) levels of equal current density during the formation of a current sheet by slowly emerging magnetic flux.

butions of the magnetic-field component parallel to the sheet and of the plasma temperature and density across the sheet (Fig. 2d) indicate the formation of a current sheet in which the magnetic and gas-kinetic pressures are in equilibrium. As the sheet decays, the energy stored in the magnetic field should be transformed into heat and form a solar flare and/or eject a plasma clump (transient) outside the solar corona [16, 17].

In this numerical experiment, we cannot precisely simulate the final stage of a flare event—the rapid decay of the sheet due to its instability. At time $t \sim 5$, only the initial stage of the MHD decay is observed. The plasma arriving together with the magnetic field cannot compensate its losses due to expulsion by the $\mathbf{j} \times \mathbf{B}/c$ force. The thickness of the sheet decreases, and then becomes comparable to the spatial step of the computations.

By this time, rapid reconnection (rapid plasma inflow to the sheet, together with the magnetic lines frozen in it) decreases the density at the sheet boundaries (Fig. 2d), where the density becomes considerably lower than ρ_0. Under these conditions, density fluctuations in the sheet can no longer be compensated by plasma inflow, and the system becomes unstable [5]. However, by this time, the sheet thickness has already become comparable to the spatial step, and the computation stops simulating the real process.

4. DISCUSSION

Observations indicate that, in flares following the emergence of new flux, the time interval between the onset of the flux emergence and the flare can be from a fraction of a minute to several hours. We have carried out several computations corresponding to real emergence timescales of from 20 s to 2 h. All these compu-

tations yielded a vertical current sheet, whose magnetic field stores magnetic energy. However, for long flux-emergence times, i.e., for long calculations, the errors of the numerical computation accumulated due to the finite spatial step and restricted size of the computation domain. These restrictions are determined by the computing power and the impossibility of using the method of characteristics to set the boundary conditions when there are large gradients at the boundaries of the computation domain. The most serious difficulties are associated with the boundary conditions for the temperature. The conditions $T = $ const, $dT/dn = $ const and the conservation of entropy describe the real situation poorly.

We have presented data above only for the rather fast emergence of new flux (~30 s), when any appreciable computation error has not yet had time to accumulate. For an emergence time of ~1 h, the current sheet also appears, but it is difficult to identify it against the background of numerical noise. Figure 3 shows the field and current density for a flux-emergence time of $t_r = 2$ min. Here, we can readily see the formation of a current sheet; however, the magnetic field in the lower right corner is already rather strongly distorted, and a current with opposite sign has arisen at the boundary. In a long calculation, the current sheet can be detected only through a very careful analysis of the data.

Let us consider in more detail the main effects accompanying the decay of the current sheet. First of all, the loss of sheet mass due to expulsion by tension forces leads to a decrease of the sheet thickness, an increase of the current density, and, consequently, an increase of the $\mathbf{j} \times \mathbf{B}/c$ force. As a result, the velocity of the plasma ejection can exceed the local Alfvén velocity [5], and the plasma expelled from the sheet will be

ejected into interplanetary space; i.e., a transient will be formed.

One-fluid magnetohydrodynamics does not take into account the Hall electric field in Ohm's law; i.e., strictly speaking, it is not applicable when $H = \mathbf{j} \times \mathbf{B}/V \times \mathbf{B}ne \ll 1$. Since the current density is negligible throughout the active region, except for in the current sheet, the Hall field can affect the plasma dynamics only inside the sheet. Writing the current density as $j = cB/2\pi a$, we obtain a dimensionless parameter for the current sheet, $H = Bc/2\pi \mathbf{a}neV$; here, $\mathbf{a}$ is the current sheet thickness, B the sheet magnetic field, and V the velocity of the plasma accelerated in the sheet. Adopting $B = 100$ G, $n = 10^{11}$ cm^{-3}, $V = 10^8$ cm/s, and $\mathbf{a} = 10^2$ cm, we obtain $H = 0.3$. Thus, the Hall effect may be important inside the sheet, and its influence is taken into account in the electrodynamic solar-flare model of [1, 18]. The model for a vertical sheet is presented in Fig. 4. The thin lines show the magnetic-field lines. The arrows inside the sheet show the Hall field, whose magnitude can be roughly estimated as $E = \dfrac{150B_n B}{\pi ane}$ V/cm. The normal component of the magnetic field $B_n \sim 2^* \times 10^{-6}$ G can be estimated from model [2] for a stationary sheet, in which the plasma flow is braked by an external hyperbolic magnetic field. Note that the ratio $B_n/B \sim 1/30$ we have obtained here fits well this model if we assume that the sheet thickness in the computation is determined by the numerical viscosity. For a sheet in the corona 10^9 cm in extent, we obtain a potential difference along the sheet of $\sim 10^5$ V. The Hall potential difference should lead to the generation of longitudinal currents (shown in Fig. 4 by bold lines). Pairs of oppositely directed longitudinal currents are completed by Pedersen currents in the chromosphere. Electrons accelerated in the longitudinal currents precipitate to the chromosphere and give rise to emission, observed as H_α ribbons, as well as chromospheric X-ray radiation. As the current sheet decays, the field lines to the right and left of the sheet rapidly reconnect. Since the field lines are frozen in the photosphere, the sites of intersection of the photosphere by the longitudinal currents move away from each other. This results in the well-known divergence of ribbons during a flare.

The pairs of longitudinal currents above the current sheet propagate upward together with an Alfvén wave. They are completed at the wave front by displacement currents. The electrons accelerated in these longitudinal currents can escape along field lines into interplanetary space.

High-energy particles can be accelerated along the neutral line of the field [19], since an electric field $V_{in}B/c$ is applied along it, where V_{in} is the velocity of the plasma inflow to the sheet. Crude estimates show that this mechanism can account for the generation of ultra-high-energy cosmic rays. Recently, Mori *et al.* [20] have simulated the acceleration of protons along a neu-
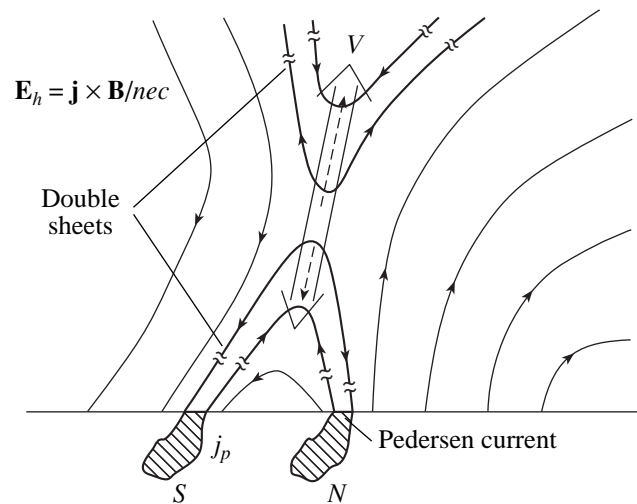
Fig. 4. Electrodynamic model of a flare with decay of a vertical current sheet.

tral line, considering acceleration up to energies of several MeV. In this energy interval, they obtained a power-law spectrum with index $\gamma = 2$–2.2, as is typical of cosmic rays.

ACKNOWLEDGMENTS

REFERENCES

1. A. I. Podgorny and I. M. Podgorny, Sol. Phys. **139**, 125 (1992).

2. A. I. Podgorny and I. M. Podgorny, in *Physics of Magnetospheric Flux Ropes*, Ed. by C. T. Russell, E. R. Priest, and L. C. Lee (American Geophysical Union, Washington, 1990), Series Geophysical Monograph, Vol. 58, p. 279.

3. A. I. Podgorny and I. M. Podgorny, Sol. Phys. **182**, 159 (1998).

4. A. I. Podgornyĭ and I. M. Podgornyĭ, Izv. Akad. Nauk, Ser. Fiz. **59** (8), 53 (1995).

5. A. I. Podgorny, Plasma Phys. Controlled Fusion **31**, 1271 (1989).

6. A. I. Podgorny and I. M. Podgorny, in *Solar Driver of Interplanetary and Terrestrial Disturbances*, Ed. by K. S. Balasubramaniam, S. L. Keil, and R. N. Smartt, Astron. Soc. Pac. Conf. Ser. **95**, 66 (1996).

7. E. R. Priest, *Solar Magnetohydrodynamics* (Reidel, Dordrecht, 1982; Mir, Moscow, 1985).

8. K. Shibata, in *Magnetodynamic Phenomena in the Solar Atmosphere*, Ed. by Y. Uchida, T. Kosugi, and H. Hudson (Kluwer, Dordrecht, 1996), p. 13.

9. S. Tsuneta, Astron. Soc. Pac. Conf. Ser. **46**, 239 (1993).

10. P. Demoulin, J. C. Henoux, and C. H. Mandrini, Sol. Phys. **139**, 105 (1992).

11. V. N. Ishkov, Izv. Akad. Nauk, Ser. Fiz. **63**, 2448 (1999).

12. A. I. Podgorny, Sol. Phys. **156**, 41 (1995).

13. D. P. Cox and W. H. Tucker, Astrophys. J. **157**, 1157 (1969).

14. A. I. Podgorny and I. M. Podgorny, Sol. Phys. **161**, 165 (1995).

15. A. I. Podgornyĭ and I. M. Podgornyĭ, Izv. Akad. Nauk, Ser. Fiz. **63**, 1516 (1999).

16. M. Dryer *et al.*, Sol. Phys. **181**, 159 (1998).

17. A. I. Podgornyĭ and I. M. Podgornyĭ, Astron. Zh. **76**, 696 (1999) [Astron. Rep. **43**, 608 (1999)].

18. A. I. Podgorny and I. M. Podgorny, Adv. Space Res. **19**, 1929 (1997).

19. A. I. Podgornyĭ and I. M. Podgornyĭ, Izv. Akad. Nauk, Ser. Fiz. **61**, 1067 (1997).

20. K. Mori, J. Sakai, and J. Zhao, Astrophys. J. **494**, 430 (1998).

Translated by G. Rudnitskiĭ

Emission Lines in the Spectrum of the Red-Dwarf Flare Star EV Lac: Modeling of the Quiescent Chromosphere

E. A. Baranovskiĭ, R. E. Gershberg, and D. N. Shakhovskoĭ

Crimean Astrophysical Observatory, National Academy of Sciences of Ukraine,
p/o Nauchnyĭ, Crimea, 334413 Ukraine
Received December 27, 1999

Abstract—We present spectral observations of the red-dwarf flare star EV Lac made at the Crimean Astrophysical Observatory in 1994 and 1995, and describe a method for semi-empirical modeling of the chromospheres of red dwarfs based on their emission spectra. We have modeled the quiescent state of the chromosphere of EV Lac for the cases of a homogeneous chromosphere and of active regions covering one-half and one-third the stellar surface. All models that are consistent with the observations indicate a region with a small vertical temperature gradient, a so-called temperature plateau. The calculated structure of the stellar chromosphere is compared with that of the solar chromosphere. © 2001 MAIK "Nauka/Interperiodica".

1. INTRODUCTION

The spectrum of UV Ceti red-dwarf flare stars continuously display intense emission lines of hydrogen, calcium and other elements originating in the chromospheric layers of their atmospheres. Quantitative analyses of these lines, started in the 1960s [1–3], provide fuller information about the physical conditions in the quiescent states of the atmospheres of these stars.

In international coordinated observing campaigns of the flare star EV Lac in 1994 and 1995, studies of the star's photometric and spectral parameters were carried out together with searches for decameter radio bursts. The spectral results obtained at the Crimean Astrophysical Observatory (CrAO) during these campaigns are described by Abranin *et al.* [4]. Here, we present a detailed analysis of the CrAO results for the profiles and intensities of emission lines in the quiescent state of the star.

2. CRAO SPECTRAL OBSERVATIONS OF EV Lac IN 1994 AND 1995

All spectral observations of EV Lac at CrAO were made with the 2.6-m Shain Telescope equipped with CCD spectrographs. In 1994, spectral monitoring of EV Lac was carried out on six nights, at 4190–5480 Å with resolution 4 Å. In the quiescent state of the star, for an exposure time of 10 min, the signal-to-noise ratio reached 140 at the center of the H_β line, 70 at the center of the H_γ line, and 90 and 30 in the continuum adjacent to these lines. In 1995, spectral monitoring of EV Lac was carried out near the H_α line with spectral resolution 0.37 Å during the first night and 0.74 Å during the other four nights. In the quiescent state of the star, with an exposure time of 30 min, the signal-to-noise ratio

reached 150 at the center of the H_α line and 90 in the adjacent continuum.

Table 1 presents the measured instrumental-profile widths for these observations. In addition to the usual full width at half maximum intensity (FWHM) we also evaluated the full width at quarter maximum intensity (FWQM). The third row of Table 1 presents the widths of Gaussians closest to the instrumental line profile. The Gaussian function $f^{cl}(\Delta\lambda) = e^{-(\Delta\lambda/\Delta\lambda_D)^2}$ that is closest to the line profile $f(\Delta\lambda)$ normalized to unity at its maximum corresponds to the Gaussian half-width $\Delta\lambda_D$ for which the relative rms deviation of the Gaussian from the considered instrumental profile $\epsilon(\Delta\lambda_D) = \sqrt{\sum((f_i - f_i^{cl})/f_i^{cl})^2/n}$ is minimum. When calculating ϵ, the summation was continued until f_i^{cl} became smaller than 0.01. The ϵ values in the fourth row of Table 1 indicate that the H_β instrumental profile can definitely be approximated by a Gaussian, while this approximation is poorer for the H_α and H_γ lines. Recall that, for any Gaussian, FWHM $= 2^{-1/2}$FWQM $= 2\sqrt{(\ln 2)}\,\Delta\lambda_D$.

Table 1. Measured instrumental profile widths (in Å)

Line parameter	Observations in 1994		Observations in 1995 in the red
	near H_β	near H_γ	
FWHM	5.64	4.10	0.65
FWQM	8.23	5.81	0.85
FWHM^{cl}	5.16	4.10	0.65
ϵ	0.10	1.2×10^{-2}	0.18

Table 2. Stellar parameters from Pettersen [20]

Star	T_{eff}, K	Sp	$B–V$
AD Leo	3450	M3.5e	1.55
EV Lac	3300	M4.5e	1.60
YZ CMi	3100	M4.5e	1.60

3. PRINCIPLES OF MODEL CALCULATION FOR THE QUIESCENT STELLAR CHROMOSPHERE

Stars in which convective energy transfer dominates in their sub-photospheric layers are known to possess atmospheres with non-monotonic temperature dependences. The temperature decreases upward in the convective zone; in the photosphere, however, a temperature minimum is reached, above which the temperature begins to increase and the chromosphere is formed. At present, there is no generally accepted theory of stellar chromospheres; however, various semi-empirical models for chromospheres exist. These are based almost solely on the observed parameters of continuum and line stellar spectra. Semi-empirical models determine the temperature distribution with height for which the calculated continuum and line profiles best fit the observations. The turbulent-velocity distribution with height is also calculated using the widths of observed lines formed at different heights. The variation of density with height is usually taken to obey the condition of hydrostatic equilibrium, but the magnitude of the density can vary, since the pressure at the upper boundary of the chromosphere or the mass of matter above this boundary are free parameters of the model.

Calculations of chromospheric spectra present considerable difficulties due to the appreciable deviations from LTE and the large optical depth of the chromosphere in spectral lines. Several specialized techniques have been developed to calculate chromospheric spectra; one technique that continues to be used widely is described by Avrett and Loeser [5] and Vernazza *et al.* [6]. For such calculations, it is necessary to specify the initial model parameters—the temperature and density—in an optically semi-infinite medium, i.e., in the chromosphere and photosphere. When a sufficiently rich set of observational data is available, a general model for the photosphere and chromosphere can be calculated; however, a previously prepared model for the photosphere consistent with the effective temperature is sometimes used. This photosphere model is either semi-empirical or calculated in accordance with the condition of radiative equilibrium.

Such calculations were first made for the solar chromosphere, based on extensive spectral observations from far UV to radio wavelengths [6–8]. With such a large set of spectral data, it was possible to find an interval of continuum spectrum or a spectral line that was formed at any height in the chromosphere or photosphere. As a result, the temperature distribution at all heights was determined with a rather high degree of certainty.

Later, this semi-empirical technique was also applied to stellar chromospheres, and numerous models for the chromospheres of cool stars have been calculated. Kelch [9] calculated a chromosphere and photosphere model based on the Ca II K-line profile and the fluxes in the h and k lines of Mg II. Kelch *et al.* [10], Giampapa *et al.* [11], and Doyle *et al.* [12] developed chromosphere models based on the Ca II K line. Houdebine and Doyle [13, 14] and Houdebine *et al.* [15] calculated a chromosphere model using the H_α and H_β lines. Mauas and Falchi [16] and Mauas *et al.* [17] used the absolute flux at 3500–9000 Å and the profiles of four Balmer lines, the Ca II K line, and the Na I D line to calculate models for three stellar chromospheres. In many of these calculations, the variation of the temperature and turbulent velocity was specified in the form of two or more sections with constant logarithmic gradients $dT/d(\log m)$ [18]. In fact, this way of specifying the temperature in a chromosphere is an artificial reduction of the number of free parameters—the temperatures at the ends of smaller height intervals. However, the main idea of the modeling technique persists: the criterion for an optimum model was agreement between the calculated and observed spectral characteristics. Since the mechanism for heating of the chromosphere remains not completely clear, neither energy balance nor radiative equilibrium are considered in semi-empirical model calculations for chromospheres.
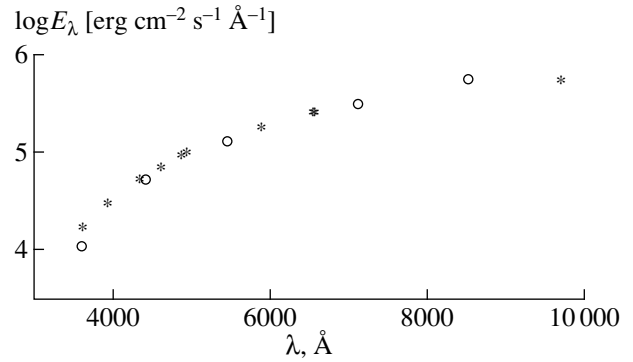
4. PHOTOSPHERE MODEL FOR EV Lac

The role of the photosphere is minor when the source function in the H_α, H_β, H_γ, and He I $\lambda4471$ Å line is calculated; the photosphere affects these lines only weakly via the adopted value of the effective temperature, which determines the radiation field during photoionization from excited levels. The calculated outgoing intensity in these lines is usually given in units of the local continuum, which, in the quiescent state of the star, originates in the photosphere. Thus, when modeling the chromosphere of EV Lac, we are interested in its photosphere primarily as a convenient local standard for the continuum radiation. Since we do not consider here lines with strong absorption wings formed in the photosphere, such as the Ca II K line, the adopted model for the photosphere must meet only one condition: the calculated continuum spectrum at the wavelengths of the studied lines, from 4340 to 6563 Å, must coincide with the observed continuum. Taking this into account, we used a model for the photosphere of AD Leo kindly presented by Dr. A. Falchi, that was improved over that published by Mauas and Falchi [19] and Mauas *et al.* [17]. The parameters of AD Leo are very close to those of EV Lac: AD Leo's effective temperature is only 150 K higher than that of EV Lac, and AD Leo is only one subclass earlier in spectral type and has a $B–V$ color index only 0.05^m lower (Table 2).

In order to obtain a continuum source that would coincide with the continuum of EV Lac from the photosphere model for AD Leo, we only varied the continuum absorption coefficient slightly, retaining the structure of the model itself. The same process of finding agreement between an observed and calculated continuum by varying the continuum absorption coefficient was also used by Mauas *et al.* [17]. According to Allard and Hauschildt [21], from 4600 to 7000 Å, the total absorption in the photospheres of cool stars exceeds absorption by H⁻ ions by more than an order of magnitude. Varying artificially the ratio for the continuum absorption coefficients to 9.1 near H_α and to 17.8 near 3600 Å, we obtain a radiation source with the spectral energy distribution in Fig. 1. The same figure presents the surface brightness of EV Lac, calculated from its *UBVRI* stellar magnitudes (Table 3), the known distance to the star, 5.13 pc, and its size, $R_* = 0.35R_\odot$. Figure 1 shows a fully satisfactory agreement between the observed brightness of EV Lac and the model continuum source in this wavelength interval. Figure 2 presents photosphere models for AD Leo from the study of Mauas and Falchi [16], for Gl 588 (dM4) and Gl 628 (dM5) from the study of Mauas *et al.* [17], and for the radiation source we constructed. Here, also, we can see a completely satisfactory agreement. This provides a basis for us to use our empirically derived model for the photosphere in our further calculations.

5. MODEL FOR THE HOMOGENEOUS-SURFACE CHROMOSPHERE OF EV Lac

Using the chromosphere model for AD Leo from [17] as an initial model and proceeding by trial-and-error, we varied the model depth dependence of the temperature, density, and turbulent velocity in such a way that the H_α, H_β, and H_γ emission lines in the quiescent spectrum of EV Lac were reproduced, while the HeI λ4471 Å line, which is not observed outside flares, was absent. For the observed emission-line profiles, we used profiles averaged over all quiescent spectra obtained during the 1994 and 1995 spectral monitoring. We will justify this choice below.

To calculate the profiles of the indicated lines, we used code developed at CrAO and based on the theory of line formation under non-LTE conditions. The code adopts a special method to solve the integral equation for the source function [5, 6–8]. It has repeatedly been used by one of the authors in the analysis of solar spectra [24–26]. As sources of continuum absorption, we

Fig. 1. Energy distribution of the photospheric radiation of EV Lac derived from modification of the AD Leo photosphere model (asterisks) and from *UBVRI* photometry of EV Lac (circles).
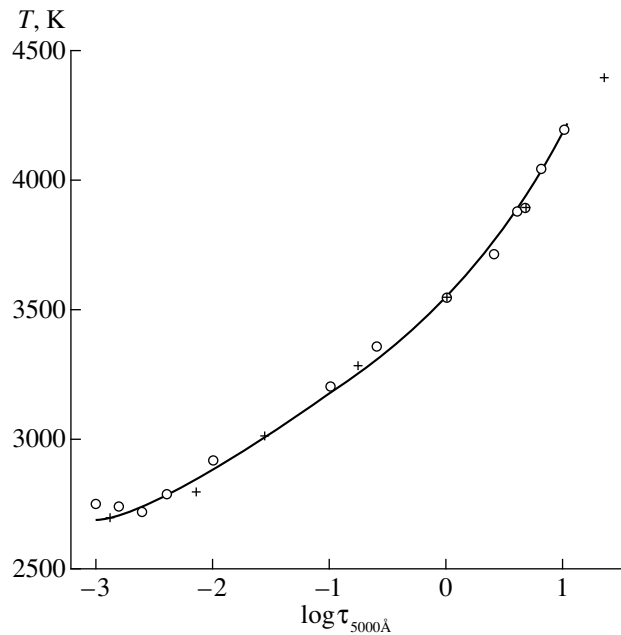

Fig. 2. Photosphere models of the red dwarfs AD Leo (circles), Gl 588 and Gl 628 (crosses), and EV Lac (solid line).

considered the following atoms and ions: H, H⁻, He I, He⁻, Mg I, Si I, C I, and Al I. We also took into account scattering on hydrogen and helium atoms, as well as on electrons. Absorption by molecules and a multitude of faint lines were not considered, since these sources of absorption are important only in photospheric layers with temperatures of 2500–4000 K. In our study, this

Table 3. Fluxes in photometric bands

	U	B	V	R	I
Flux density F_λ in 10^{-9} erg cm⁻² s⁻¹ Å⁻¹ for an A0 star 0^m, in accordance with Boyarchuk *et al.* [22] and Straĭzhis [23]	3.95	6.60	3.72	1.75	0.84
EV Lac stellar magnitudes	12.90	11.80	10.20	8.41	6.96
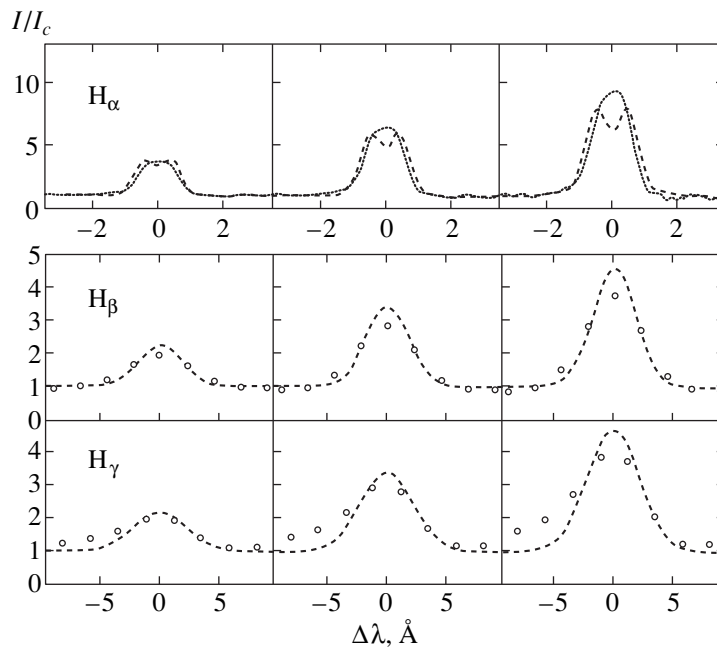
Fig. 3. Reproduction of the observed Balmer-line profiles. See explanation in the text.

type of absorption is negligible, since our main purpose is to determine the structure of the chromosphere in the regions of the formation of hydrogen and helium emission lines, where the temperature exceeds 5000 K. In our calculations, we adopted a model for the hydrogen atom with 10 levels and the continuum, and a model for the helium atom with 16 levels and the continuum. We took into consideration all line-broadening mechanisms: van der Waals, Doppler, damping, and Stark.

Following Cram and Mullan [18], in the first stages of our calculations, we specified the dependence of temperature on depth in the chromosphere in the form of two rectilinear sections with constant gradients $dT/d(\log m)$, assuming that the radial density m, i.e., the mass of a unit column of matter above the upper boundary of the chromosphere of EV Lac, was the same as that in the AD Leo model chromosphere. In the last stages of the calculations, however, we did not retain this scheme.

To compare the results with observations, we convolved the calculated profiles with the instrumental profiles in Table 1. We took the turbulent velocity to be 2 km/s over the total height of the chromosphere, since the width of the calculated H_α profile exceeds the observed value when the turbulent velocity exceeds this value.

The calculations demonstrated that we must consider chromosphere models in which the main region of formation of the Balmer lines ($T = 5000$–9000 K) extends to large depths where $\log m \sim -2.5$, thus encompassing high-density regions. Extension over a range of depths rather than a large density is important here, since mod-

els in which the density increases over the entire range of depths via the value of m but the regions of Balmer-line formation are located above $\log m = -3.5$ do not satisfactorily reproduce the observed line equivalent widths. The temperature dependence in regions where $T > 9000$ K was chosen such that the He I $\lambda 4471$ Å line appears neither in emission nor in absorption. To calculate the ionization correctly, the models were calculated to the height where the temperature reached 50000 K.

In the initial stage, we calculated chromosphere models based on the average H_β and H_γ profiles for the quiescent state of EV Lac in 1994 and independently using the average quiescent H_α profile in 1995. However, the models we ultimately obtained for these two different initial data sets were so similar that it was possible to find a single model describing all the initial data equally well. Note that, in 1994, W_{H_γ} was determined with larger uncertainty than W_{H_β}, since the signal-to-noise ratio in H_β was a factor of three higher. Our values of W_{H_γ} are probably somewhat overestimated, since, according to the 1964–1970 observations of Gershberg [3], $W_{H_\gamma} = 4.6$–6.6. Therefore, when constructing the chromosphere model, we ascribed a larger weight to the H_β line. The results of our calculations are presented in Fig. 3, Table 4, and Fig. 4.

The left columns of plots in Fig. 3 presents the average profiles of the H_β and H_γ lines in the quiescent state of the star in 1994 (circles) and of the H_α line in the quiescent state in 1995 (dots). The dashed curves mark the best reproduction of these observations using a homo-

geneous-surface chromosphere model for EV Lac. Table 4 presents the varied and calculated equivalent widths, which indicate good consistency with the absolute flux in the H_α and H_β emission lines and less satisfactory agreement for H_γ. The EV curves in Fig. 4 present the temperature and density distribution for this homogeneous-chromosphere model.

We will now compare our results with previous calculations for the parameters of the chromospheres of active emission M dwarfs whose effective temperatures are close to that of EV Lac. Based on the Ca II K-line profile, Giampapa *et al.* [11] calculated a model for the lower chromosphere of the dwarf flare star YZ CMi, whose parameters are very close to those of EV Lac (Table 2). As in our calculations, in this model, the turbulent velocity does not exceed 2 km/s. The results of the calculations of [11] are presented in Fig. 4 by the YZ curve. Since it encompasses the temperature range from the temperature minimum to $T = 6430$ K, this model cannot be used to calculate the hydrogen emission lines over the entire range of their formation.

The AD curves in Fig. 4 correspond to the AD Leo chromosphere models calculated by Mauas and Falchi [16]. These models differ appreciable from ours: they have a monotonic increase of the temperature with height, whereas, in our model, there is a quite extended region with a very small vertical temperature gradient, i.e., a kind of temperature plateau, in the middle chromosphere. The reason for this discrepancy is not clear. On the one hand, according to [16, Fig. 3], the ratio of equivalent widths in the spectrum of AD Leo is $W_{H_\alpha}/W_{H_\beta} = 1.6$, whereas our data show this ratio in the spectrum of EV Lac to be 0.81. Since the continuum spectral energy distributions for both stars are essentially the same, the flux ratios F_{H_α}/F_{H_β} also differ by approximately a factor of two. Such significant differences in the Balmer decrement provide evidence for appreciable differences in the radiating media.

On the other hand, the temperature plateau in our model is very similar to the analogous structure in the solar-chromosphere model, which is based on extremely rich observational material (see [8, Fig. 1]). Recall that, in their thermodynamical analysis of the solar chromosphere, Athay and Thomas [27] predicted the existence of a plateau in the dependence of temperature on height, as a result of the presence of temperature-stabilizing "coolers" in the medium, such as neutral hydrogen atoms and helium ions. Another temperature plateau is also seen in semi-empirical chromosphere models for the active K2 dwarf ε Eri [9, 28, 29], whose spectrum is comparatively close to that of the Sun. The presence of analogous structures in other stars supports our chromosphere model for EV Lac. According to the calculations of Vernazza *et al.* [8], the temperature plateau in the Sun for $T \sim 6500$ K extends from $\log m = -4.7$ to $\log m = -3.4$; the total density in this plateau is from 2×10^{11} to 6×10^{12} cm^{-3}, and the electron density is from

Table 4. Chromosphere models

| Line	Equivalent widths for emission lines, Å		Optical depths at the line centers
	measured	calculated	
Model with homogeneous chromosphere			
H_α	4.2	4.5	85
H_β	5.2	5.6	12
H_γ	9.6	6.4	4
Model with active regions covering one-half the stellar disk			
H_α	8.4	8.4	290
H_β	10.7	11.1	40
H_γ	19.2	13.3	14
Model with active regions covering one-third the stellar disk			
H_α	12.6	13.7	340
H_β	15.6	18.2	47
H_γ	28.8	23.9	16

4×10^{10} to 8×10^{10} cm^{-3}. A comparison of the EV curve in the upper plot of Fig. 4 and [8, Fig. 1] indicates that the temperature plateau begins much deeper in the stellar chromosphere: at a level with radial density m an order of magnitude higher than in the chromosphere of the Sun.

Another appreciable difference between our model for the quiescent chromosphere of EV Lac and the model of Mauas and Falchi [16] for the quiescent chromosphere of AD Leo is the relative flux in calcium and hydrogen emission. In our model, the calculated $F_K/F_{H_\gamma} \sim 4$–5, whereas this ratio is 0.25 in the model of Mauas and Falchi [16]. Measurements for 12 flare red dwarfs by Pettersen and Hawley [30], including AD Leo ($F_K/F_{H_\gamma} = 1.2$), indicate an average F_K/F_{H_γ} ratio of 1.5.
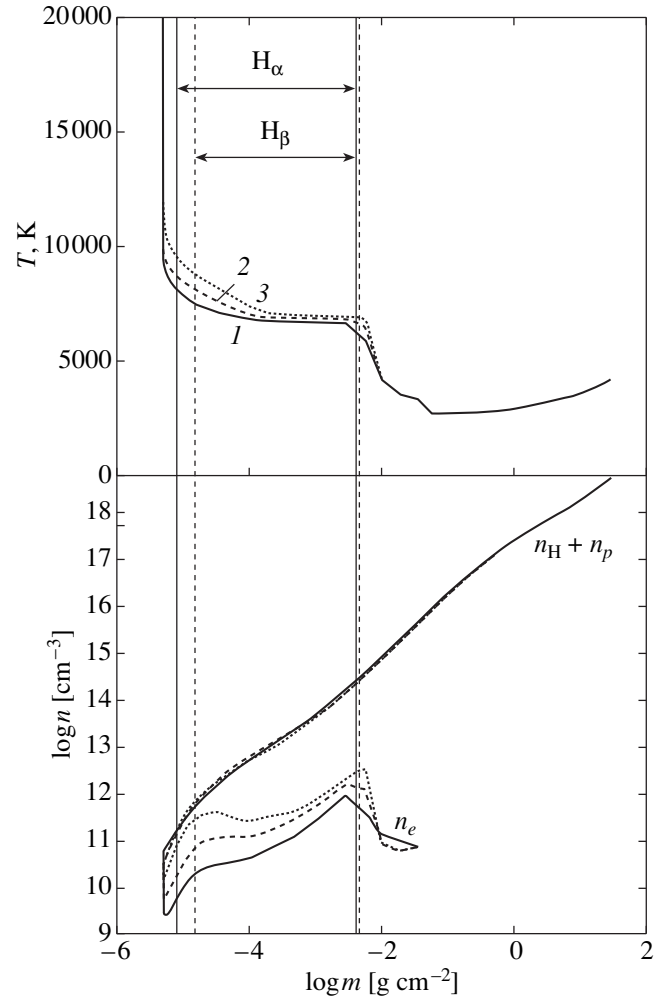
Thus, our model appears to yield an appreciably overestimated ratio F_K/F_{H_γ} compared to the average value, while the value of Mauas and Falchi [16] is underestimated. Since we have no observations of this ratio in EV Lac, we decided that there was no point in refining our model based on a discrepancy with the average for other stars.

In addition to the distribution of total hydrogen density, the lower plot in Fig. 4 presents the electron-density distribution, and the vertical lines drawn through both plots indicate the region of the chromosphere where 80% of the flux in the H_α and H_β lines is formed. We can see from this figure that the temperature plateau is the main region of formation of hydrogen emission lines, and the electron density in this region ranges from 10^{12} to 3×10^{10} cm^{-3}. The lower plot in Fig. 4 indicates that, while there is considerable similarity in the height distributions for the total densities in the EV Lac and AD Leo chromospheres, the electron-density distri-
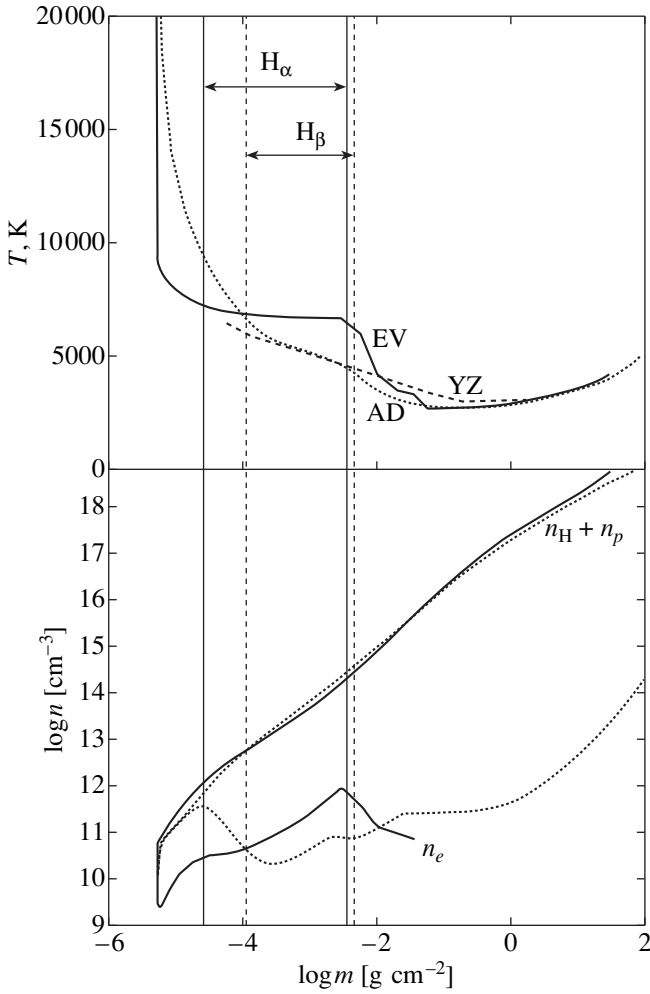
Fig. 4. Homogeneous chromosphere models for red dwarfs.

Fig. 5. Models for active regions in the chromosphere of EV Lac.

butions in these stars are appreciably different, due to the difference in the dependence of the temperature on height mentioned above. Note that estimates of n_e in the quiescent chromosphere of EV Lac, made by comparing the observed and calculated Balmer decrement for $T = 10^4$ K, yielded 3×10^{12} cm^{-3} [3] and 10^{13} cm^{-3} [31]. Based on the isothermal optically thick chromosphere model developed by Cram and Mullan [18], Pettersen *et al.* [32] estimated the electron density of the chromosphere of the star to be 10^{12}–10^{13} cm^{-3}, using the distance between the emission peaks of the H$_\alpha$ profile in the quiescent spectrum of EV Lac. Taking into account that, in our model, the lower regions of the temperature plateau contribute more to the total emission, we can conclude from the presented values that our height-structured model yields electron densities approximately an order of magnitude lower than previous height-homogeneous models.

6. MODEL FOR THE CHROMOSPHERE OF AN ACTIVE REGION

Despite the deep physical correlation between solar and stellar chromospheres, the observational data obtained for these structures are fundamentally different. A solar observer can fix the slit of his spectrograph on the image of some specific feature on the solar surface (the quiescent photosphere, spots, an active region) and use a model for specific structures of the underlying photosphere to analyze the chromospheric spectrum. When a star is observed, the chromospheric spectrum averaged over the stellar disk is detected against the background of the photospheric spectrum, which is also averaged over the disk. This difference must be taken into account in order to correctly apply procedures developed for the Sun to stellar spectra.

Appreciable night-to-night variations of the equivalent widths of emission lines in the spectrum of EV Lac provide direct evidence for substantial inhomogeneity

of the chromosphere of the star. For example, during six nights in 1994, W_{H_β} and W_{H_γ} varied with relative amplitudes up to 12 and 21%; and during five nights in 1995, W_{H_α} variations with amplitudes of 43% were detected. All these variations substantially exceed the errors. Such variations in the emission spectra of UV Ceti stars have been known for a long time. Their inverse correlation with the brightness of the star led to the idea that a major contribution to the observed emission of red dwarfs is made by active regions (the low-amplitude periodic oscillations of the brightness are due to the axial rotation of a star with a non-uniformly spotted photosphere). In calculations of chromosphere models, estimates of the inhomogeneity of the chromosphere of YZ CMi in various emission lines were obtained by Giampapa *et al.* [11]; Falchi *et al.* suspected substantial inhomogeneity of the chromosphere of AD Leo [33], as did Houdebine and Doyle for the chromosphere of AU Mic [14].

Our observations also indicate an inverse correlation between the intensity of the emission spectrum and the brightness of the star, especially in 1995. This enables us to roughly estimate the inhomogeneity of the chromosphere. According to the study of Alekseev and Gershberg [34], cool spots covered 1/7 of the surface of EV Lac in 1994, and 1/5 of the surface in 1995. On the Sun, the areas of active regions in the chromosphere exceed those of the corresponding photospheric cool spots by a factor of several tens. On EV Lac, there is no room for a factor of "several tens"; to satisfy the condition that active regions on the star have substantially larger areas than spots and simultaneously cover appreciably smaller than the total surface of the star, the active regions should cover 1/2–1/3 of the stellar surface.

Thus, the available data enable only a very approximate account for the chromospheric inhomogeneity of EV Lac: model calculations for the chromosphere of an active region should yield emission lines with equivalent widths that are factors of two to three larger than those directly measured. It is clearly necessary to take this correction factor into account; however, its probable error is so large that it is hardly advisable to consider the chromospheric properties on separate nights. We can only expect to obtain parameters of the chromosphere of EV Lac for some average active region.

Thus, to construct a model for the chromosphere of an active region, the calculations of the previous section must be repeated with the intensity of directly detected profiles of hydrogen emission lines increased by a factor of two to three, maintaining the condition that the He $\lambda 4471$ Å line not be observed. In this case, we neglect the contribution to the hydrogen emission from the stellar disk outside of active regions, assuming that, outside of active regions, Balmer lines are detected neither in emission nor in absorption.

The panels of the middle and right columns in Fig. 3 present the observed averaged profiles of emission lines

in the spectrum of EV Lac amplified in this way and the best fits for these profiles obtained in the chromospheric modeling for the stellar active regions. Given that both the profiles and equivalent widths were fitted, the resulting reproductions can be considered satisfactory. Table 4 presents the corresponding equivalent widths and optical depths at the line centers. Figure 5 reproduces the EV curve from Fig. 4 (denoted here as curve *1*), and presents models of the active regions corresponding to doubled and tripled profiles (curves *2*, *3*).

When the data from Table 4 and curves *1*, *2* and *3* in Fig. 5 are compared, it is apparent that the models calculated for active regions differ from that for a homogeneous chromosphere in their appreciably larger optical depth in the hydrogen lines, higher (by 500–1500 K) temperatures at the plateau, less extended isothermal regions, and earlier smooth rise to the high-temperature region. The H_α and H_β emission lines begin to form at essentially the same depths as in the homogeneous-chromosphere model, however, in the active-region models, they extend higher, to somewhat lower values of m. The electron densities are a factor of two to four higher in the active-region models than in the homogeneous-chromosphere model, and approach the above estimates obtained from the Balmer decrement and the splitting of the peak of the H_α emission profile.

Several years ago, Houdebine and Doyle [14] made detailed theoretical calculations for the chromospheres of dMe stars using the formalism of Gram and Mullan [18]. In particular, they presented an excellent fit for high-dispersion profiles of hydrogen lines in the spectrum of the dM2e star AU Mic, and obtained a good agreement between the calculated and observed Ly_α/H_α flux ratios, Balmer decrements, Balmer discontinuity, and Ly_α line width. However, they were not able to represent the H_α and H_β line profiles and their equivalent widths simultaneously. To avoid this discrepancy, they assumed that the observed emission originated only on 30% of the stellar surface, rather than over its entire area. (Note that, according to the photometric analysis of Alekseev and Gershberg [34], in 1971–1987, cool spots covered from 11 to 17% of the surface of AU Mic.) Estimates of n_e for the chromosphere of AU Mic obtained by Houdebine and Doyle [14], $n_e = (1–5) \times 10^{12}$ cm^{-3}, are close to estimates based on the Balmer decrement.

7. CONCLUSIONS

Our modeling of the quiescent chromosphere of the red dwarf EV Lac based on spectral observations made at the Crimean Astrophysical Observatory satisfactorily reproduce the average observed profiles and equivalent widths of the H_α, H_β and H_γ emission lines and the absence of the helium $\lambda 4471$ Å line in the spectrum of this star. We have calculated models for the quiescent state of the chromosphere both for a homogeneous chromosphere and for the case of active regions covering 1/2 and 1/3 of the surface.

In all cases, adequate description of the observations requires the presence of a temperature plateau in the chromosphere, extending from $\log m = -5.5$ to $\log m = -2.3$. Near the plateau, the temperature is 6500–7000 K, the total density varies from 10^{11} to 3×10^{14} cm^{-3}, and the electron density varies from 10^{11} cm^{-3} to 2×10^{12} cm^{-3}. Transforming the radial density to linear height, we find that the temperature plateau in the Sun is located in the range from 1200 to 1800 km, while the plateau in EV Lac is located from 200 to 700 km, much deeper and closer to the surface of the star.

ACKNOWLEDGMENTS

REFERENCES

1. O. C. Wilson, Publ. Astron. Soc. Pac. **73**, 15 (1961).

2. R. E. Gershberg, Astrofizika **6**, 191 (1970).

3. R. E. Gershberg, Astron. Zh. **51**, 552 (1974) [Sov. Astron. **18**, 326 (1974)].

4. E. P. Abranin, I. Yu. Alekseev, S. Avgoloupis, *et al.*, Astron. Astrophys. Trans. **17**, 221 (1998).

5. E. H. Avrett and R. Loeser, Smithson. Astrophys. Obs. Spec. Rep., No. 303 (1969).

6. J. E. Vernazza, E. H. Avrett, and R. Loeser, Astrophys. J. **184**, 605 (1973).

7. J. E. Vernazza, E. H. Avrett, and R. Loeser, Astrophys. J., Suppl. Ser. **30** (1), 1 (1976).

8. J. E. Vernazza, E. H. Avrett, and R. Loeser, Astrophys. J., Suppl. Ser. **45** (4), 635 (1981).

9. W. L. Kelch, Astrophys. J. **222**, 931 (1978).

10. W. L. Kelch, J. L. Linsky, and S. P. Worden, Astrophys. J. **229**, 700 (1979).

11. M. S. Giampapa, S. P. Worden, and J. L. Linsky, Astrophys. J. **258**, 740 (1982).

12. J. G. Doyle, E. R. Houdebine, M. Mathioudakis, and P. M. Panagi, Astron. Astrophys. **285**, 233 (1994).

13. E. R. Houdebine and J. G. Doyle, Astron. Astrophys. **289**, 169 (1994).

14. E. R. Houdebine and J. G. Doyle, Astron. Astrophys. **289**, 185 (1994).

15. E. R. Houdebine, J. G. Doyle, and M. Koscielecki, Astron. Astrophys. **294**, 773 (1995).

16. P. J. D. Mauas and A. Falchi, Astron. Astrophys. **281**, 129 (1994).

17. P. J. D. Mauas, A. Falchi, L. Pasquini, and R. Pallavicini, Astron. Astrophys. **326**, 249 (1997).

18. L. E. Cram and D. J. Mullan, Astrophys. J. **234**, 579 (1979).

19. P. J. D. Mauas and A. Falchi, Astron. Astrophys. **310**, 245 (1996).

20. B. R. Pettersen, Astron. Astrophys. **82**, 53 (1980).

21. F. Allard and P. H. Hauschildt, Astrophys. J. **445**, 433 (1995).

22. A. A. Boyarchuk, B. A. Burnasheva, and V. I. Burnashev, Izv. Krym. Astrofiz. Obs. **78**, 69 (1988).

23. V. Straĭzhis, *Multicolor Photometry of Stars* (Mokslas, Vilnius, 1987).

24. É. A. Baranovskiĭ, A. Kuchera, and Z. A. Shcherbakova, Izv. Krym. Astrofiz. Obs. **77**, 3 (1987).

25. É. A. Baranovskiĭ, E. V. Malanushenko, and A. V. Shumko, Astron. Zh. **94**, 454 (1997) [Astron. Rep. **41**, 399 (1997)].

26. V. G. Lozitskiĭ and É. A. Baranovskiĭ, Izv. Krym. Astrofiz. Obs. **88**, 67 (1993).

27. R. C. Athay and R. N. Thomas, Astrophys. J. **123**, 299 (1956).

28. T. Simon, W. L. Kelch, and J. L. Linsky, Astrophys. J. **237**, 72 (1980).

29. J. D. Thatcher, R. D. Robinson, and D. E. Rees, Mon. Not. R. Astron. Soc. **250**, 14 (1991).

30. B. R. Pettersen and S. L. Hawley, Astron. Astrophys. **217**, 187 (1989).

31. M. M. Katsova, Astron. Zh. **67**, 1219 (1990) [Sov. Astron. **34**, 614 (1990)].

32. B. R. Pettersen, D. S. Evans, and L. A. Coleman, Astrophys. J. **282**, 214 (1984).

33. A. Falchi, R. Pallavicini, P. J. D. Mauas, and L. Pasquini, in *Cool Stars, Stellar Systems, and the Sun*, Ed. by R. Pallavicini and A. Dupree, Astron. Soc. Pac. Conf. Ser. **109**, 603 (1996).

34. I. Yu. Alekseev and R. E. Gershberg, Astrofizika **39**, 67 (1996).

Translated by K. Maslennikov

Intensity Dependence of the Asymmetry of Fraunhofer Line Profiles

D. M. Kuli-Zade

Rasul-zade State University, ul. Khalilova 23, Baku, 370148 Azerbaijan
Received July 19, 1999

Abstract—The integral, residual, and relative asymmetries of the profiles of 120 weak and medium-strength Fraunhofer lines in the spectrum of the central solar disk are determined. The digitized spectral materials used were obtained using rapid-scanning, high-dispersion double monochromators. The integral profile asymmetries grow appreciably with line equivalent width, while the residual and relative profile asymmetries do not show such a strong dependence. © *2001 MAIK "Nauka/Interperiodica".*

1. INTRODUCTION

The use of new, rapid-scanning double monochromators and Fourier spectrometers with high dispersion and high resolution in spectroscopic observations of the Sun has made it possible to detect and investigate in detail the asymmetry of Fraunhofer line profiles. Initially, this asymmetry was characterized via simple comparison of the blue and red wings of profiles. Later, it was described by the profile bisector. However, the bisector method cannot be used to characterize the asymmetry quantitatively. Because of this, it was not possible to investigate variations in the asymmetry with atomic and photospheric parameters.

The asymmetry of line profiles can also be described using the asymmetry coefficient. Although this is not a physical quantity, it can be used to analyze the dependence of the asymmetry on macroscopic and microscopic quantities. Various studies [1–3] have found that the asymmetry coefficient decreases with an increase in line equivalent width. However, this result is subject to serious doubt, as we will discuss below.

Recently, we proposed a new method [4–6] enabling a quantitative characterization of the asymmetry of solar line profiles. We introduced the concepts of differential, integral, residual, and relative asymmetries. This enables the study of the dependence of the asymmetry of Fraunhofer line profiles on various atomic and photospheric quantities.

2. METHOD

Let $\Delta\lambda_{vi}$ and $\Delta\lambda_{ri}$ be the distances of the blue and red wings from the line center at an arbitrary depth $R(\Delta\lambda_i)$. Then, the quantity

$$\delta(\Delta\lambda_i) = \Delta\lambda_{vi} - \Delta\lambda_{ri} \qquad (1)$$

characterizes the asymmetry of the profile at the given depth. We call $\delta(\Delta\lambda_i)$ the differential profile asymmetry. We will consider the asymmetry to be blue when $\delta(\Delta\lambda_i) > 0$ or $\delta(\Delta\lambda_i) < 0$, and take the profile to be symmetrical when $\delta(\Delta\lambda_i) = 0$. Naturally, the dependence of $\delta(\Delta\lambda_i)$ on $R(\Delta\lambda_i)$ will show variations in the differential asymmetry in amplitude and sign within the profile.

We will call the area under the curve representing the dependence of $\delta(\Delta\lambda_i)$ on $R(\Delta\lambda_i)$ the integral asymmetry. It is clear that we can write the integral asymmetry analytically as follows:

$$\Lambda = \int_0^{R_0} |\delta(\Delta\lambda)| dR(\Delta\lambda) = \sum_i |\delta(\Delta\lambda_i)| \Delta R(\Delta\lambda_i), \quad (2)$$

where R is the profile depth and R_0 is its central value. The difference between the positive and negative parts of the integral asymmetry

$$\Delta\Lambda = \sum_i \left| +\delta(\Delta\lambda_i) \right| \Delta R(\Delta\lambda_i)$$
$$- \sum_i \left| -\delta(\Delta\lambda_i) \right| \Delta R(\Delta\lambda_i) \qquad (3)$$

we call the residual asymmetry. It shows the dominance of blue or red asymmetry. If $\Delta\Lambda > 0$, blue asymmetry dominates, if $\Delta\Lambda < 0$, red symmetry dominates, and if $\Delta\Lambda = 0$, both asymmetries have equal weight. The quantity

$$\Lambda_0 = \frac{\sum_i |\delta(\Delta\lambda_i)| \Delta R(\Delta\lambda_i)}{W} \qquad (4)$$

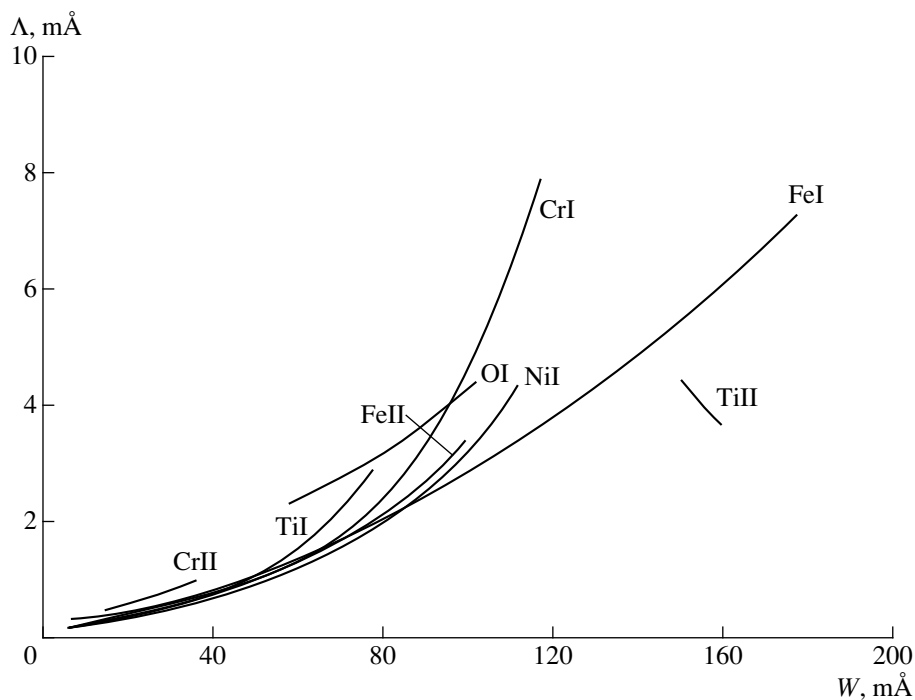will be called the relative asymmetry. Here, W is the line equivalent width.

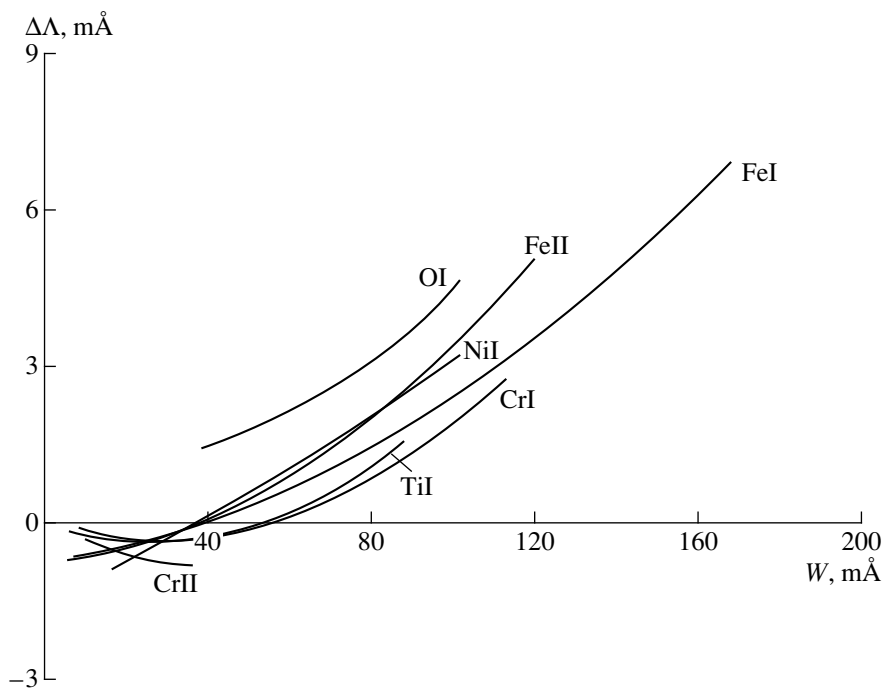**Fig. 1.** Integral asymmetry Λ as a function of line equivalent width W.

Fig. 2. Residual asymmetry $\Delta\Lambda$ as a function of line equivalent width W.

3. RESULTS

Using the newest digitized spectral materials for the center of the solar disk obtained with a rapid-scanning double monochromator [7], we constructed accurate pro-files of about 120 weak and medium-strength Fraun-hofer lines for various elements at wavelengths from 4400 to 7800 Å. We then determined the equivalent widths (W) and the integral (Λ), residual ($\Delta\Lambda$), and rel-ative (Λ_0) asymmetries of the line profiles. We used the
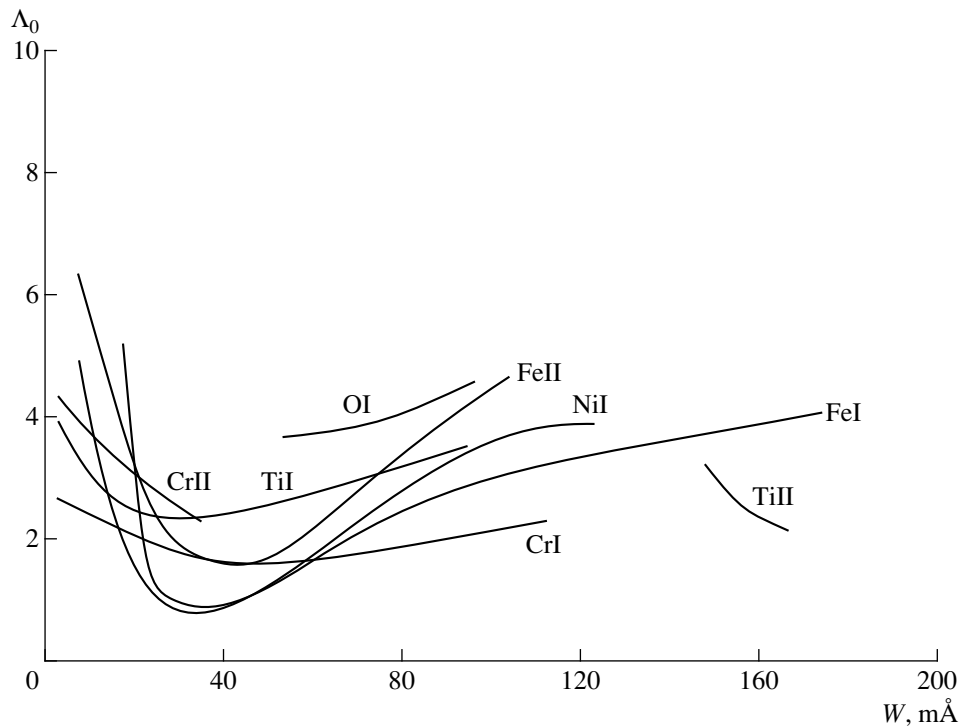
Fig. 3. Relative asymmetry Λ_0 as a function of line equivalent width W.

resulting quantitative data to study the dependence of Λ, $\Delta\Lambda$, and Λ_0 on the line equivalent widths.

Figure 1 shows the integral asymmetry Λ as a function of equivalent width W. For lines of all elements considered, there is an evident increase in Λ with W. Recall that various studies have shown the asymmetry coefficient, on the contrary, to decrease sharply with W.

Figure 2 presents the dependence of the residual asymmetry $\Delta\Lambda$ on W. For all lines except those of CrII, there is a significant increase in $\Delta\Lambda$ with W. For the CrII lines, $\Delta\Lambda$ decreases slightly as W increases. Note that the CrII ion is represented by a small number of lines (four in all).

The relative asymmetry Λ_0 as a function of W is given in Fig. 3. For weak lines ($W < 38$ mÅ), the relative profile asymmetry Λ_0 decreases with increase in W. When $W > 38$ mÅ, Λ_0 increases slightly with growth in W. The one exception is the TiII ion, which is represented by a small number of lines (four in all).

4. DISCUSSION

It is currently thought that the asymmetry of solar Fraunhofer line profiles is associated with dynamical processes in the photosphere. If this is the case, strong lines should be subject to the influence of these dynamic processes much more than weak lines, since the formation region for strong Fraunhofer lines encompasses the entire photosphere and lower chromosphere. Weak lines form only in a thin layer in the lower photosphere. Consequently, the asymmetry should increase with line strength, as indicated by our method.

We believe earlier results indicating a decrease in the asymmetry coefficient with increasing equivalent width to be erroneous. More precisely, the problem lies with the method, which cannot take into account variations of the sign of the asymmetry within a line profile. In reality, within a single line, the asymmetry can change its magnitude and sign multiple times. Therefore, red asymmetry at some profile depths may be compensated by blue asymmetry at others. As a result, an asymmetric strong line may seem nearly symmetrical. In our method, this factor is taken into account. As we can see from (2), when determining the total asymmetry, the magnitudes of the positive and negative parts Λ are added.

5. CONCLUSION

Our method can describe the profile asymmetry of weak and medium-strength Fraunhofer lines quantitatively and in more detail than earlier methods. The asymmetry is characterized by a quantity with a physical meaning. The integral profile asymmetry, as expected, grows with line intensity. The residual and relative asymmetries also grow, though more slowly than the integral asymmetry. Our results can be used to analyze candidate mechanisms leading to the asymmetry of Fraun-

hofer line profiles in the atmosphere of the Sun and other stars.

REFERENCES

1. R. I. Kostyk and T. V. Orlova, Astron. Astrophys. **9**, 117 (1970).

2. R. I. Kostik and T. V. Orlova, Sol. Phys. **36**, 279 (1974).

3. R. I. Kostik and T. V. Orlova, Sol. Phys. **53**, 353 (1977).

4. D. M. Kuli-Zade, M. Basal, and G. Kandemir, Kinematika Fiz. Nebesnykh Tel **11**, 51 (1995).

5. D. M. Kuli-Zade and M. Basal, Turk. J. Phys. **18** (9), 926 (1994).

6. D. M. Kuli-Zade, Vestn. Bakin. Univ., No. 1, 83 (1998).

7. L. Delbouile, L. Neven, and G. Roland, *Photometric Atlas of the Solar Spectrum from* λ 3000 to λ 10000 Å (Liege Univ. Press, Liege, 1973).

Translated by D. Gabuzda